UNIVERSITÀ
DEGLI STUDI
FIRENZE

DOTTORATO DI RICERCA IN
INTERNATIONAL DOCTORATE IN ATOMIC AND MOLECULAR PHOTONICS
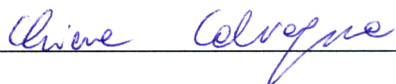
CICLO XXX

COORDINATORE Prof. Roberto Righini

Dynamical aspects of hydrophilic solvation from time resolved spectroscopy
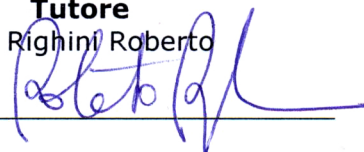
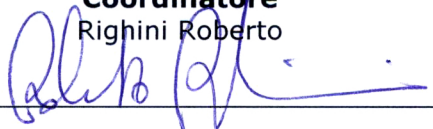Settore Scientifico Disciplinare CHIM/02

Dottorando
Dott. Calvagna Chiara

Tutore
Prof. Righini Roberto

Coordinatore
Righini Roberto

Anni 2014/2017

Contents

1. Introduction

Full understanding of structure and dynamics of condensed water is still an open challenge. Water shows peculiar behaviour that distinguishes it from the "normal" liquids. The most relevant anomalies are the decrease in density on passing from liquid to solid state and the increasing rotational diffusion under compression. The extended Hydrogen Bond (HB) network is the cause of water peculiarity [1].

Nowadays, the study of aqueous solutions is still fundamental. Water is the ubiquitous liquid on earth: it covers two-thirds of the surface of the earth and constitutes about 70% of the human body.

As a polar molecule (its dipole moment is 1.86 D in the gas phase), water has hydrophobic interaction with non-polar solvents and hydrophilic solvation with polar molecules. The hydrophobic effect consists in the strengthening of HBs around the solute molecules producing the so referred as iceberg structure; clathrate hydrates are one of the most important example of hydrophobic structures [2]. Differently, the addition of ions to water leads to severe alteration of the HB structure of the liquid and to formation of solvation shells. Conventional infrared absorption and Raman spectroscopic studies show this dramatic effect on the structure of the liquid [3, 4].

In the specific case of salt solution, there are two different kinds of HB: water-water and water-anion (salt); depending on the chemical behaviour of the anion, the water-anion HB can be stronger or weaker than that between two water molecules. Cox and Wolfenden classified the inorganic ions as structure makers or structure breakers according to the viscosity coefficient of their aqueous solutions at ordinary temperature. Structure-making ions enhance the hydrogen bond strength while structure-breaking ones weaken the hydrogen bonds in aqueous solution [5]. The presence of ions in water produces two different water subpopulations; the water molecules that form the first shell of the ions, and those whose first solvation shell consists entirely of water molecules (bulk water).

As an example of water solvation, we report the cases of two different salt: Sodium Perchlorate ($NaClO_4$) and Sodium Carbonate (Na_2CO_3). The HBs formed by water with ClO_4^- anion are long and substantially weaker than those in of the bulk water. Conversely, the Carbonate ions interact strongly with water, with HBs stronger than the water-water ones.

Obviously water does not form HBs with positive ions: in general, the presence of cations does not have relevant effects on the water structure, unless those due to the excluded volume.

It is clear that the HB dominates the solvation of solutes in aqueous solution. It is known that the variation of thermodynamic parameters, like pressure and temperature, influences the structure and the dynamics of water and aqueous solutions. Molecular Dynamics simulations and neutron scattering measurements provide structural information about the HB network, instead time-resolved spectroscopy gives a relevant contribution to know the water dynamics.

One can find in recent literature several studies of the properties of ionic solutions in dependence of temperature and concentration. Few examples instead can be found where pressure has been taken as a variable external parameter, in spite of the fact that the properties of solution at high pressure and the pressure dependence of the solubilisation process are of paramount relevance in geochemistry.

In this thesis, the main interest is focused on the water reorientation dynamics in solutions of NaClO$_4$ at different concentrations.
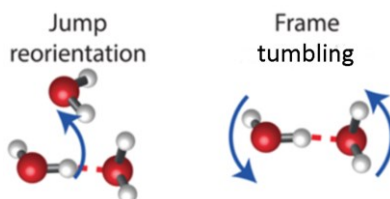
Fig.1.1 Large amplitude jumps and frame tumbling contribute to molecular reorientation

In a series of papers [6, 7, 8], Laage and co-workers developed and verified by MD computer simulations, a model describing the orientational motion of water in the bulk liquid and in ionic solutions. In short, two distinct mechanisms (**Fig. 1.1**) take place in reorienting the molecule:

1) *Large amplitude jumps*. A jump can be seen as chemical reaction that involves reactant, transition state and product. In **Fig.1.2**, we illustrate a scheme of the model.
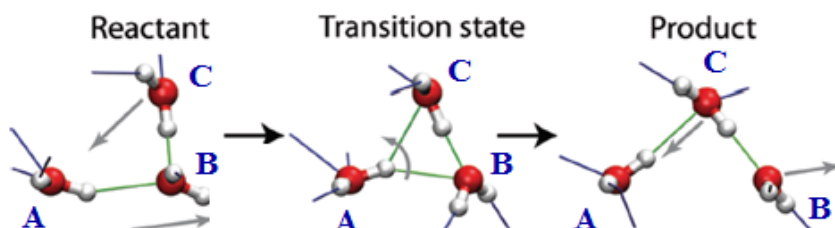
Fig. 1.2 Scheme of the jump mechanism [6].

The mechanism is a concerted one, involving the elongation of the initial HB joining A and B molecules and the simultaneous approach of the C molecule toward the A molecule that donates the HB. This first step is completed when the bifurcate transition state is formed. Finally, the A donor molecule rotates by a large angle and forms a new HB with the C molecule. The model can be seen like the mean results of many jumps of all molecules presents in solution; the mean jump angle calculated for neat water is about 68 °. The rate of the large amplitude jumps is $1/\tau_{jump}$.

2) *Frame tumbling*. In the time interval between successive jumps the molecular axis does not rest: its orientation is modulated by molecular librations on a femtosecond scale, and by the picosecond tumbling (diffusive) motion of the bi-molecular frame (**Fig. 1.1**).

It is worth of notice that, although the jump is a "local" event, it requires the approach of the new partner and the departure of the former partner, thus implying a rearrangement of the solvation shells. In this sense, it is strongly correlated with collective rearrangement of the HB network.

In pure water at room temperature, the jump mechanism has been shown [6] to dominate the orientational dynamics.
High pressure experiments [9, 10, 11] and computer simulations have shown that this model accounts for the pressure dependence of the orientational motion in neat water. At the same time, the model is able of explaining the orientational time constant measured in different ionic solutions, where seemingly contradictory behaviours were observed.

Time resolved infrared spectroscopy and time resolved Optical Kerr Effect (OKE), both with femtosecond resolution, are the experimental techniques adopted for the investigation of pressure and concentration dependence of water dynamics in $NaClO_4$ aqueous solutions. Classical computer simulations provide a substantial support in the interpretation of the experimental results.

In infrared experiments, the water orientational dynamics in samples consisting of HOD impurities in H_2O, is revealed by using the OD stretching band as a probe. The technique gives access to the second order Legendre polynomial of the time autocorrelation function of the O-D dipole moment μ: $C(t) = \langle P_2(\mu(0)\mu(t)) \rangle$. Thus, we are observing the behaviour of a "local" probe (with the intrinsic connections to the collective properties noticed above).

4

Differently from infrared spectroscopy, in time resolved OKE experiments the response function is proportional to the first derivative of the time correlation function of a collective property: the first order susceptibility of the sample [12]: $R_{ijkl}(t) \propto \frac{\partial}{\partial t}\langle \chi_{ij}(t) \cdot \chi_{kl}(0)\rangle$. In most liquids, the molecular orientational motion dominates; this is not the case for water. In fact, the molecular polarizability of water is almost isotropic and the optically induced polarization is dominated by intermolecular contributions. This holds not only for the short-time (typically 1 - 2 ps) OKE signal, but also for the long-time relaxation tail. In other words, the OKE and depolarized-light scattering techniques are mostly sensitive to the intermolecular dynamics of water. In the short delay time limit, this corresponds to the intra-cage vibrational dynamics; the long-time decay, in contrast, is prevalently associated with rearrangement of local structures, which represents the first step of the overall structural relaxation.

Thus, the two techniques look at the water dynamics from significantly different points of view; their parallel use can provide interesting additional information on the dynamical properties of water in the ionic solutions investigated here.

2. Time-Resolved Vibrational Spectroscopy

2.1 Outline

Time Resolved Vibrational Spectroscopy (TRVS) is one of the most frequently used transient technique. In fact, the time evolution of the vibrational spectra allows gathering information about the structure and dynamics, at the molecular scale, of condensed phase molecular systems [13].

TRVS is a specific realization of the general Four Wave Mixing (4WM) experimental scheme. In its simplest set-up, the experiment follows the pump-probe scheme. A first pulse (acting twice) promotes the molecules from the ground to an excited vibrational state, and a second pulse probes the excitation. The interactions of the pulses with the sample produces the third-order polarization that is source of the signal field (**Eq. 1.2**).

A sketch of the experimental setup is shown in **Fig. 2.1**.
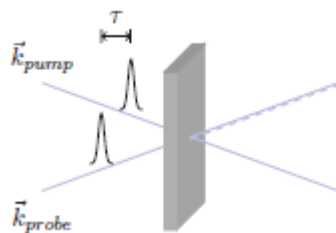
Fig. 2.1 Schematic representation of a pump-probe experiment.
The dotted line represents the signal beam, this is emitted in the same direction of the probe [14].

Feynman diagrams are generally used for describing the third-order terms of the non-linear polarization that contribute to the signal. For an isolated vibrational mode, three levels, corresponding to vibrational quantum numbers 0, 1 and 2, have to be included. The relevant diagrams are collected in **Fig. 2.2**.

Fig. 2.2 Feynman diagrams relevant for the Time-Resolved Vibrational Spectroscopy (TRVS).

In the figure, diagrams [1] and [2] describe ground state Bleaching (B), [3] and [4] correspond to Stimulated Emission (SE), [5] and [6] are relative to Excited State Absorption (ESA).

Because of the vibrational anharmonicity, the frequency (ω_{21}) of the ESA signal is lower than that of B and SE (ω_{10}). The ESA signal corresponds to increased absorption and gives rise to a positive band in the differential spectrum, while B and SE contribute with a negative band.
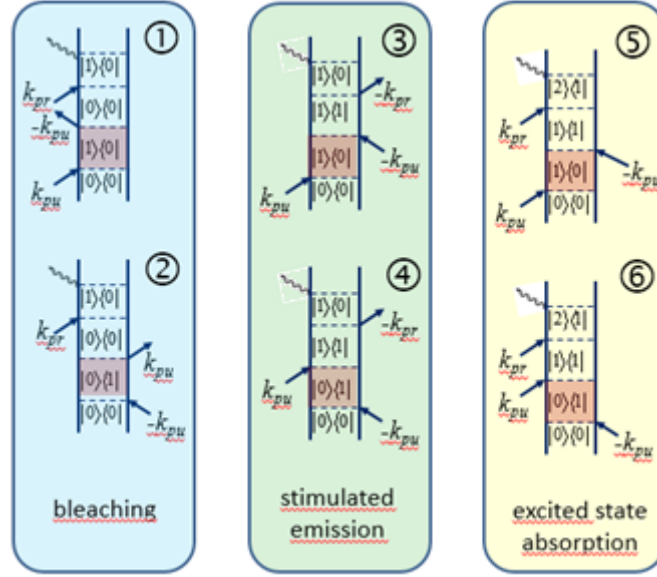
The expressions for the non-linear polarization corresponding to the six diagrams in **Fig. 2.2** are given below:

Polarizations obtained by the [1] and [2] diagrams, relative to B:

$$P_{1,2}^{(3)}(t) \propto \rho_{00}(0) \cdot |\mu_{10}|^4 \cdot E_{pu} \cdot E_{pu}^* \cdot E_{pr} \cdot e^{ik_{pr} \cdot z} \cdot e^{-\Gamma_{00} \cdot t} \cdot e^{-\Gamma_{10} \cdot (t-\tau)} \cdot e^{-\omega_{10} \cdot (t-\tau)} \qquad (2.1)$$

Polarizations for the [3] and [4] diagrams, relative to SE:

$$P_{3,4}^{(3)}(t) \propto \rho_{00}(0) \cdot |\mu_{10}|^4 \cdot E_{pu} \cdot E_{pu}^* \cdot E_{pr} \cdot e^{ik_{pr} \cdot z} \cdot e^{-\Gamma_{11} \cdot t} \cdot e^{-\Gamma_{10} \cdot (t-\tau)} \cdot e^{-\omega_{10} \cdot (t-\tau)} \qquad (2.2)$$

Polarizations given by the [5] and [6] diagrams, relative to ESA:

$$P_{5,6}^{(3)}(t) \propto \rho_{00}(0) \cdot |\mu_{10}|^2 \cdot |\mu_{21}|^2 \cdot E_{pu} \cdot E_{pu}^* \cdot E_{pr} \cdot e^{ik_{pr} \cdot z} \cdot e^{-\Gamma_{11} \cdot t} \cdot e^{-\Gamma_{21} \cdot (t-\tau)} \cdot e^{-\omega_{21} \cdot (t-\tau)} \qquad (2.3)$$

In Eq.(2.1 - 2.3), ρ_{00} is the ground state population at equilibrium, μ_{10} and μ_{21} are the transition moments, Γ is the reciprocal of the dephasing time. Note that the expressions (2.1)–

(2.3) have been written for a pump-probe experiment, in which the wave vector of the probe beam (k_{pr}) coincides with that of the signal.

As already noticed, a schematic representation of the differential absorption spectrum, consisting of two bands of opposite sign (see **Fig. 2.3**).
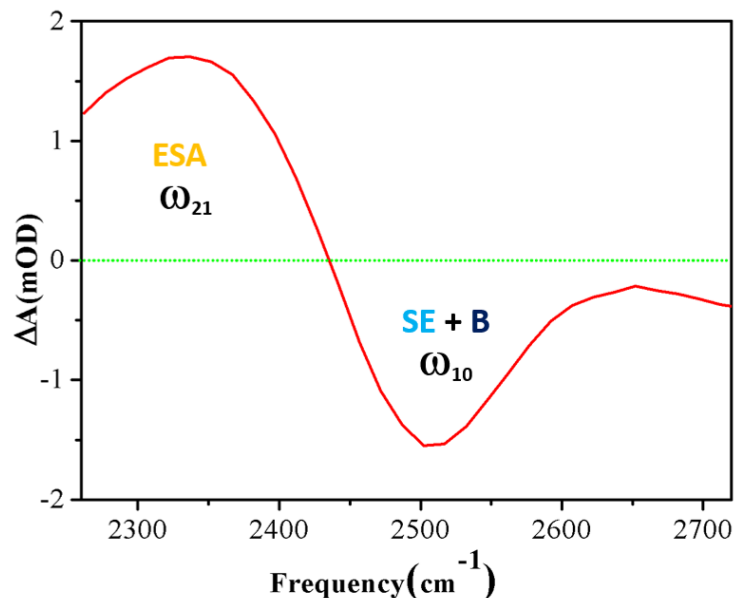
Fig. 2.3 Scheme of a Transient Infrared absorption spectrum.

2.2 Broadband pump probe spectroscopy

In our experiments we use two linearly polarized IR pulse. The pump pulse, centred at 2500 cm^{-1}, is resonant with the $0\rightarrow1$ transition of the OD oscillator; the probe pulse (same frequency as the pump), overlapped in the sample and separated by a controllable time delay (τ) from the pump, causes the collinear emission of the signal.

The signal field beats with probe field on the detector that measures the transient absorption spectrum. The transient signal is express in term of differential absorbance, obtained as the difference between the spectrum measured with the pump on and the spectrum with the pump off.

The IR pulses are 100 fs long and have spectral width of about 200 cm^{-1}. The very broad spectral width ensures coherent excitation and probing of practically any possible inhomogeneous frequency distribution of the vibrational transition under investigation.

Two important physical quantities can be directly obtained from a pump-probe experiment.

i) The excited state lifetime is obtained from the delay time dependence of the isotropic differential absorbance, defined as:

$$\Delta\alpha_{iso}(t) = \frac{\Delta\alpha_{\parallel}(t) + 2 \cdot \Delta\alpha_{\perp}(t)}{3} \qquad (2.5)$$

where $\Delta\alpha_{\parallel}$ is the absorbance measured with parallel polarizations of pump and probe pulses and $\Delta\alpha_{\perp}$ is the absorbance with orthogonal polarization of the two pulses. $\Delta\alpha_{iso}(t)$ is the absorbance free of orientational contribution; it coincides with magic-angle absorbance, obtained with t pump and probe polarization directions forming an angle of 54.7 degrees.

ii) The spectral anisotropy $R(t)$, defined as:

$$R(t) = \frac{\Delta\alpha_{\parallel}(t) - \Delta\alpha_{\perp}(t)}{3 \cdot \Delta\alpha_{iso}(t)} \qquad (2.6)$$

We performed experiments in the parallel and in the perpendicular configurations consecutively, in order to obtain the magic-angle and the spectral anisotropy. To this purpose, we used a half-wave plate ($\lambda/2$) placed on the pump beam.

Linearly polarized pump pulses excite the OD oscillator selectively, depending on their orientation [12]: consequently, the parallel absorbance is larger than the orthogonal. The anisotropy is maximum when pump and probe pulse coincide (time zero) and it decays for positive delays; the maximum theoretical value of $R(t)$ is 0.4.

The time constant obtained from the exponential fit of the anisotropy decay is a measure of how fast water molecules rotate and lose the initial orientation.

More precisely, $R(t)$ is proportional to the orientational correlation function $C_2(t)$ of the OD transition dipole, defined as:

$$C_2(t) = \langle P_2(\mu(0) \cdot \mu(t)) \rangle \qquad (2.7)$$

where P_2 is the second-order Legendre polynomial $P_2(x) = \frac{1}{2}(3x^2 - 1)$ and $\mu(t)$ is the OD transition dipole. In (2.7), $\langle\,\rangle$ denotes the ensemble average.

2.3 Two-Dimensional Infrared (2D-IR) spectroscopy

2D spectroscopy is a technique, in which the spectral intensity is obtained as a function of two independent spectral variables, wavenumbers in our case. The concept of 2D spectroscopy was first introduced several decades ago in the field of nuclear magnetic resonance (NMR) spectroscopy [15]. 2D spectra in NMR spectroscopy are typically obtained by applying a series of radio frequency pulses to a sample. Similar pulse-based 2D spectroscopy techniques are now practiced in the field of nonlinear optical spectroscopy, where a sequence of ultrafast optical pulses are used to produce 2D optical spectra.

A 2D-IR spectrum (an example is given in **Fig. 2.4**) is a symmetric spectrum respect to the main diagonal line corresponding to coordinates $\omega_1 = \omega_3$,
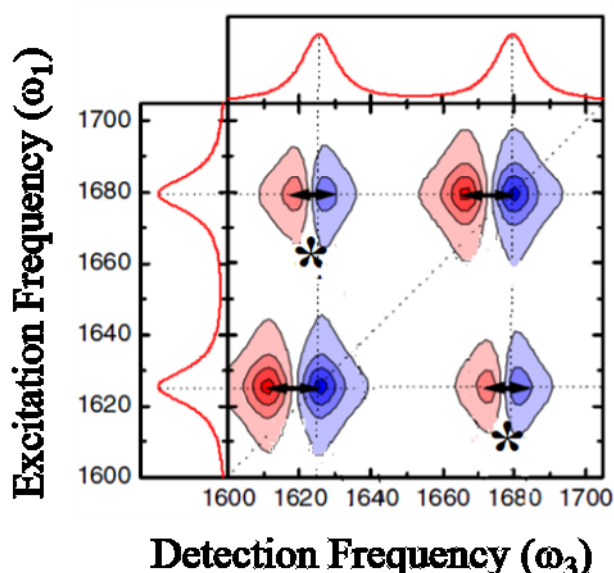
Fig. 2.4 Scheme of 2D-IR spectrum. Along the diagonal the negative peaks (blue) originate from B and SE. The positive ASE peak (red) is anharmonically red-shifted along the detection-frequency axis. The stars indicates the cross-peaks.

A 2D-map is recorded for a certain time delay (τ) between pump and probe pulses; the excitation frequency is along the y-axis and the detection frequency on the x-axis. Correlation peaks appear at both diagonal and off-diagonal positions. The intensity of peaks located at diagonal positions corresponds mathematically to the autocorrelation function of spectral signal intensity. Therefore, diagonal peaks are often referred to as auto-peaks [16]. Frequently, center lines of the diagonal peaks are used for a quantitative 2D lineshape analysis. Indeed, round peak shapes originating from homogeneous lineshapes give horizontal lines with a center line slope (CLS) of zero. In contrast, inhomogeneous lineshapes that are

elongated along the diagonal have a CLS of 1. The temporal fit of the trend of CLS as a function of population time allows quantifying the molecular spectral diffusion [14]. The CLS decay is directly proportional to the frequency fluctuation correlation function (FFCF):

$$\boldsymbol{FFCF = \langle \delta\omega_{01}(0) \cdot \delta\omega_{01}(\tau) \rangle}$$ (2.8)

Therefore, the time constant decay of the CLS function is a direct measure of the correlation time of the Brownian motion present in the solvent.

In addition, 2D spectra are able to reveal anharmonic couplings between different vibrations by the analysis of the cross peaks. The cross peaks are located at an off-diagonal position of the spectrum and they are characterized by different frequencies in the two coordinates ω_1 and ω_3. The presence of these peaks indicates the existence of coupling between different oscillators; it can also be due to the set-up of a chemical exchange.

2.3.1 2D-IR spectroscopy methods

2D-IR spectra can be collected in either the frequency [17, 18, 19] or time domains. Two experimental schemes can be adopted for time resolved 2D-IR experiments: the pump-probe scheme, where the excitation pulse band is narrowed and tuned by a Fabry-Perot interferometer, and the photon echo scheme, in which the full band-with of excitation and probe pulses is fully retained. In general, both method yield the same information. One of the purpose of my thesis has been the design and the development of the photon echo experiment.

Frequency-frequency domain experiment

The spectrally narrow, pump pulse is obtained by filtering the broad band pulse either with a tuneable Fabry-Perot etalon, or using a diffraction grating coupled to a slit. Both methods allow scanning the central frequency of the pump pulse across the frequency range of interest.

Fig. 2.5 gives a schematic picture of the set-up.
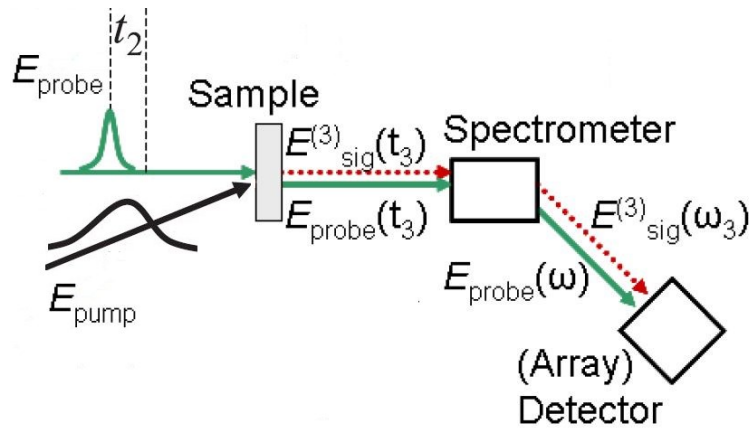
Fig. 2.5 Scheme of the experimental setup for narrow band pump – broad band probe 2D IR spectroscopy. The delay time τ corresponds to the population time [17].

The ω_3 axis in the 2D spectrum is obtained by passing the probe + signal beam through a grating monochromator and by detecting the spectrum by means of a 32 pixel MCT array detector. The discrete values ω_1 along the pump axis correspond to the peak frequency of the narrow-band pump beam. The 2D spectrum is obtained from the interpolation of the discrete spectra along the ω_1 axis.

The main drawback of this method is the limited time resolution due to the narrow linewidth of the pump pulse, corresponding to pump pulse duration in the range 500 – 800 fs, depending on the spectral region.

Time-frequency domain experiment

We realized the photon echo experimental set-up in the collinear scheme based on a Mach-Zehnder interferometer.

Fig. 2.6 Schematic view of the collinear 2D IR spectroscopy experimental setup.
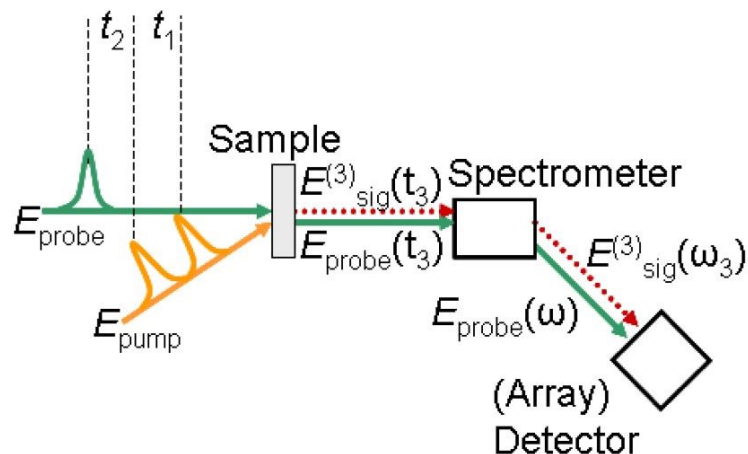The delay time t_1 and t_2 are respectively coherence and population time [17].

As schematically shown in **Fig. 2.6**, the pump beam is split in two parts: one beam travels along a fixed path, while the other is travels along a variable distance controlled by a motorized delay line stage. The length difference between the two paths provides the coherence time t_1.

In this two-beam pump geometry, the phase matching condition imposes that the emitted signal is collinear with the probe beam. The ω_3 axis is obtained by measuring the spectrum of the probe + signal beam, as described for the frequency-frequency experiment. The ω_1 frequency axis is determined by Fourier transforming the sequence of spectra recorded at different values of the coherence time t_1.

2.4 Experimental Setup

A scheme of the Transient-Infrared experimental set-up is shown in **Fig. 2.7**.
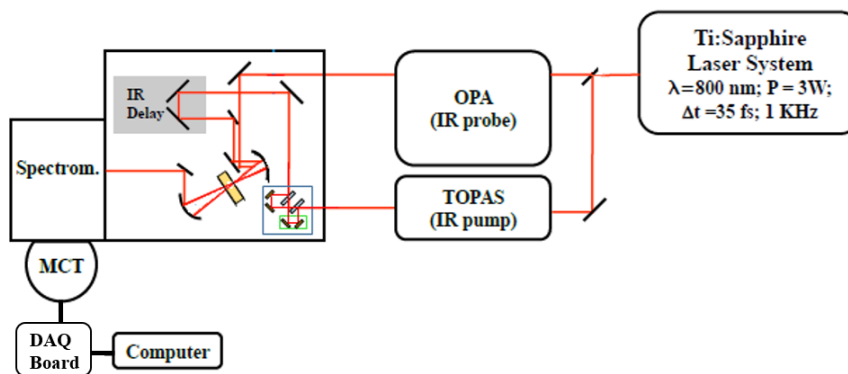
Fig. 2.7 Schematic view of the set-up for Transient IR measurements.

The laser system consists of a Ti:Sapphire oscillator (Micra, Coherent) and of a regenerative amplifier (Legend Elite, Coherent). This laser source produces pulses 35 fs long, with central wavelength of 800 nm at 1 KHz repetition rate. Optical parametric amplifiers (OPAs) are used to convert the fixed wavelength laser output into the Mid-Infrared (MIR) spectral region [20].

13

2.4.1 Laser system

The active medium of the oscillator (Micra, Coherent) is a Titanium:Sapphire rod, pumped by a 532 nm beam generated by the second harmonic of a Nd-YVO₄ laser. The two laser sources are integrated in a unique housing, which guarantees good thermal and mechanical stability.

The Micra oscillator operates in self-mode locking regime and generates an ultra-short pulse train at the repetition rate of 76 MHz. The oscillator output beam has wavelength of 800 nm, bandwidth of 90 nm and average power of (300-400) mW.

In the regenerative amplifier (Legend Elite, Coherent) the Ti:Sapphire active medium, placed inside the optical cavity, is pumped by a pulsed Nd-YLF operating at 1 KHz repetition rate. Two Pockels cells allow one pulse every 76.000 from the oscillator to enter the amplifier cavity and to extract the amplified pulse after a number of round trips. The amplification is done with the Chirped Pulse Amplification (CPA) method, which implies stretching of the seed pulse, followed by re-compression of the amplified pulse; stretching and compression operations are performed by means of two independently adjustable diffraction gratings. The output beam consists of a 1 KHz train of horizontally polarized pulses, with central wavelength of 800 nm, energy of 3 mJ, duration of 35 fs and spectral width of ~35 nm. Only a fraction of ~1.1 mJ is used for the infrared experiment

2.4.2 Optical Parametric Amplifier (OPA)

The 1.1 mJ fraction of the Ti:Sapphire amplifier output beam is split by a broad-band beam splitter (BS). The two beams pump two optical parametric amplifiers (OPAs), which convert the 800 nm beam into a couple of tuneable near-Infrared pulses (idler and signal).

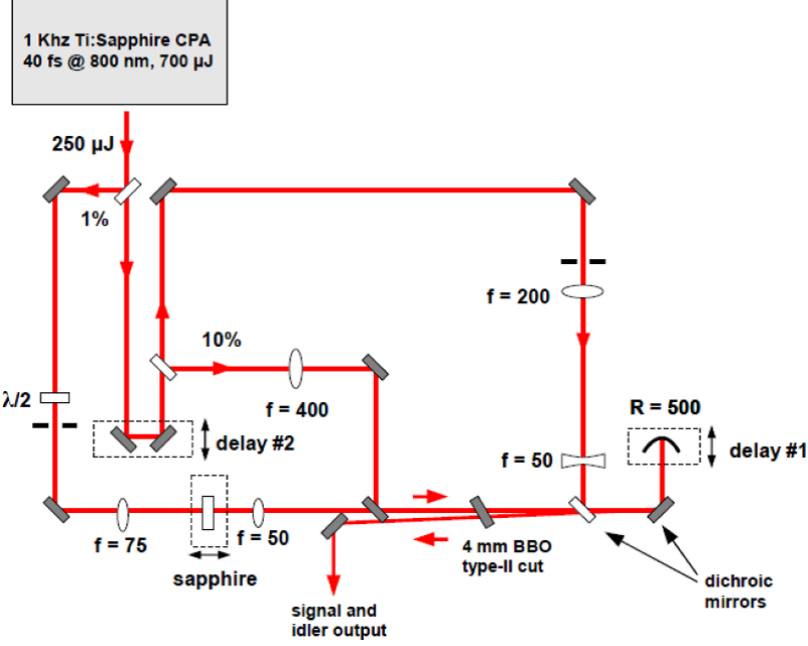The layout of the home-built two-stage OPA [21] is given in **Fig. 2.8**.

Fig. 2.8 Scheme of the two-stage optical parametric amplifier (OPA).

The OPA operates in three stages: i) generation of the seed for the super-continuum generation, ii) pre-amplification and iii) amplification to obtain the final signal and idler. The seed pulse is generated by focusing a small portion (1%) of the amplified 800-nm pulses into a sapphire plate that generates a white-light continuum, with frequencies that go from near-IR to visible. A long-wave pass filter eliminates the shortest wavelengths. Next, the seed pulses and 10% of the temporally delayed pump pulses are spatially and temporally (delay #2) overlapped and focused into the type II BBO amplifier crystal. The type II process used in the experiment follows the phase-matching conditions:

$$\omega_{pu} \cdot n_{eo} = \omega_{si} \cdot n_o + \omega_{id} \cdot n_{eo} \tag{2.9}$$

where ω_{si} and ω_{id} indicate the frequencies of signal and idler beams and n_i is the refraction index. In this geometry, signal and idler have orthogonal polarizations.

At the optimal phase-matching angle ($\theta = 27°$), the BBO crystal generates about 700 nJ of signal and idler output during this first stage of amplification. Better stability is obtained by removing, prior to the second amplification step, the idler and the residual 800 nm radiation by means of tailored dichroic mirrors. A concave mirror that also serves as a temporal delay for the second pass (delay #1) collimates the remaining signal beam.

The signal goes back into the same BBO crystal at a slightly different height (using the same crystal for both amplification stages simplifies tuning). The intense pump beam (200 µJ

per pulse) used in the second amplification step passes through a telescope, which adapts the beam size to the diameter of the collimated signal beam. Pump and signal pulses are overlapped temporally and spatially and propagate unfocused through the BBO crystal, generating energetic signal and idler pulses. The OPA delivers intense near-infrared with energy (sum of signal and idler) of approximately 150 μJ across the whole tuning range. The signal and idler pulses are continuously tuneable in the wavelength range 1-3 μm.

The mid-IR pulses (to be used, in our case, as probe pulses at $\lambda \approx 4$ - 6 μm) are generated by difference frequency generation (DFG) of signal and idler in a non-linear type I $AgGaS_2$ crystal. The MIR pulse energy is about 1-2 μJ, the pulse duration is 100 fs and the spectral bandwidth is about 200 cm^{-1}.

2.4.3 Sample chamber

Transient IR Absorption

To avoid spectral and temporal distortion of mid-IR laser pulses due to the absorption by water vapour and carbon dioxide (CO_2), the sample chamber is purged with nitrogen gas. In fact, in addition to the strong attenuation of the beam intensity, significant pulse distortions of the pulses happen at frequencies where water and carbon dioxide of air have resonant transitions (namely, 3700 and 1600 cm^{-1}, stretching and bending modes of H_2O; 2300 cm^{-1}, stretching mode of CO_2).

First, the probe beam passes through a filter that remove residual signal and idler. Then, it gets through a telescope that enlarge it of 1.5 times. Later, it arrives on a wedged plate, which splits off the transmitted beam used as the probe and a weak reflection beam used as reference.

The pump pulse, collimated by a telescope, goes through a MgF_2 half wave-plate ($\lambda/2$) that allows changing the pump polarization.

The pump beam, after being chopped at 500 Hz (half the repetition rate of the laser) travels a computer controlled delay line and is focused by a 30° off-axis parabolic mirror into the sample, together with the probe beam. Pump and probe are spatially overlapped inside the sample, whereas the reference beam follows a different path.

The pump beam is blocked after passing the sample. Probe and reference are spectrally dispersed in a 100 groove/mm grating spectrometer (TRIAX 180, HORIBA Jobin Yvon) and recorded separately on a 32 channels double array HgCdTe (MCT) detector (InfraRed Associated Inc.) cooled by liquid nitrogen (77 K).

The transient spectrum is obtained as the differential absorbance ΔA:

$$\Delta A = A_{on} - A_{off} = -log_{10}\left[\left(\frac{I_{pr}}{I_{ref}}\right)_{pump\ on} \cdot \left(\frac{I_{ref}}{I_{pr}}\right)_{pump\ off}\right] \cdot 1000 \tag{3.0}$$

A NI-DAQ acquisition board collects all the data and transmits these to the PC in real time.

2D-IR measurements

In **Section 2.3.1** I already pointed out that 2D experiments can preserve the full time resolution compatible with the pulse duration (~ 100 fs) only adopting a three-pulse photon echo scheme, in which pump and probe pulses maintain their full bandwidth, thus granting the maximum time resolution (better than 100 fs). The set-up I designed and realized in my PhD Thesis work is the two-beam scheme, with the two pump pulses, generated in a Mach-Zehnder interferometer, propagating collinearly.

The interferometer was designed as compact as possible, taking care that the pulses in the two interferometer arms experience the same material dispersion. In **Fig. 2.9** are illustrated the designs used by the LENS mechanical workshop for the realization of the interferometer support in aluminium. **Fig. 2.9-10** gives a schematic view of the optical set-up.
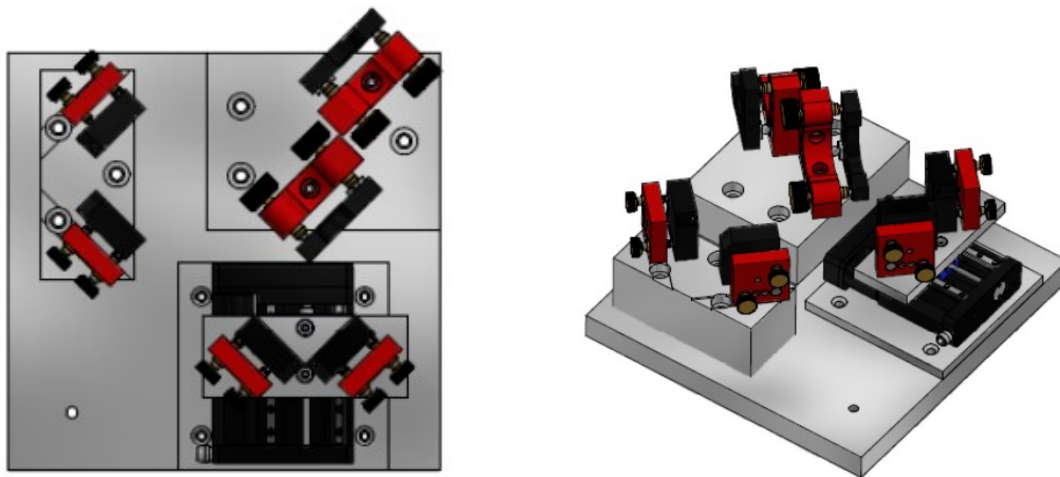

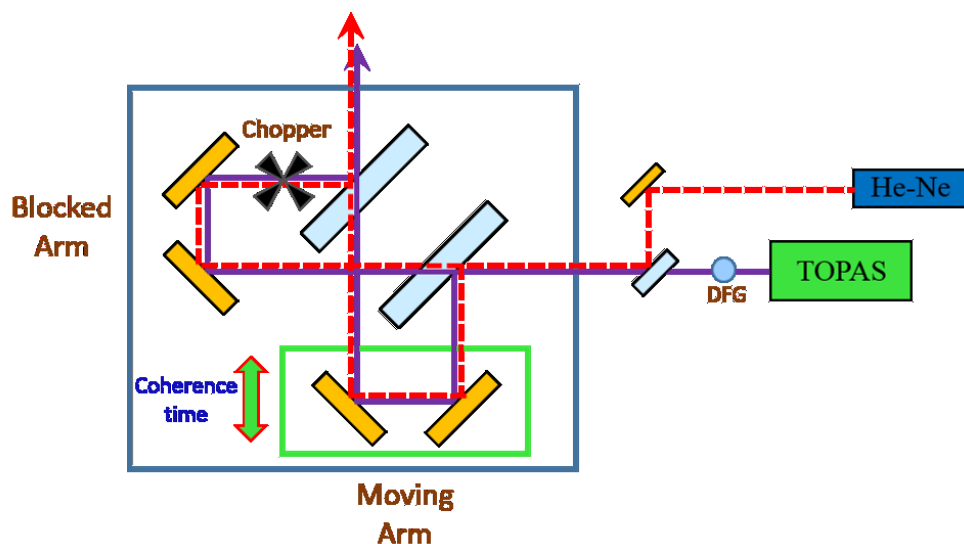**Fig. 2.9** Top view and 3D model of the interferometer.

Fig. 2.10 Schematic view of the Mach-Zehnder interferometer.

The adopted scheme is based on the Mach-Zehnder interferometer. Here, the excitation pulse (full bandwidth) is split in two beams of equal intensities by the beam splitter BS1. The first beam travels a fixed pathway (*Blocked Arm*); the second one proceeds on a variable path (*Moving Arm*), adjustable by means of a motorized sledge. The interferometric scan is performed by moving the sledge with constant velocity (0.001 mm/s). A chopper placed in the blocked arm eliminates long term drifts effects, allowing the acquisition of probe intensity with and without pump pulse in two subsequent shots. Finally, the two beams overlap on the second beam splitter BS2.

The device is designed as a single unit to be inserted in the pre-existing pump-probe setup. A He-Ne (633 nm) beam, made perfectly collinear with the mid-IR beam, makes the visual fine alignment of the interferometer possible. In addition, the He-Ne interference fringes provide a precise tool for measuring the pathlength difference in the two arms, which sets the t_1 coherence time.

The two collinear pump pulses are sent to a second motorized translation stage (that sets the population time delay t_2), and are focused onto the sample by an off-axis parabolic mirror, together with the probe beam. After passing the sample, probe and reference are spectrally analysed by a grating monochromator equipped with a 32 MCT elements double array detector. See **Fig. 2.11** for a sketch of the experimental setup.
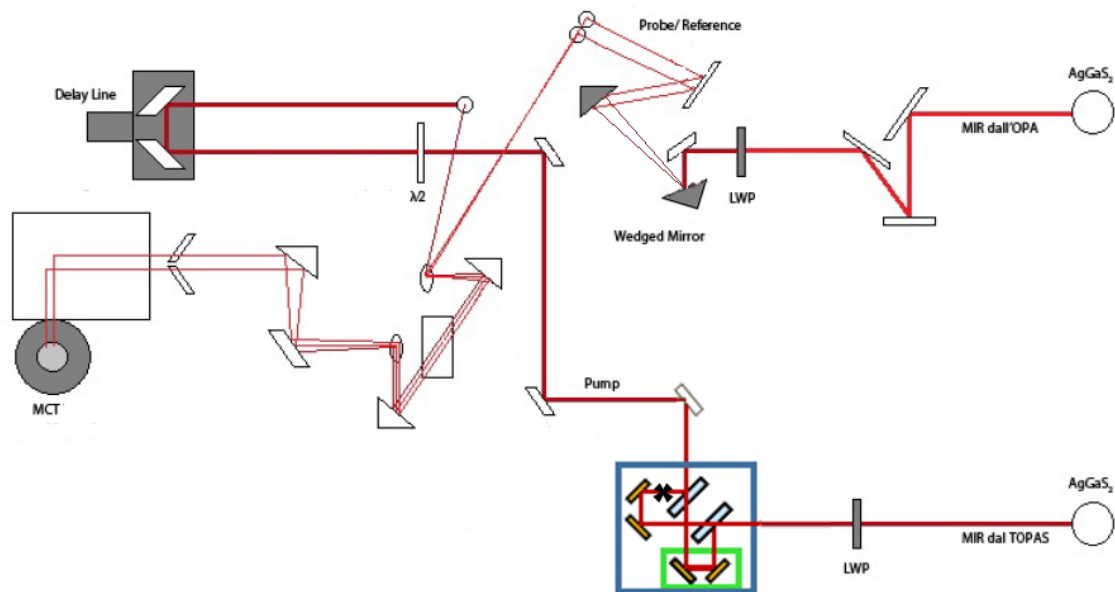
Fig. 2.11 Scheme of 2D-IR experiment.

Two-dimensional spectra are obtained as the Fourier transform of the one-dimensional spectra obtained at different values of t_1 coherence time. The time evolution of the 2D spectra is measured by varying the t_2 population time delay.

2.4.4 Data acquisition program

I wrote the acquisition programme in LabVIEW language. LabVIEW (Laboratory Virtual Instrumentation Engineering Workbench) is a platform and development environment for visual programming language from National Instruments. The program execution depends on the structure of a graphical block diagram, where the programmer connects different function-nodes by drawing wires.

The program performs the following operations:

1. Motion control of motorized sledge and reading of the sledge position (encoder);
2. Selection of the pump polarization ($\lambda/2$);
3. Check the state ("on" or "off") of the chopper;
4. Acquisition of the trigger signal;
5. Communication with the TRIAX spectrometer;

6. Reading the multichannel MCT detector and data acquisition

7. Data processing.

The acquisition software performs the complete scans of an experiment in an automatic way.
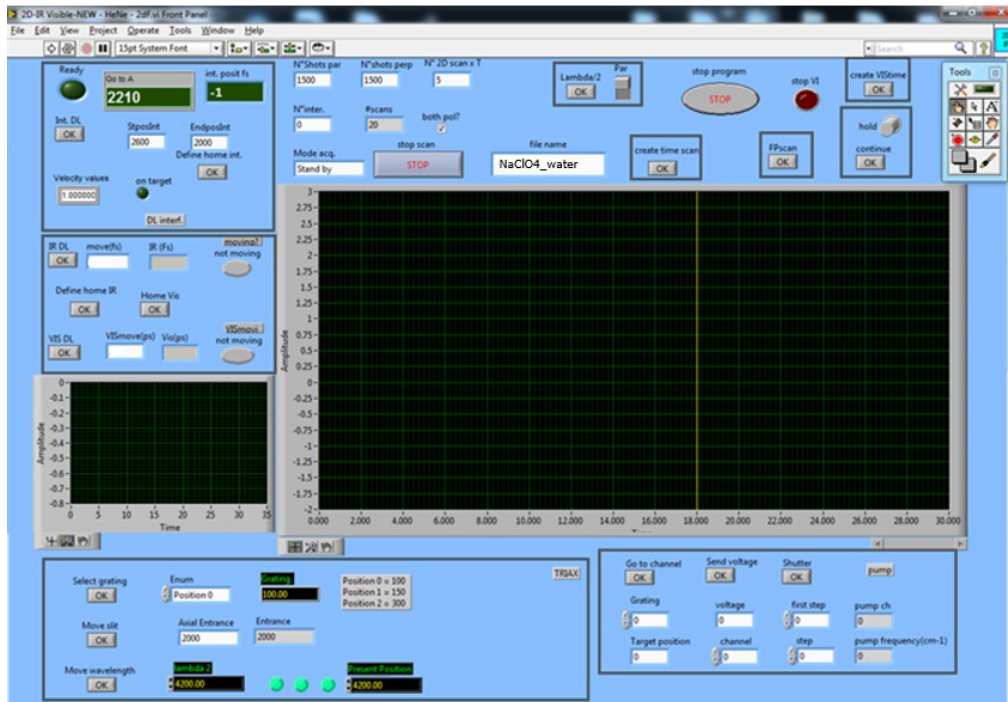
Fig. 2.12 Screenshot of the LabVIEW interface of the acquisition program.

We use a step-by-step approach to realize the broad band pump-probe experiment. Keeping the moving arm of the interferometer blocked, we set the t_2 pump delay line to a certain position and acquire the signal there. Then, we change the stage position, and acquire the spectrum in the new position. We repeat these two steps for the complete set of time delays.

In the 2D experiment, we use real-time acquisition of the signal during the rapid scan of t_1 in the interferometric optical delay line. With the t_2 delay line set at a certain position, we scan the t_1 delay line with a velocity of 0.001 mm/s; the acquisition card (DAQ) reads continuously the output signals from the MCT array. Then, we change the t_2 stage position and repeat the coherence time scan to acquire the spectra for a new 2D map at a different t_2 population time.

2.4.5 Sample cells

For ambient pressure experiments, we use a cell consisting of two Fluorite (CaF_2) windows separated by a 100 μm spacer. The two windows are assembled on a metallic structure, which isolates the sample and blocks the liquid evaporation.

For the high-pressure experiments (up to 1.3 GPa), we employ a Sapphire Anvil Cell (SAC). Sapphire is less hard of the diamond but, unlike the latter, is transparent in the mid-IR region of interest. The anvils have conical shape. The anvil face that is in contact with the sample is 300 μm in diameter; therefore, this very small area allows obtaining high pressure with the application of little force. The details of the SAC are described below.

High pressure cell

The preparation of the sample in a high pressure cell is not trivial; indeed, it must to be transparent to the light in the region of interest and resistant to different compression/decompression cycles. The first step consists in the selection of the anvils material; usually, diamond is the best choice for its extreme hardness. We chose to use the Sapphire (Al_2O_3), because diamond is not transparent to the IR radiation at the frequency (about 2500 cm^{-1}) resonant with the OD stretching mode. The two anvils must be glued to the cell support and their perfect alignment is crucial to avoid future breaking during compression steps. An illustration of the SAC structure used in our experiments are given in **Fig. 2.13**

Fig. 2.13 Scheme of the Sapphire Anvil Cell (SAC).

The second step is the indenting of the gasket. The gasket is made from Copper for the 98% and for the remaining by a Beryllium alloy; its composition is important to endure the compression phase. Indenting consists in printing the mark of the small face the conical window onto the gasket. We had to use diamond windows because sapphire does not resist the high pressures necessary for this step. Compression causes the reduction of the gasket thickness; its final value was 50 μm, starting from a thickness of 200 μm.

The last step is the creation of the hole in the gasket that will be the sample area; for this purpose, we used electro-erosion. In this technique, a charged tip produces an electric discharge close the desired point of the gasket; the latter is plunged into an oil, which prevents the delocalizing of the electric discharge.

The electro-erosion treatment is done in two phases. In the first step, we obtain a hole of about 300 μm. In order to avoid the reaction of water with the metals of the gasket, the hole rim has to be coated with sintered gold nanoparticles, what reduces appreciably the clear aperture: a second electro-erosion treatment is necessary to obtain a hole of diameter ≈ 250 μm.

Prior to sample loading, we insert in the hole some micro-fragment of Ruby, whose fluorescence emission is used to measure the pressure on the sample.

Finally, the sample is loaded and the cell is closed by a first compression step.

Measuring the internal pressure

Ruby (Al_2O_3) is a fluorescent material with absorption band around 500 nm: we use the second harmonic of a Nd-YAG laser to excite the Rubies inside the sample area.

The peculiarity of the Ruby material is that its emission frequency (**Fig. 2.14)** exhibits strong dependence on pressure and temperature conditions. Therefore, at any given temperature, it is possible to known the applied pressure by measuring its emission spectrum.
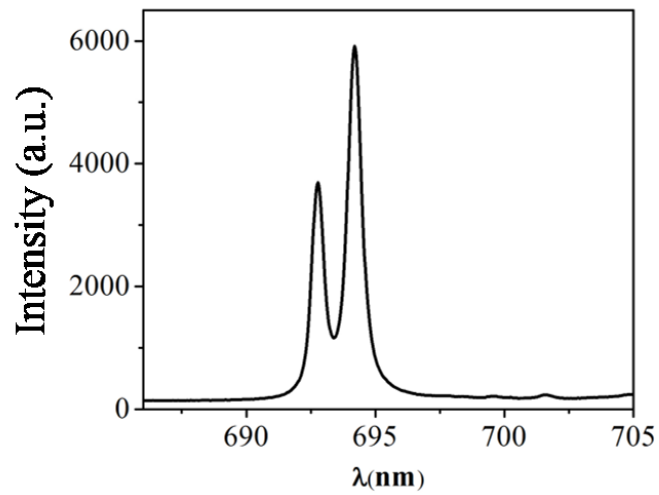
Fig. 2.14 The emission spectrum of Ruby shows two narrow band around 693 nm.

A Charge - Coupled Device (CCD) detector is used to record the Ruby emission spectrum. For the detector calibration, we use four emission bands of a mercury lamp.

3. Time-Resolved Optical Kerr Effect

3.1 Introduction

In time resolved Optical Kerr Effect (OKE) experiment the light pulses are not resonant with sample transitions. In the typical pump-probe scheme, the pump pulse induces in the sample some transient optical anisotropy, which is probed by a second laser pulse. More precisely, the linearly polarized pump pulse modifies the refractive index of the isotropic sample, inducing some transient birefringence. The probe pulse, linearly polarized at 45 ° from the pump, is blocked by a crossed polarizer (the *analyzer*) placed after the sample. Thus, in absence of the pump, no probe light reaches the detector. When the pump is switched on, the induced sample birefringence lets some fraction of the probe to cross the polarizer and reach the detector. The probe intensity, detected as a function of the of the pump-probe delay time, measures the relaxation of the optically induced birefringence. The experimental scheme is shown in **Fig. 3.1**
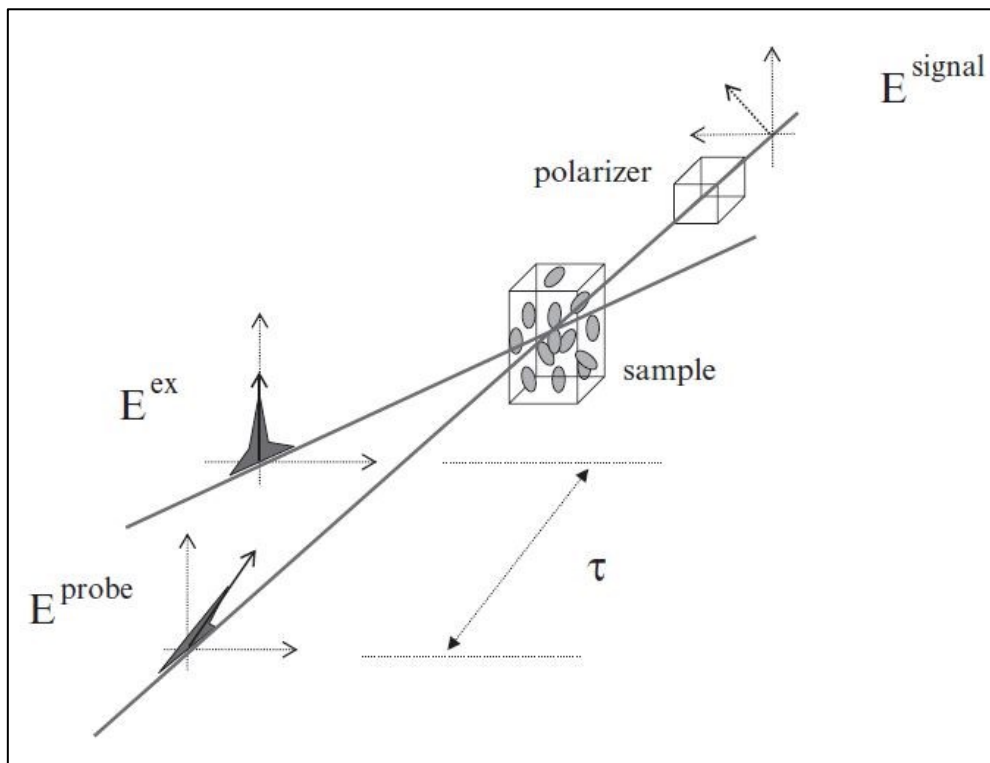

Fig. 3.1 Schematic view of the OKE experiment

Different models can be used to give a theoretical description of the OKE experiment; below we introduce an intuitive and a rigorous model to explain the experiment [12].

3.1.1 The time-resolved OKE signal

Here we describe the OKE effect in a relatively simple way, making use of the concept of non-linear index of refraction. We consider an optically isotropic medium, e.g. liquid or glass, and two linearly polarized pulses (see **Fig. 3.2)**.
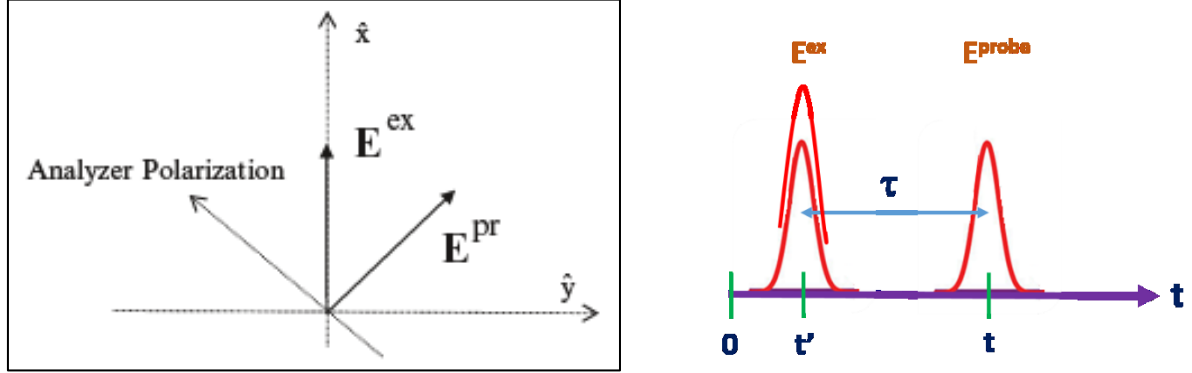

Fig. 3.2 Laser pulses polarization and temporal pulse sequence.

The pump pulse is polarized along the x-axis and its electric field

$$E^{ex}(z,t) = \hat{e}_x \cdot \varepsilon^{ex}(z,t) \cdot e^{i\omega\left(\frac{\eta_0}{c}z-t\right)} \tag{3.1}$$

where z is the propagation direction of the pulse, $\varepsilon^{ex}(t)$ is the pulse time envelope and η_0 is the isotropic refractive index of the sample. The pump pulse propagates in the material producing a transient linear birefringence; so, the sample becomes temporarily anisotropic.

We can write the modified refractive index as follows:

$$\eta_{ij} = \eta_0 + \Delta\eta_{ij}(t) \tag{3.2}$$

were the anisotropic term $\Delta\eta_{ij}$ has the form

$$\Delta\eta_{ij}(t) = \begin{pmatrix} \Delta\eta_{xx}(t) & 0 \\ 0 & \Delta\eta_{yy}(t) \end{pmatrix} \tag{3.3}$$

and i and j indicate the direction of polarization.

After the sample has been excited, the probe beam propagates in it probing the modified index of refraction. We assume that probe beam is linearly polarized at 45° respect to the pump beam; then, its electric field can be written as

$$E^{pr}(z,t) = \left[\hat{e}_x \cdot E_x{}^{pr}(z,t) + \hat{e}_y \cdot E_y{}^{pr}(z,t)\right]$$

$$= \hat{e}_x \cdot e^{i\frac{\omega l}{c}(\eta_0 + \Delta\eta_{xx}(t))} \cdot \varepsilon^{pr}(z,t) \cdot e^{i\left(\frac{\omega}{c}z - t\right)} + \hat{e}_y e^{i\frac{\omega l}{c}(\eta_0 + \Delta\eta_{yy}(t))}$$

$$\cdot \varepsilon^{pr}(z,t) \cdot e^{i\left(\frac{\omega}{c}z - t\right)}$$

(3.4)

where l is the length of the sample. The birefringence of the sample produces a modification of the probe phase different for the components along x and y axis: its polarization becomes (slightly) elliptical [22]. Now the analysing polarizer lets a fraction of the probe light pass through and reach the detector. Thus, the electric field obtained of the OKE signal is:

$$E^{sig}(z,t) = \left[\hat{e}_x \cdot E_x{}^{pr}(z,t) - \hat{e}_y \cdot E_y{}^{pr}(z,t)\right]$$

$$= (\hat{e}_x - \hat{e}_y) \cdot e^{i\frac{\omega l}{c}\eta_0} \cdot \left[e^{i\frac{\omega l}{c}(\Delta\eta_{xx}(t) - \Delta\eta_{yy}(t))}\right] \cdot \varepsilon^{pr}(z,t) \cdot e^{i\left(\frac{\omega}{c}z - t\right)}$$

(3.5)

Considering the small contribution of the exponent $\Delta\eta(t)$, the exponential can be expressed in a Taylor series, retaining only the first term, so that the previous equation is becomes:

$$E^{sig}(z,t) \propto i \cdot \left[\Delta\eta_{xx}(t) - \Delta\eta_{yy}(t)\right] \cdot \varepsilon^{pr}(z,t) \cdot e^{i\omega\left(\frac{\eta_0}{c}z - t\right)}$$

$$\propto i \cdot \left[\int dt' \cdot R_{OKE}(t - t') \cdot I_{ex}(t')\right] \cdot \varepsilon^{pr}(z,t) \cdot e^{i\left(\frac{\omega}{c}z - t\right)}$$

(3.6)

where R_{OKE} represents the material response function.

3.1.2 The Response Function

Time domain third order perturbation theory provides the expression for the time dependent response function R_{OKE} in equation (3.6).

From the expression of the i-th component of the polarization density p_i in terms of the i-th component of the permanent dipole m_i and of the components of the generalized susceptibilities χ, β, γ...

$$p_i = m_i + \chi_{ij} E_j + \beta_{ijk} E_j E_k + \gamma_{ijkl} E_j E_k E_l + \cdots$$

(3.7)

and including in the perturbation Hamiltonian the induced dipole terms

$$V(t) = -m_i E_i - \frac{1}{2}\chi_{ij} E_i E_j - \frac{1}{3}\beta_{ijk} E_i E_j E_k - \cdots$$

(3.8)

26

the response function is found to be proportional to the expectation value of the commutator of the linear susceptibility χ_{ij} at different times. $R(t)$ depends on four indexes (each can be *x, y, z*) and consists of two contributions, both proportional to the product of three electric fields. The purely electronic contribution, proportional to $\gamma_{ijkl}E_j E_k E_l$, is instantaneous (it is different from zero only when pump and probe pulse overlap) and does not carry any dynamical information. The contribution relevant to our investigation is the nuclear term, whose time evolution gives information on the dynamical properties of the molecular system. It is proportional to the commutator of the anisotropic linear susceptibility at different times:

$$R_{ijkl}(t) \propto \frac{i}{h} \cdot \theta(t) \cdot \langle [\chi_{ij}(t), \chi_{kl}(0)] \rangle \qquad (3.9)$$

where $\theta(t)$ is the Heaviside step function.

Only the nuclear contribution will be considered in the following.

It can be demonstrated that, in the classical limit, equation (3.9) is equivalent to the temporal derivative of the classical correlation function of the linear susceptibility:

$$R_{ijkl}(t) \propto -\frac{\theta(t)}{K_B T} \cdot \frac{\partial}{\partial t} \langle \chi_{ij}(t) \cdot \chi_{kl}(0) \rangle \qquad (3.10)$$

where K_B is the constant and T the absolute temperature.

If z is the propagation direction of the probe beam, making use of the symmetry relations for tensor quantities in an isotropic medium, we have :

$$R_{OKE} \propto R_{xyxy} = \frac{1}{2} \cdot (R_{xxxx} - R_{yyxx}) \qquad (3.11)$$

Therefore, the OKE response function (3.10) becomes:

$$R_{ijkl}(t) \propto -\frac{\theta(t)}{K_B T} \cdot \frac{\partial}{\partial t} \langle \chi_{xy}(t) \cdot \chi_{xy}(0) \rangle \qquad (3.12)$$

In condensed phases the susceptibility tensor can be separated in two parts:

$$\chi_{ij}(t) = \chi_{ij}{}^M(t) + \chi_{ij}{}^{IM}(t) \qquad (3.13)$$

where $\chi_{ij}{}^M$ is the molecular contribution, and $\chi_{ij}{}^{IM}$ describes the contribution of the intermolecular interactions, like hydrogen bond and induced-dipoles interaction.

The molecular term in (3.13) is the sum of the polarizabilities of the individual molecules:

$$\chi_{ij}{}^M(t) = \sum_n \alpha_{ij}^n(t) \tag{3.14}$$

n running over the ensemble of molecules.

The molecular susceptibility (3.14) depends, *via* the polarizability α, on the molecular rotational and vibrational degrees of freedom:

$$\alpha_{ij}^n(t) = \beta \cdot Q_{ij}^n(t) + \sum_{n,v} b_{ij}^{n,v}(t) \cdot V_v^n(t) \tag{3.15}$$

where β represents the anisotropic part of the equilibrium polarizability, Q_{ij}^n is the orientational tensor of molecule n, $b_{ij}^{n,v}$ is the first derivative of the polarizability with respect to the v normal coordinate V_v. Therefore, the correlation function of the linear susceptibility $C_{\chi\chi}^{OKE}(t)$ in eq. (3.12) can be written as

$$\langle \chi_{xy}(t) \cdot \chi_{xy}(0) \rangle = C_{\chi\chi}^{OKE}(t) = C^R(t) + C^V(t) \tag{3.16}$$

$$C^R(t) = \sum_{n,m} \beta^2 \cdot \langle Q_{xy}^n(t) \cdot Q_{xy}^m(0) \rangle \tag{3.17}$$

$$C^V(t) = \sum_{n,v} \langle b_{xy}^{n,v}(t) \cdot V_v^n(t) \cdot b_{xy}^{n,v}(0) \cdot V_v^n(0) \rangle \tag{3.18}$$

The correlation describes two different dynamics: rotational and vibrational. The rotational correlation function $C^R(t)$ includes the diffusive dynamics, responsible for the long-time relaxation of the OKE signal, and the short time oscillating contribution due to molecular librations. The vibrational correlation function $C^V(t)$ produces a fast oscillating modulation of the OKE signal, due to the beating of the involved normal coordinates.

That of the OKE signal described in equations (3.1) – (3.6), is a *homodyne detection*, i.e. the quadratic detector measures the square modulus of the electric field given in eq. (3.6). Thus, the homodyne signal is:

$$S_{homo}(\tau) \propto \int \left| E^{sig}(t) \right|^2 \cdot dt$$

$$\propto \int I_{pr}(t) \cdot dt \cdot \left[\int dt' \cdot R_{OKE}(t - t') \cdot I_{ex}(t') \right]^2 \tag{3.19}$$

Differently, if the signal field is superimposed to an identical local field, a *heterodyne detection* is obtained, with the following expression for the signal:

$$S_{hete}(\tau) \propto \int I_{pr}(t) \cdot dt \cdot \left[\int dt' \cdot R_{OKE}(t - t') \cdot I_{ex}(t') \right] \qquad (3.20)$$

Considering that pump and probe pulses are very short, compared to the timescale of the material dynamics, they can be approximated to delta functions; therefore, in the impulsive limit, the signal measured is:

$$S_{homo}(\tau) \propto [R_{OKE}(\tau)]^2 \cdot I_{pr} \cdot I_{ex}{}^2 \qquad (3.21)$$

$$S_{hete}(\tau) \propto [R_{OKE}(\tau)] \cdot I_{pr} \cdot I_{ex} \qquad (3.22)$$

In our set-up, we use the Heterodyne Detection (HD) scheme. In this configuration, a photodiode detects the interference of the signal field with the local field (E^{loc}):

$$S_T \propto |E^{sig} + E^{loc}|^2 = \left\{ |E^{sig}|^2 + |E^{loc}|^2 + 2 \cdot Re[E^{sig} \cdot E^{loc^*}] \right\} \qquad (3.23)$$

The total signal S_T is the sum of three contributions: the homodyne signal $|E^{sig}|^2$, the local field intensity $|E^{loc}|^2$ and the heterodyne signal; the first two terms can be eliminated using a differential photodiode detector. Therefore, the signal is:

$$S_{hete} \propto 2 \cdot Re[E^{sig} \cdot E^{loc^*}] = 2 \cdot \sqrt{(I^{sig} \cdot I^{loc})} \cdot cos(\Delta\phi) \qquad (3.24)$$

Where $\Delta\phi = \phi^{sig} - \phi^{loc}$ is the phase difference between signal and local fields. Performing two measurements with phase difference equal to 0 and π, we obtain opposite signs for the heterodyne signal, while signs are equal for the homodyne signal. Therefore, the difference of the two signals eliminates all the contributions that are insensitive to the phase change, and keeps the heterodyne signal only.

3.1.3 Fourier-Transform Deconvolution

The heterodyne-detected OKE signal in eq. 3.8 can be rewritten as the convolution of the response function $R_{OKE}(t)$ with an instrumental function $G^{(2)}(t)$ [23]:

$$S_{hete}(t) \propto \int dt_0 \cdot R_{OKE}(t - t_0) \cdot G^{(2)}(t_0) \qquad (3.25)$$

where $G^{(2)}(t)$ is the cross-correlation between pump and probe pulses:

$$G^{(2)}(t) \propto \int_{-\infty}^{+\infty} d\tau \cdot I_{ex}(t) \cdot I_{pr}(t - \tau) \tag{3.26}$$

According to the convolution theorem, the Fourier transform of the convolution of two functions is equal to the product of the Fourier transform of the individual functions. Therefore, in the frequency domain, the OKE signal becomes:

$$S(\omega) = R(\omega) \cdot G(\omega) \tag{3.27}$$

where $R(\omega)$ and $G(\omega)$ are the Fourier transforms of $R_{OKE}(t)$ and $G(t)$, respectively. $R(t)$ is an observable, so it is a real quantity; in contrast, $R(\omega)$ is a complex quantity:

$$R(\omega) = R'(\omega) + i \cdot R''(\omega) \tag{3.28}$$

$$R'(\omega) = \int_{0}^{+\infty} dt \cdot R(t) \cdot cos(\omega t) = Re[FT(R(t))] \tag{3.29}$$

$$R''(\omega) = \int_{0}^{+\infty} dt \cdot R(t) \cdot sin(\omega t) = Im[FT(R(t))] \tag{3.30}$$

Then, from eq. (3.27), the depolarized Raman spectral density $Sd(\omega)$ is obtained as the imaginary part of the Fourier transform of the time domain signal divided by the Fourier transform of the time domain instrumental function:

$$Sd(\omega) \propto Im[S(\omega)/G(\omega)] \tag{3.31}$$

The depolarized Raman spectral density $Sd(\omega)$ equals the depolarized spontaneous Raman spectral intensity $I_{Raman}(\omega)$ corrected for the Bose-Einstein factor:

$$Sd(\omega) = \frac{1}{2}\left[1 - exp\left(-\frac{\hbar \omega}{K_B T}\right)\right] I_{Raman}(\omega) \tag{3.32}$$

3.2 Experimental Methods

3.2.1 Optical set-up

The scheme of the HD-OKE setup assembled in our laboratory [12, 24, 25] is shown in **Fig. 3.3**.
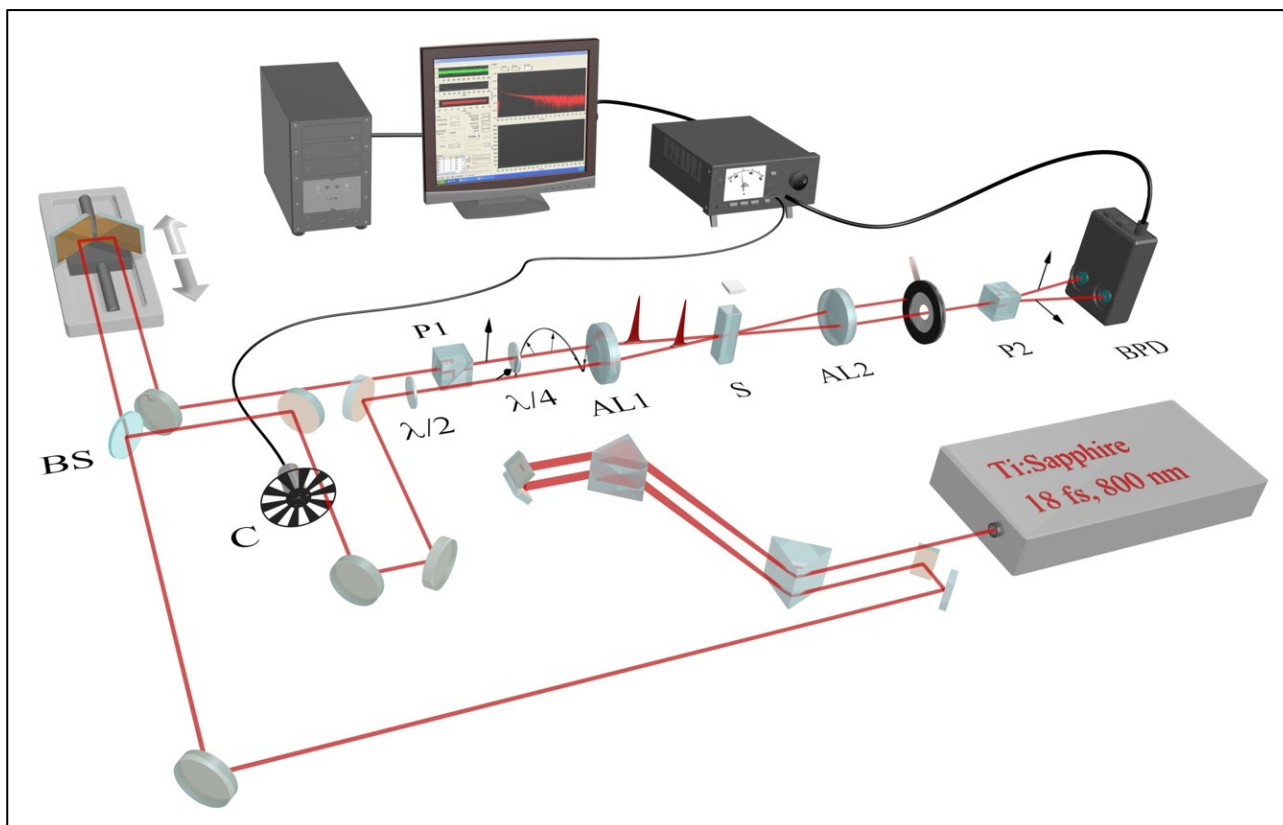
Fig. 3.3 Sketch of the setup used for the OKE experiment.

The source of ultrashort pulses is a self-mode-locked Ti:Sapphire laser (by Femtolasers, mod. Fusion), pumped by the second harmonic of a laser-diode-pumped Nd:YVO4 laser (Millennia V, by Spectra-Physics). It produces 20 fs horizontally polarized pulses, with 3 nJ peak energy, at the repetition rate of 76 MHz; the central wavelength is 800 nm and the bandwidth ∼ 90 nm. At the laser output, the pulses are compressed by passing in a pair of fused silica prisms; the compression stage is crucial to achieve good time resolution and to observe the oscillating Raman components over a sufficiently large frequency range. Indeed, pulses shorter than 50 fs have sufficient bandwidth to excite intramolecular Raman-active vibrations.

A beam splitter (BS) divides the laser beam into a strong pump beam (80%) and a weaker probe beam (20%). The pump pulse is chopped at 6 KHz and passes in a half wave plate ($\lambda/2$)

that, coupled to a calcite polarizer (P0) rotates its polarization by 45°. and then it arrives on the sample. The probe pulse is directed to the computer controlled optical delay line (ODL) that consists of a roof retroreflector mounted on a motorized stage. The delay line moves back and forth in a continuous manner at the velocity of 2.5 mm/s. The stage instantaneous position is obtained from the quadrature acquisition of He-Ne fringes by means of two photodiodes. The delayed probe passes in a polarizer (P1) oriented along the x-axis (horizontal) and in a quarter-wave plate ($\lambda/4$) rotated by $+45°$ in order to make the probe beam circularly polarized. In a circularly polarized beam the x (horizontal) and y (vertical) components have the same amplitude and $90°$ phase difference. After the sample, the vertical component passes through the vertically oriented analysing polarizer and is used as the local oscillator for the horizontal component for heterodyne detection; we remember that the OKE signal is also 90° out of phase with respect to the probe.

An achromatic doublet lens (L1, 75 mm focal length) makes both probe and pump beams coincident and focused in the sample. The probe beam is then collimated by the achromatic doublet lens (L2, 50 mm focal length) and sent to the Wollaston polarizer (P2) that separates spatially the horizontally and vertically polarized components. To perform heterodyne detection the signal field has to be beaten with the local oscillator. In this set-up the presence of an external local field is intrinsically guaranteed by the circular polarization of the probe beam and so an automatic heterodyne of the OKE signal is produced. Moreover, this optical set-up produces twin OKE signals with vertical and horizontal polarizations having opposite phase difference (0 and π) with the local field; a balanced photodiode detector operates the electronic subtraction of the two signals and extracts the HD-OKE signal.

A lock-in amplifier system, synchronized to the mechanical chopper, collects the output of the differential photodiode amplifier and performs an automatic subtraction of the background present in the signal. The lock-in integration time is 1 ms. The lock-in output is sent to the acquisition board (DAQ) that simultaneously acquires the translation stage position from the translation stage encoder and the lock-in output. Finally, the computer stores the signal and the stage position data. A further reduction of the noise in the data can be obtained by "super-heterodyning" the signal. This is achieved by performing two OKE measurements, corresponding to left and right circular polarizations of the probe, and taking the difference of the two.

Further operations can be done in order to improve the signal to-noise ratio and to remove possible artefacts. Spatial overlap of pump and probe pulses is achieved by focusing both beans trough a 40 μm pin-hole, placed at the position of the sample cell. The temporal coincidence is obtained by optimizing the sum frequency generation in a 20 μm thick BBO-crystal, placed at the pinhole position. The addition of a neutral filter along one of the analyser components allows compensating for small deviations of the circular polarization of the probe beam.

A further adjustment is required in order to minimize the depolarized signal produced by the static birefringence of the sample/cell system. With the pump beam blocked, we orient the axis of the quarter-wave plate parallel to the probe polarization. We detect, at the exit of the analyser, the orthogonally polarized signal, and rotate the wave-plate and the axis of the P1 polarizer to reach the absolute minimum of this signal. Finally, we rotate the quarter-wave plate back of 45° in order to restore the circular polarization of the probe beam.

3.2.2 Data acquisition program

The key point of the acquisition procedure is the real-time reading of the signal during the rapid scan of the optical delay line. The acquisition scheme in use allows for data acquisition with high absolute time resolution (1 fs), fast scanning velocity (0.1 mm/s) and long maximum time delay (several ns). In the real-time acquisition procedure, the delay line moves continuously, and the signal and the stage position are acquired simultaneously. All this reduces the acquisition time, thus substantially improving the statistics. Very good signal-to-noise ratio, with an extended dynamic range, is obtained in a single continuous scan of the optical delay line, with no need for pulse energy/duration adjustment.

4. Infrared experimental results

The sample used in the experiments is an aqueous solution of $NaClO_4$. In particular, I prepared solutions at different concentration of $NaClO_4$ in a 6% mixture of HOD in H_2O. Solutions were obtained in two steps: preparation of the water mixture, using 6 μl of D_2O and 199 μl of H_2O, and dissolution of the salt in the mixture.

The OD stretching mode of the HOD molecules provides the IR spectroscopic probe. With very good approximation, the OD stretch oscillator can be considered fully decoupled from the other HOD modes, so that the rate of intramolecular energy transfer is very low. On the other hand, the low concentration of HOD present in solution makes intermolecular energy transfer negligible.

4.1 Linear IR experiment

Before describing the transient measurements, it is useful to consider the linear FT-IR spectrum of the sample in the region we want to study. Our IR probe band, corresponding to the OD stretching mode, is peaked in the water mixture around 2520 cm^{-1}. All FT-IR spectra of SP solutions were taken using a cell equipped with two fluorite windows and a 100 μm spacer.

In $NaClO_4$ aqueous solutions two different sub-populations of water molecules are present: those having at least one ClO_4^- anion in the first shell (W_p) and those whose first solvation shell consists entirely of water molecules (W_w). The presence of these two ensembles of water molecules produces two distinct bands with central frequencies at 2630 cm^{-1} (for the W_p molecules) and 2520 cm^{-1} (for the W_w molecules). **Fig.4.1** shows the FT-IR spectrum of 6M Sodium Perchlorate solution.
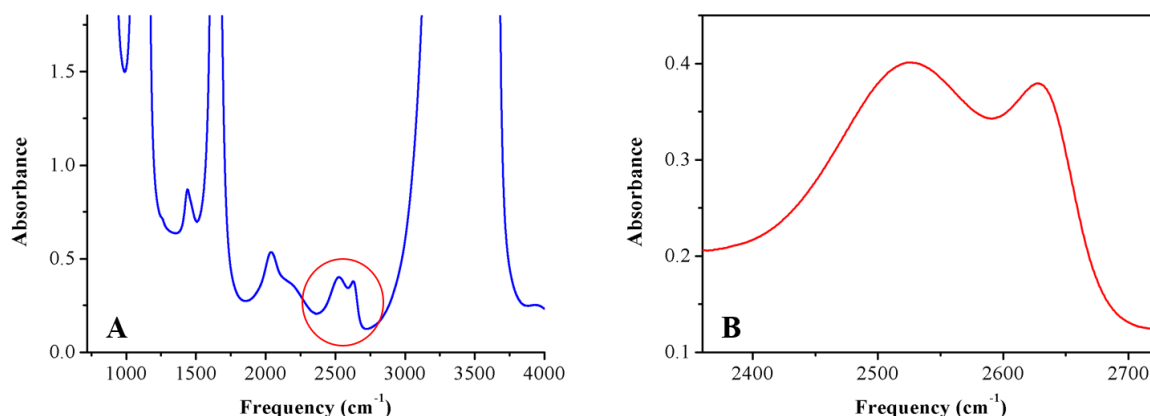
Fig. 4.1 A) FT-IR spectrum of a 6M SP solution. The H_2O absorption bands are in saturation. We focus our attention on the OD stretching band at 2500 cm^{-1}. **B)** Zoom of the band of interest; it consists of two different components, corresponding to the W_w and W_p sub-populations.

In the figure, the out-of-scale bands are relative to neat water (H_2O) absorption. In the region of interest, 2000-3000 cm^{-1}, the spectrum shows: the HOD combination band of bending and libration at 2000 cm^{-1}, the OD stretching mode of the two sub-populations at 2520 e 2630 cm^{-1} and the tail of the antisymmetric stretching of H_2O centred at 3500 cm^{-1}.

It is known that the OD stretching frequency changes in function of the strength of hydrogen bonds. Therefore, in Sodium Perchlorate solutions, the OD frequency of W_p is higher than that of W_w in consequence of the much weaker hydrogen bond that HOD forms with ClO_4^- in comparison with that formed with water molecules.

Thanks to the almost complete separation from the HOD combination band peaked at ~2000 cm^{-1}, it is possible to use the OD stretching band as a probe of the dynamics of the HDO molecules, neglecting the presence of other contributions. Moreover, the spectral separation of the two water subpopulations allows following their dynamics separately. This is a not so frequent feature, which is due to the particularly low propensity of ClO_4^- to form H-bonds: for instance, in the IR spectra of Carbonate and Sulphate ions show a unique band for the OD stretching mode, what makes the spectroscopic distinction of two water ensembles practically impossible.

I employed Gaussian deconvolution for the analysis of the OD absorption band profile. After a linear baseline subtraction, I used two (three for high concentrations) Gaussian functions for the fit. **Fig. 4.2** gives an example of the spectral deconvolution.
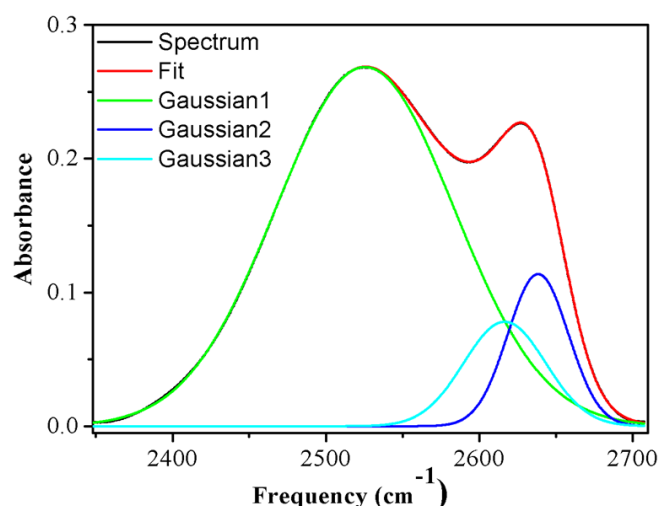
Fig. 4.2 FT-IR spectrum of a 5M NaClO$_4$ solution (black line). The OD Ww band is simulated by a Gaussian function (green line) centred at 2520 cm^{-1}, the OD Wp band is described by a Gaussian function (blue line) centred about 2630 cm^{-1} and another Gaussian (cyan line) function is necessary to have a good fit of data. The red line is the sum of all the Gaussian

The figure displays the OD region of the FT-IR spectrum of a 5M solution. At this concentration, three Gaussian functions are necessary to reach a fit of the data. We use one Gaussian profile peaked at 2525 cm^{-1} for the OD stretching of the W_w molecules, and two gaussians, centred at 2630 and 2617 cm^{-1} for the band relative to the W_p molecules. The need for the band 2617 is probably to be associated to the presence of a relevant population of associated ionic species at high concentration. In fact, the spectrum of dilute solutions can be reproduced using only two bands, corresponding to W_w and W_p water molecules. However, for the sake of uniformity, we adopt the three Gaussian fit for of all samples, and focus our analysis on the OD stretching band of the W_w molecules.

4.1.1 Concentration effect

In **Fig. 4.3**, we illustrate the OD stretching band for solutions at different concentration. We extract from the fit two spectral quantities: central frequency and linewidth of the band of interest.
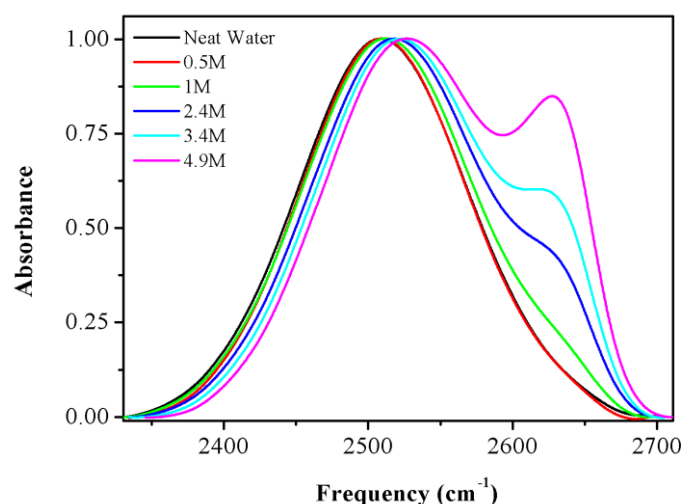
Fig. 4.3 Zoom of the OD stretching band of linear spectra, for neat water (black) and for SP solution at different concentration: 0.5 (red), 1 (green), 2.4 (blue), 3.4 (cyan) and 4.9 M (magenta). All spectra are normalized on the maximum of the W_w band.
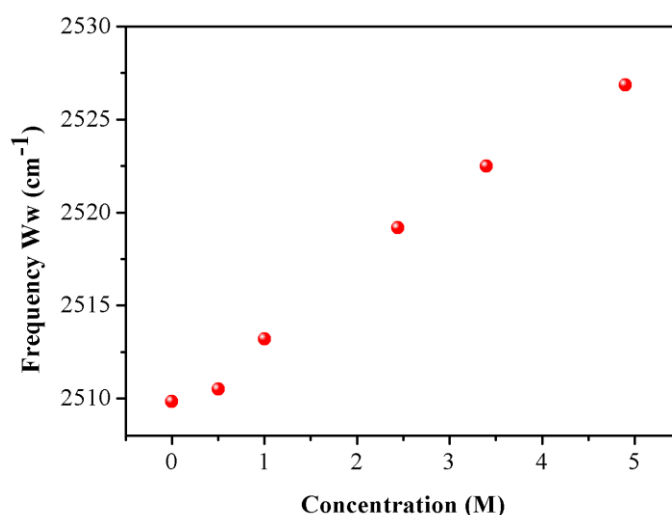
Fig. 4.4 Central frequency of the OD band, relative to W_w subpopulation, for neat water and for different concentration of $NaClO_4$.

The spectra in the region of OD stretch display two bands around 2520 and 2630 cm^{-1}, corresponding, respectively, to at the OD stretching mode of bulk water (W_w) and of water molecules in the first solvation shell of the perchlorate anion (W_p). As $NaClO_4$ concentration increases, the low frequency peak shifts to the blue, while the higher frequency peak does not move and increases in amplitude. We underline that water molecules that form the Na^+ hydration shell are not spectrally distinguishable from the bulk ones; in fact, cations interact

mostly with the oxygen atom of water and their effect on the OD stretching frequency is practically undetectable.

Fig. 4.4 shows the blue shift of the band with increasing salt concentration. The central frequency of the band goes from 2510 cm^{-1} in neat water, to 2527 cm^{-1} in 4.9 M solution. MD simulations [26] showed that this effect is mostly due to the large electric field produced by the ionic charges (Stark effect) in the liquid, which increases with the salt concentration.

The FWHM linewidth data for different concentrations, collected in **Fig. 4.5,** show that the linewidth is only very weakly dependent on concentration. Its value is almost constant ($\approx$ 140 cm^{-1}) up to 2.5 M; a moderate decrease (about 2 cm^{-1}) shows up beyond that concentration.
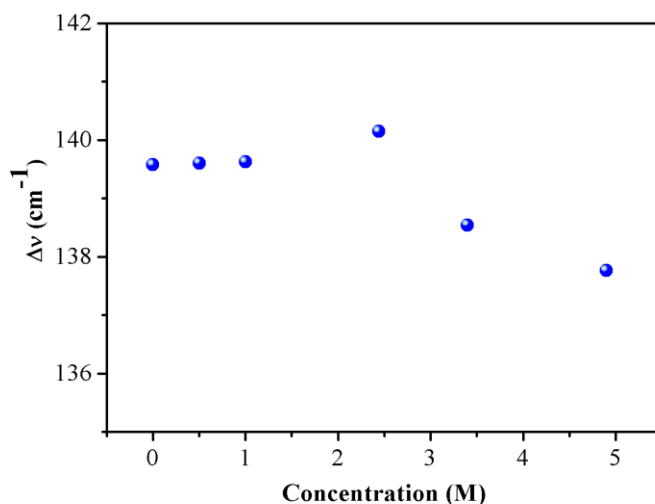
Fig. 4.5 FWHM linewidth of the OD band of W$_w$ molecules as a function of concentration.

4.1.2 Pressure effect

The pressure induced changes of the OD stretching band of a 2 M NaClO$_4$ solution is shown in **Fig. 4.6**. A red shift with increasing pressure of the peak around 2500 cm^{-1}, corresponding to W$_w$ molecules, is evident.
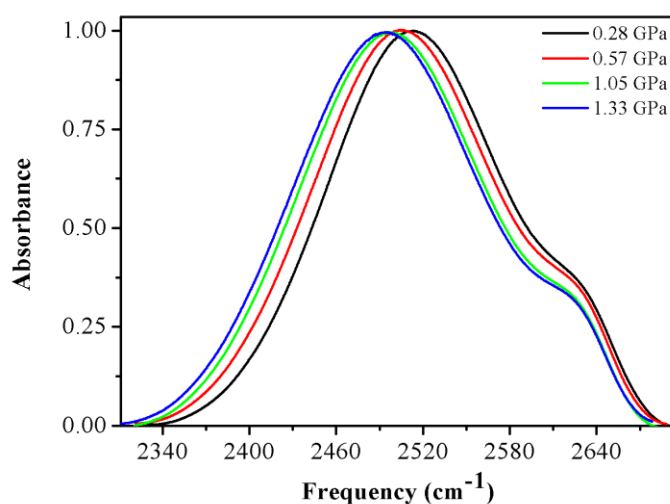
Fig. 4.6 Zoom on OD stretching band of 2.4M solution for different values of pressure: 0.28 (black), 0.57 (red), 1.05 (green) and 1.33(blue) GPa. All the spectra are normalized on the maximum of the W_w band.

The data collected in **Fig. 4.7** confirm that this effect is common to all the concentrations, including neat water. No relevant pressure dependence is instead observed for the W_p band around 2630 cm^{-1}.
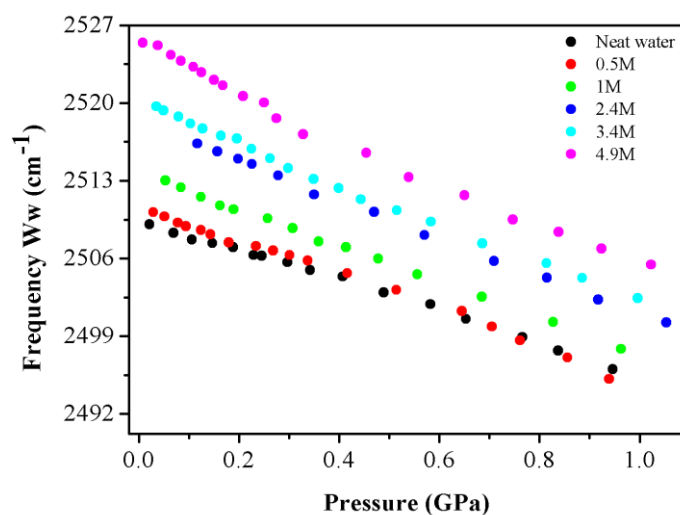
Fig. 4.7 Central frequency of the Gaussian used to fit the OD band of W_w molecules, as a function of pressure for different concentrations: neat water (black circles), 0.5 M (red circles), 1 M (green circles), 2.4 M (blue circles), 3.4 M (cyan circles) and 4.9 M (magenta circles).

Pressure induced line broadening is common to all concentrations. The pressure dependence observed for the 0.5 and 1M solutions is practically indistinguishable from that of neat water, which has been shown [10] to have a definite change of slope around 0.2 GPa (better visible when the linewidth data are plotted against density). **Fig. 4.8** shows that this strong non-linearity of the linewidth pressure dependence decreases with increasing concentrations, and becomes hardly appreciable for the 4.9 M solution.

Fig. 4.8 Pressure dependence of the linewidth of the W_w band for different concentrations.: neat water (black circles), 0.5 M (red circles), 1M (green circles), 2.4 M (blue circles), 3.4 M (cyan circles) and 4.9 M (magenta circles).

The data of **Fig. 4.8** are collected in **Table 4.1.**

Table 4.1 Linewidth for different systems in function of pressure.

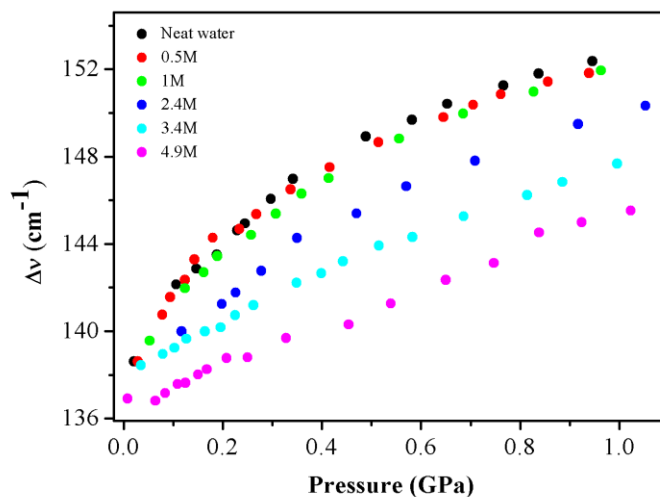| Neat water		0.5 M		1 M		2.4 M		3.4 M		4.9 M	
P (GPa)	FWHM (cm⁻¹)	P (GPa)	FWHM (cm⁻¹)	P (GPa)	FWHM (cm⁻¹)	P (GPa)	FWHM (cm⁻¹)	P (GPa)	FWHM (cm⁻¹)	P (GPa)	FWHM (cm⁻¹)
0.02	138.6	0.03	138.6	0.05	139.6	0.12	140.0	0.03	138.4	0.008	136.9
0.11	142.1	0.08	140.7	0.12	142.0	0.20	141.2	0.08	138.9	0.08	137.2
0.15	142.9	0.09	141.6	0.16	142.7	0.23	141.8	0.10	139.2	0.11	137.6
0.19	143.5	0.12	142.3	0.19	143.4	0.278	142.8	0.13	139.7	0.12	137.6
0.23	144.6	0.14	143.3	0.26	144.4	0.35	144.3	0.16	140.0	0.15	138.0
0.24	144.9	0.18	144.3	0.31	145.4	0.47	145.4	0.20	140.2	0.17	138.2
0.30	146.1	0.23	144.7	0.36	146.3	0.57	146.6	0.22	140.7	0.21	138.8
0.34	147.0	0.27	145.4	0.41	147.0	0.71	147.8	0.26	141.2	0.25	138. 8
0.49	148.9	0.34	146.5	0.56	148.8	0.92	149.5	0.35	142.2	0.33	139.7
0.58	149.7	0.42	147.5	0.68	150.0	1.05	150.3	0.40	142.6	0.45	140.3
0.65	150.4	0.51	148.7	0.83	151.0	1.21	151.3	0.44	143.2	0.54	141. 3
0.77	151.2	0.64	149.8	0.96	151.9	1.33	151.6	0.51	143.9	0.65	142.3
0.84	151.8	0.70	150.4	1.21	152.9	1.46	152.2	0.58	144.3	0.75	143.1
0.95	152.4	0.76	150.8	1.40	153.6			0.69	145.2	0.84	144.5
		0.86	151.4	1.55	154.1			0.81	146.2	0.92	145.0
		0.94	151.8					0.88	146.8	1.02	145.5
		1.07						1.00	147.7	0.06	136.8

4.2 Broad-band IR transient absorption experiment

The experimental set-up for this experiment is described in detail in the **Section 2.4**.

As already described in **Section 2.1**, the non-linear differential transient spectrum contains a positive and a negative band; ESA gives rise to the positive band, and SE and B cause the negative one.
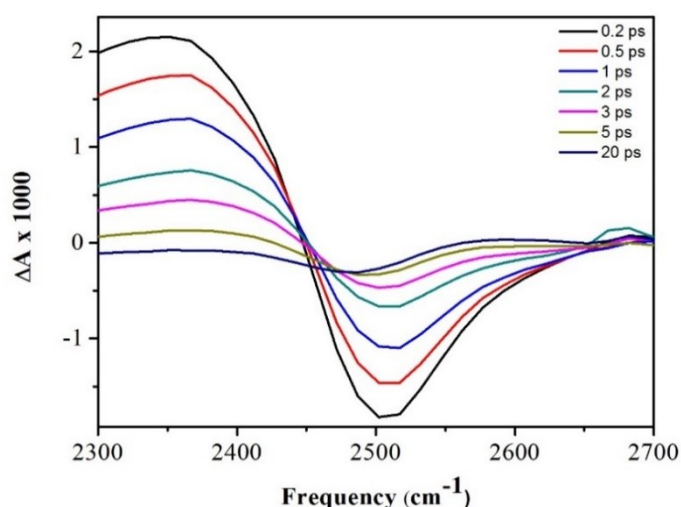

Fig. 4.9 Room pressure transient spectra, for a 2M solution, recorded at different delay times between pump and probe: 0.2, 0.5, 1, 2, 3, 5 and 20 ps.

In **Fig. 4.9**, we illustrate an example of transient spectra recorded at the magic angle, for different time delays between pump and probe pulses. The figure shows the decay of the signal with delay time; the exponential decay is due to the relaxation of the population of the excite state.

Another important feature of **Fig. 4.9** is the presence of a residual differential absorption at delay time as long as 20 ps; at this long delay, the OD stretching excited state is fully relaxed, and the residual contribution cannot be related to the HOD dynamics of interest for this work. It is attributed to a thermal effect and it is typical of liquids that present hydrogen bond network. Its origin is a photochemical modification of the sample that persists for relatively long time, resulting from the energy deposited by the pump pulse. Indeed, the energy absorbed by the OD stretching relaxes very quickly and dissipates through the hydrogen-bonded network. The resulting local heating causes partial breaking of the hydrogen bonds. The spectral signature of this thermal effect observed in our transient spectra can be easily determined by measuring the difference of the static FT-IR spectra of water taken at two different temperatures [27].

From the literature, is known that in the transient spectrum of neat water the thermal contribution grows exponentially with a time constant ($\tau*$) of 800 fs; however, no information is available for the rise time in salt solutions. It has been shown [28] that the growth kinetic equation follows the equation

$$\Delta A_T(\omega, t) = \Delta A_{end}(\omega) \cdot \left\{ \frac{\tau*}{\tau_v - \tau*} \cdot e^{-t/\tau*} - \frac{\tau_v}{\tau_v - \tau*} \cdot e^{-t/\tau_v} + 1 \right\} \tag{4.1}$$

where ΔA_{end} is the differential spectrum measured at delay times longer than 20 ps, $\tau*$ is the time constant for photoproduct formation and τ_1 is the lifetime of the OD excited state.

Thus, the signal measured in our experiments is the sum of the "true" signal and of the thermal contribution. We then fit the data using the following equation:

$$\Delta A(\omega, t) = N_1(0) \cdot [\sigma_{12}(\omega) - 2 \cdot \sigma_{01}(\omega)] \cdot e^{-t/\tau_v} + \Delta A_T(\omega, t) \tag{4.2}$$

where N_1 is the population of the excited state and $\sigma_{ij}(\omega)$ is the spectral cross-section. We obtain the signal fit, using **Eqs. 4.1** and **4.2,** imposing the spectral cross sections constant. By the fit, we obtain the value of $\tau*$ and τ_v and then, we subtract the thermal term (ΔA_T) from the data. **Fig. 4.10** shows the spectrum of the thermal contribution ($\Delta A_{end}(\omega)$) obtained as the difference as the difference of two FT-IR spectra taken at a temperature difference of 20 K.
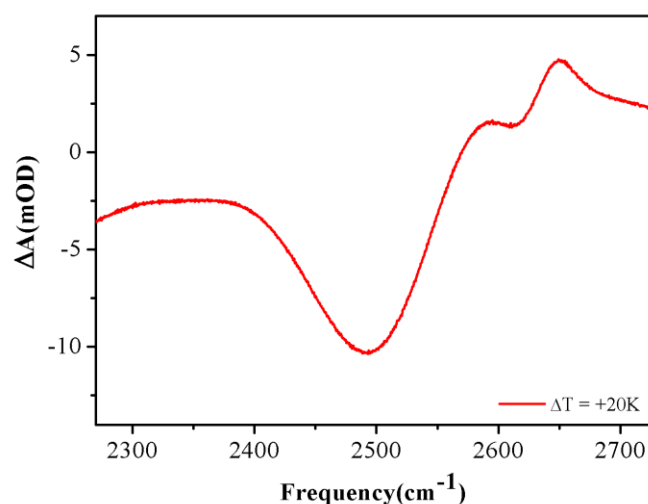
Fig. 4.10 Difference spectrum obtained as the difference of two static FT-IR spectra of a 6M solution at a temperature difference of 20 degrees

The spectral profile is very similar to that obtained for neat water [10]. The frequency and shape the of narrow band around 2670 cm^{-1} correspond to those of the band assigned to the W_p molecules: its increase with rising temperature corresponds to the change in the equilibrium constant for the in/out exchange reaction in the first solvation shell.

Moreover, the time constant (τ^*) for the formation of the photoproduct in the ionic solution is longer than that obtained in neat water (0.9 ps); its value changes with salt concentration and pressure. In **Tables 4.2** and **4.3** we collect the values of τ^* measured at different concentrations and pressures.

Table 4.2 Time constant τ^* for the formation of the photoproduct at different concentrations

Concentration (M)	τ^* (ps)
0	0.9
0.5	1.4
0.9	2.0
2	2.1
3.4	2.8
4.9	6.6

Table 4.3 Time constant τ^* for the formation of the photoproduct as a function of the applied pressure, for 0.5 and 2 M solutions

Pressure (GPa)	τ^* 0.5 M (ps)	Pressure (GPa)	τ^* 2 M (ps)
0.0001	1.4	0.0001	2.1
0.09	1.5	0.16	2.2
0.20	1.5	0.20	2.5
0.33	1.3	0.31	2.2
0.57	1.4	0.52	2.3
0.72	1.5	0.78	1.4
0.94	1.4	1.20	1.5
1.25	1.4		

From the transient absorption data, corrected for the thermal contribution, we can finally extract the delay time dependence of the isotropic absorbance and of the spectral anisotropy (**Eqs. 2.5** and **2.6**), which provide the lifetime of the excited state and the rotational relaxation time of the HOD molecules.

The findings from experiments and from computer simulations are described in detail in the next two paragraphs.

4.2.1 Concentration effect

In this work, we are mostly interested in the analysis of bulk water dynamics. In general, we use data recorded about 2500 cm^{-1}, corresponding to the minimum of the lower frequency negative peak of the transient spectrum. With good approximation, data measured at this frequency concern only the W_w molecules.

We performed pump-probe experiment with pulse polarization control; the observables of this experiment are molecular orientational dynamics and vibrational relaxation dynamics.

Vibrational relaxation

The decay of the intensity of the isotropic (magic angle) differential absorbance (see **Eq. 2.5**) measured in transient absorption experiments gives the lifetime of the excited state. As already noticed, first we had to correct the row data for the thermal contribution: **Fig. 4.11**

shows the delay time dependence of the isotropic absorbance in presence (black) and in absence (red) of the thermal contribution.
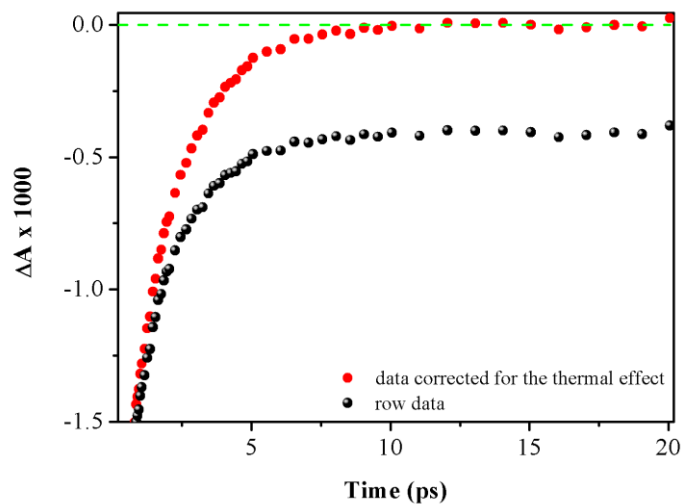
Fig. 4.11 Intensity decay of the negative band at 2500 cm^{-1} for the 0.5M solution. The black dots represent data obtained from row data, the red ones are data corrected for the thermal effect.

An exponential fit to the decay curves gives the O-D lifetimes (τ_v) for neat water and for different concentrations of NaClO$_4$ solutions reported in **Fig. 4.12**.

Fig. 4.12 Lifetime (τ_v) of the OD stretching vibration as a function of NaClO$_4$ concentration.

Two different regimes are evident in the figure. In diluted solutions, up to 1 M, the vibrational relaxation is essentially independent of the concentration, with a lifetime τ_v of

about 1.7 ps. In contrast, in solutions above 2 M the OD stretching lifetime increases appreciably with the concentration, reaching a value of about 2.2 ps at 6 M.

The data of **Fig. 4.12** are summarized in **Table 4.4**.

Table 4.4 OD stretching lifetime τ_v for different salt concentrations

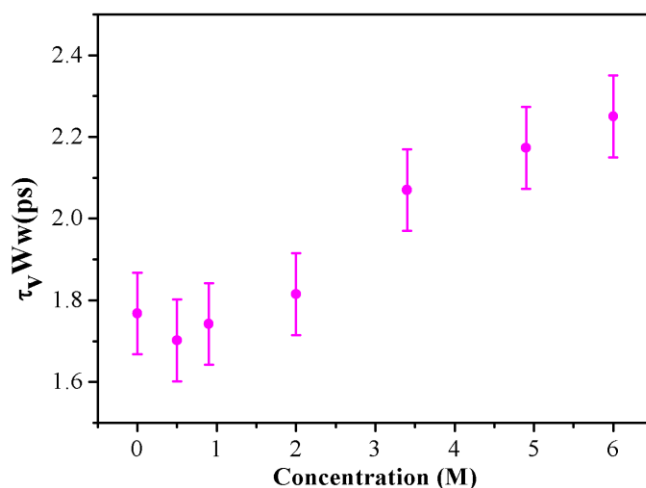| Concentration (M)	τ_v (ps)
0	1.8
0.5	1.7
0.9	1.7
2.0	1.8
3.4	2.1
4.9	2.2
6.0	2.2

Spectral anisotropy

The time evolution of the spectral anisotropy provides direct information on the rotational dynamics of the water molecules; we remember that to calculate the spectral anisotropy value is necessary to record transient signal in parallel and perpendicular configurations, see **Section 2.2** for details. The orientational correlation time is obtained through the fit of data with an exponential function.
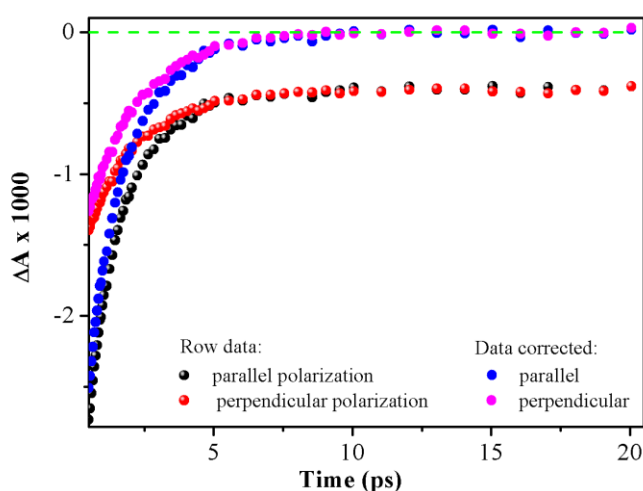

Fig. 4.13 Intensity decay of parallel and perpendicular signal recorded at 2500 cm^{-1} for the 0.5M SP solution. The black and red points represent the data measured; instead, the blue and magenta ones are data before corrected for thermal effect.

According to **Eq. 2.5** and **2.6**, the time dependence of the spectral anisotropy is obtained from transient absorption measurements in parallel and perpendicular polarization configurations, after correction for the thermal contribution. **Fig. 4.13** shows the effect of the correction on the absorbance decay curves for the 0.5 M sample.

The spectral anisotropy decay for perchlorate solutions at different molar concentrations is reported in **Fig. 4.14**.
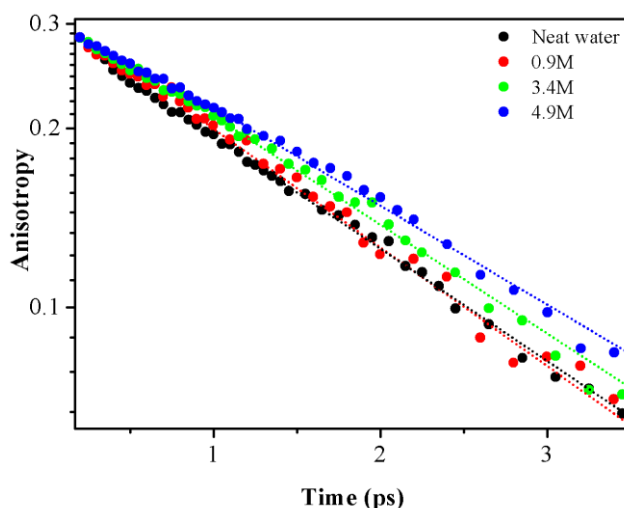
Fig. 4.14 Spectral anisotropy decay measured at different concentrations (semi-log plot): neat water (black circles), 1M (red circles), 3.4M (green circles) and 4.9M (blue circles); the dotted lines are exponential fits. All data concern the negative band.

In the figure, we report the anisotropy decay for neat water and for solutions of different concentrations. The kinetic traces are obtained from the peak intensity of the negative band around 2500 cm^{-1}; thus, we are analysing the orientational dynamics of bulk water molecules.

The apparent slowing down of the HOD rotational dynamics with increasing concentration is confirmed by the exponential fit. In **Fig. 4.15** and **Table 4.5**, we collect the exponential rotational time constants (magenta symbols) obtained at different concentrations.
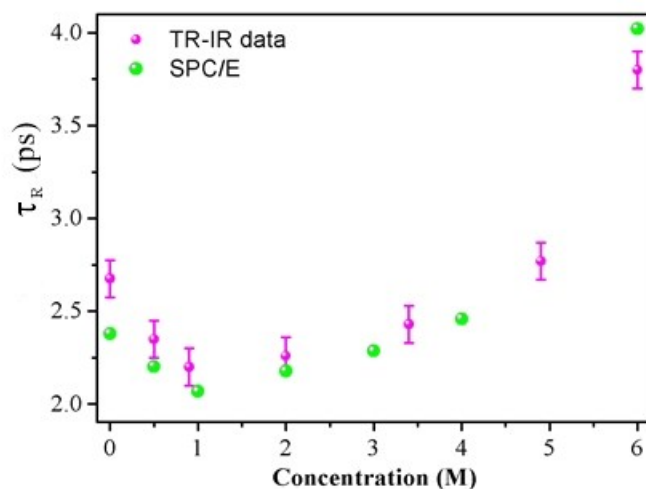
Fig. 4.15 Reorientation time τ_R of W_w molecules at different concentrations. The experimental data (magenta symbols) correspond to the intensity of the transient negative band at 2500 cm^{-1}. The calculated data (green) are obtained from MD simulation.

Similarly to the behaviour of the vibrational lifetime, also for the rotational time constant τ_R, two different dynamical regimes are evident. For diluted solutions, the orientational dynamics speeds up with increasing concentration up to ~1.5 M; at higher concentrations the opposite trend appears, as the rotational dynamics slows down when molarity increases.

We notice the good accordance of the experiment results with the simulated data. We perform Molecular Dynamics (MD) simulations on NaClO$_4$ aqueous solutions and in particular, we use the SPC/E model [29] for water and the potential proposed by Heinje et al. [30] for NaClO$_4$. Further details of the simulation procedures will be given in the **Section 4.4**.

Table 4.5 Concentration dependence of the reorientation time τ_R

Concentration (M)	τ_R (ps)
0	2.7
0.5	2.3
0.9	2.2
2.0	2.3
3.4	2.4
4.9	2.8
6.0	3.8

4.2.2 Pressure effect

Investigating the influence of pressure on the water dynamics requires the use of a gas membrane cell; in the present case, we use a Sapphire Anvil Cell (SAC), which is transparent in the mid-IR region (see **Section 2.4.5** for further details). We perform transient one- and two-dimensional spectroscopy experiments, in the pressure range of (0.1-1.3) GPa, on $NaClO_4$ aqueous solutions at concentration 0.5, 2 and 6 M.

The preparation of the sample in a high pressure cell is not trivial; we illustrate the procedure in detail in **Section 2.2**. Some complication for the high-pressure transient measure derives from the small dimensions of the sample area (~250 μm diameter). In particular, the far tails of the (roughly Gaussian) pump beam are scattered by the edge of the aperture; this results in some scattered light overlapping the transient signal. Usually, we tilt of a little angle the sample cell to minimize the scattering light reaching the MCT detector.

The spectra collected in **Fig. 4.16 A-C** account for the pressure-induced changes of the OD stretch band for different perchlorate solutions.

The negative band of the 0.5M solution, with one peak centered at about 2500 cm^{-1}, is almost identical to that of neat water (W_w). At 2 M perchlorate concentration a second peak at ~2620 cm^{-1}, due to HOD molecules in the anion first solvation shell (W_p), appears; it becomes prominent for the 6M solution.
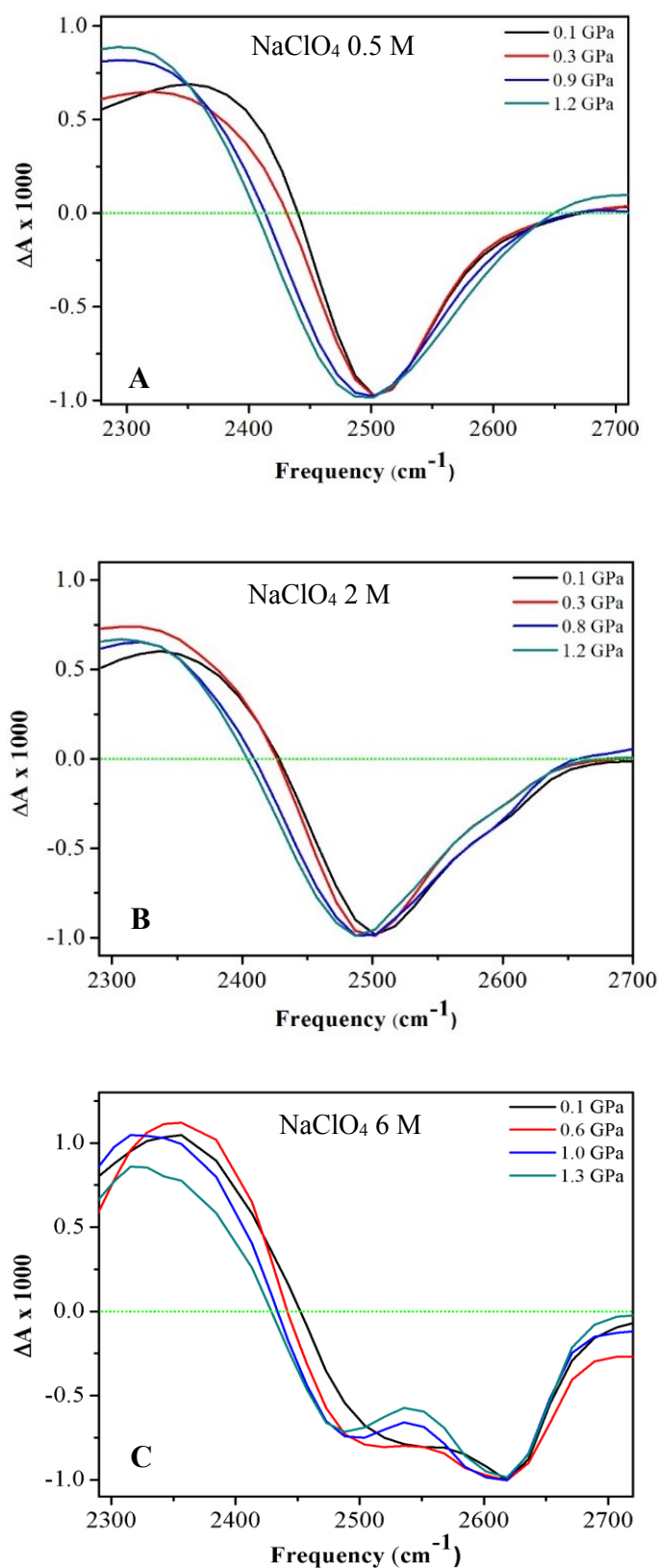
Fig. 4.16 A) Transient IR spectra in the OD stretch region, recorded at 500 fs of delay time, for different pressures, on a NaClO$_4$ 0.5 M aqueous solution. **B)** the same, for a 2 M solution. **C)** the same, for a 6 M solution.

In 0.5M and 2M solutions increasing pressure causes a moderate red shift of the band around 2500 cm^{-1} (corresponding to bulk water). In the 6M solution the frequency downshift is definitely larger: the W_w band moves from 2524 cm^{-1} at 0.1 GPa to 2488 cm^{-1} at 1.3 GPa. This red shift of the OD band is consistent with the strengthening of the HBs network, caused by the sample compression. In contrast, the frequency ($\sim$2620 cm^{-1}) of the W_p water molecules in the perchlorate solvation shell is essentially pressure-independent. Note that, consequently, the separation between the two bands increases with pressure.

Vibrational relaxation

After subtraction of the thermal contribution, we obtain the OD stretching lifetime at different pressures from the exponential fit to the delay time dependence of the absorbance measured at 2500 cm^{-1}. The lifetimes for the 0.5 M and 2 M solutions are plotted in **Fig. 4.17**, together with those of neat water.
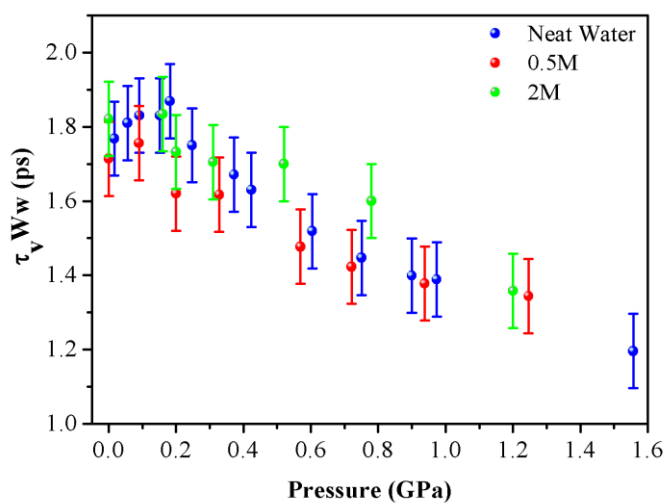
Fig. 4.17 OD stretching lifetime as a function of pressure. The pressure effect is very similar for all concentrations (neat water, 0.5 M and 2 M solutions).

For 0.5 and 2 M solution, in full analogy with what previously observed in neat water [10], the pressure dependence of the OD stretch lifetime has two distinct regimes, with a sharp slope change around 0.2 GPa. In the pressure range 10^{-4} – 0.2 GPa, the lifetime is almost constant: the slight apparent increase remaining within the experimental error. Conversely, further pressure increase leads to a substantial speed up of the population relaxation.

51

At variance with the analysis just described, for the NaClO$_4$ 6 M solution we chose to measure the OD stretch lifetime from the delay time dependent intensity of the positive band, measured at 2342 cm^{-1}.

Fig. 4.18 Transient spectrum recorded at room pressure and delay time of 500 fs for a SP solution 6M.

Two are the reasons for this choice. First, the high intensity of the W$_p$ band at 2620 cm^{-1} makes difficult discriminating the contributions of the sub-population at 2500 cm^{-1} (see **Fig. 4.18)**. Second, as the OD stretching lifetime of the W$_p$ molecules i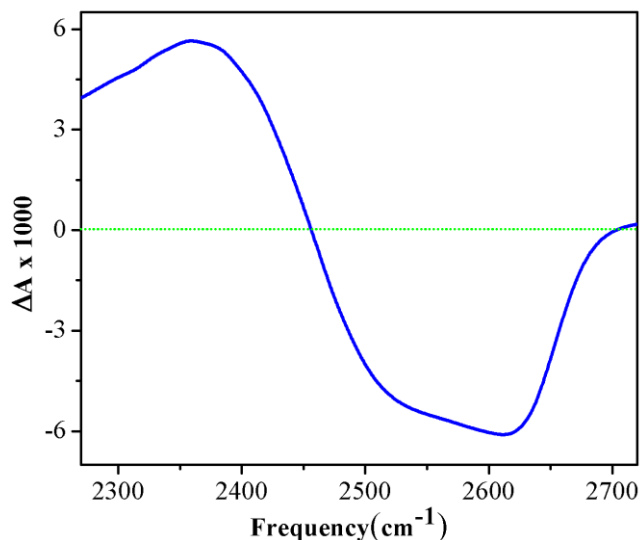s longer than that of the W$_w$ ones, any residual contribution of the former affects the kinetic trace of the W$_w$ molecules. This effect is negligible for diluted system, but is relevant for high concentrations.

By the other side, we underline that the positive band relative to the HOD transient spectrum is very close, in frequency, to the combination band of bending and libration (2000 cm^{-1}); so, the tail of the combination band affects the HOD dynamics. The presence of the band at 2000 cm^{-1} is the reason because we prefer to analyse the spectrum negative band for the more diluted systems.

Fig. 4.19 shows that, as expected according to the room pressure results, the values of the OD stretching lifetime relative to the W$_w$ molecules, for the 6 M solution are, at all pressures, remarkably longer than those of the less concentrated solutions at the corresponding pressures. Moreover, the excited state lifetime of the W$_p$ molecules, for all pressures, is longer of the lifetime relative of bulk water, in consequence of the weaker H-bonds. In 6M solutions, the pressure dependence of the lifetime is qualitatively similar to that measured at lower

concentrations (see **Fig. 4.17**). The excited state lifetime, after a small (~10%) sharp increase around 0.1 – 0.3 GPa, decreases with a very small slope. We underline that the effect of pressure on the OD stretching lifetime is similar for both the water subpopulations (see **Fig. 4.19**).

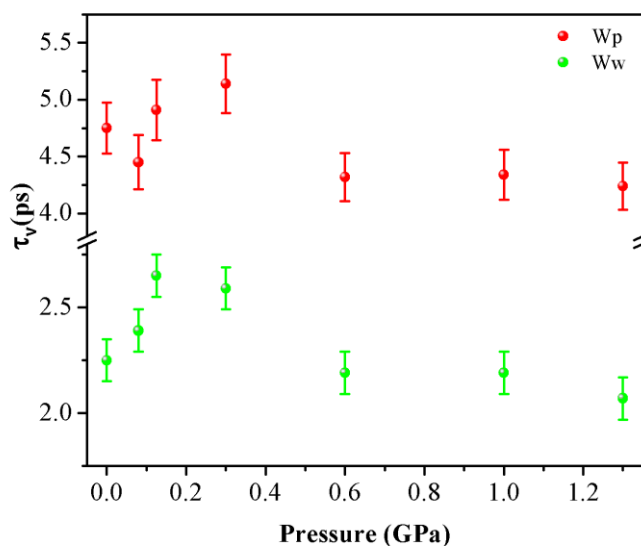**Fig. 4.19** OD stretch lifetime τ_v as a function of pressure for the 6 M solution for the two subpopulations W_w (green) and W_p (red). The data for W_w molecules are extracted from the positive band at 2342 cm^{-1}. Data for the W_p molecules are acquired at 2636 cm^{-1}.

The values of the lifetime for the different concentrations are given **in Table 4.6** as a function of pressure.

Table 4.6 Vibrational lifetimes τ_v for the different concentrations as a function of pressure

Water		0.5 M solution		2M solution		6 M solution	
Pressure (GPa)	τ_v (ps)	*Pressure (GPa)*	τ_v (ps)	*Pressure (GPa)*	τ_v (ps)	*Pressure (GPa)*	τ_v (ps)
0.02	1.8	0.0001	1.7	0.0001	1.8	0.0001	2.2
0.06	1.8	0.09	1.8	0.16	1.8	0.08	2.4
0.09	1.8	0.20	1.6	0.20	1.7	0.12	2.6
0.15	1.8	0.33	1.6	0.31	1.7	0.30	2.6
0.18	1.9	0.57	1.5	0.52	1.7	0.60	2.2
0.25	1.7	0.72	1.4	0.78	1.6	1.00	2.2
0.37	1.7	0.94	1.4	1.20	1.4	1.30	2.1
0.42	1.6	1.25	1.3				
0.60	1.5						
0.75	1.4						
0.90	1.4						
0.97	1.4						
1.56	1.2						

Spectral anisotropy

Fig. 4.20 shows the time dependence of the spectral anisotropy of the 0.5 M solution for different values of pressure.

Fig. 4.20 Spectral anisotropy decay of the 0.5M solution for different pressures: room pressure (black circles), 0.1 GPa (red circles), 0.2 GPa (green circles), 0.5 GPa (blue circles) and 1.2 GPa (cyan circles); the dotted coloured lines are guidelines for the eyes. All data are extracted from the negative band of the transient spectrum at 2500 cm^{-1}.

The rotational time constants extracted from the fit are collected (red dots) in **Fig. 4.22**, together with those already published for neat water (blue dots). The similarity between the two sets of data is striking: in both cases, a steep drop of the rotational time takes place in the pressure range below 0.2 GPa, followed by a plateau where the time constant is almost pressure independent. The only difference is that the plateau sets around 1.3 ps for neat water and at ~ 1.7 ps for the 0.5 M ionic solution.
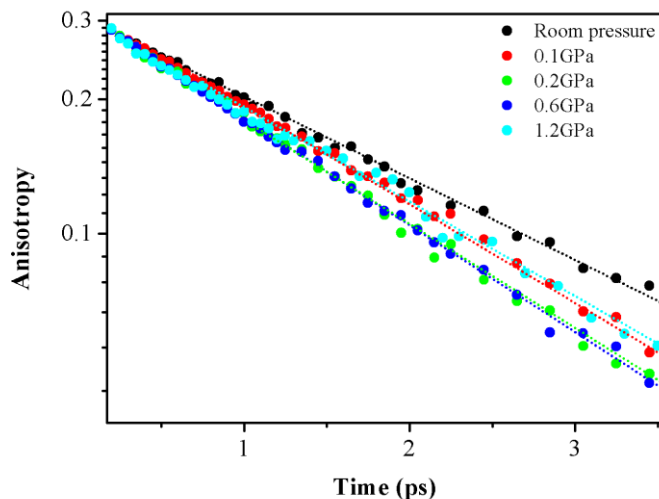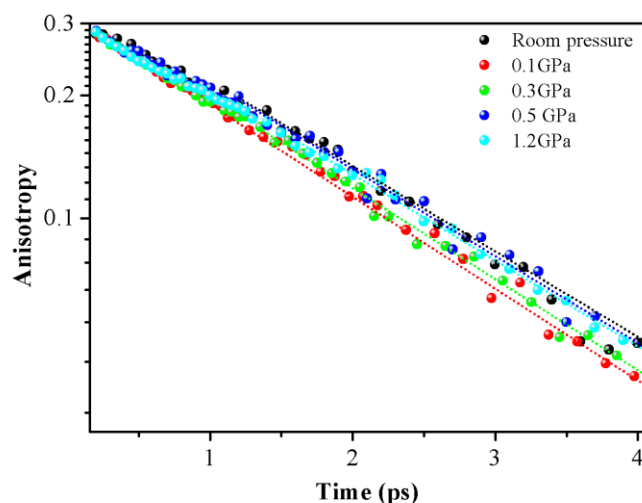
Fig. 4.21 Spectral anisotropy decay for 2 M solution as a function of pressure: room pressure (black circles), 0.1 GPa (red circles), 0.3 GPa (green circles), 0.3 GPa (blue circles) and 1.2 GPa (cyan circles).
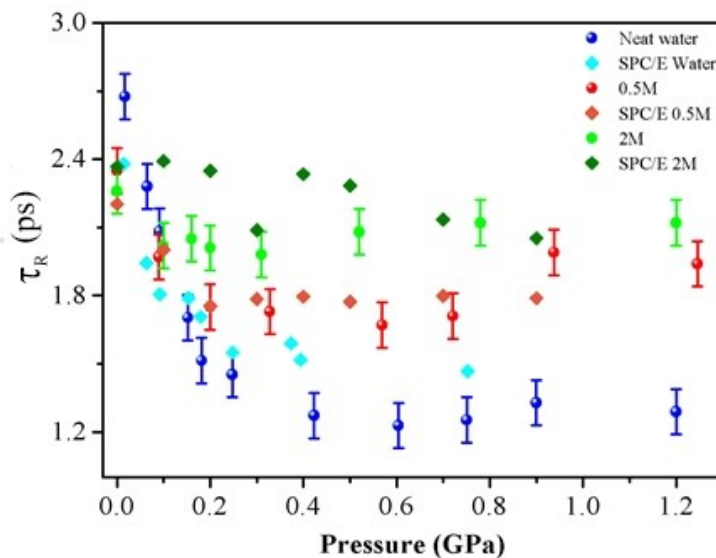

Fig. 4.22 Rotational time constant as a function of pressure. Blue circles: experimental data for neat water. Red circles: experimental data for 0.5 M solution. Green circles: experimental data for 2 M solution. Cyan diamonds: calculated for neat water. Red diamonds: calculated for 0.5 M solution. Green diamonds: calculated for 2 M solution.

Interestingly, the spectral anisotropy curves, measured for the 2M solution and collected in **Fig. 4.21**, show practically no pressure dependence. The rotational time constant (see **Fig. 4.22**) varies slightly between 2.1 and 2.3 ps in the entire $0 - 1.2$ GPa pressure range. It is worth noticing that the level of the plateau follows the trend observed on going from neat water to 0.5 M solution (**Fig. 4.22**), with a marked concentration dependence: 1.3 ps in neat water; 1.7 ps in the 0.5 M solution; 2.2 ps at 2 M concentration.

We underline that there is a good agreement of the simulated data with the experimental results. We use in the MD simulations: the SPC/E model [29] for water and the potential proposed by Heinje et al. [30] for $NaClO_4$. All details are described in **Section 4.4**.

In **Fig. 4.22**, we report the trend of the rotational time as a function of pressure rather than density. The reason is that there are no experimental data for the density of the perchlorate solutions at high pressure. In principle, we could use the densities calculated in the MD simulations; we found that is possible for neat water, but the error on the calculated density at room pressure grows critically with the concentration.

Lastly, we show the data relative to orientational dynamics of 6M solution. We choose to analyse the data recorded at 2342 cm⁻¹ of frequency for the Sodium Perchlorate solution 6 M; the reasons are explained before in the section relative to the vibrational relaxation.
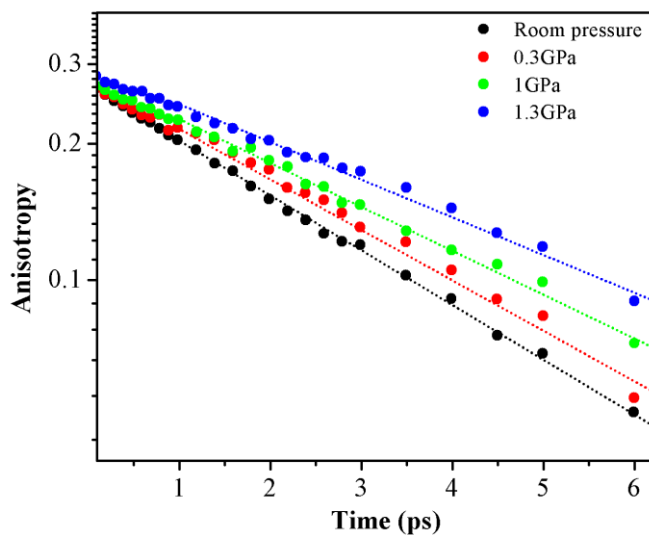
Fig. 4.23 Spectral anisotropy decay for the 6M SP solution as a function of pressure: room pressure (black circles), 0.3 GPa (red circles), 1 GPa (green circles) and 1.3 GPa (blue circles). The data are acquired on the positive band at 2342 cm⁻¹.

In **Fig. 4.23**, we show that increasing pressure causes a gradual slowing down of the orientational dynamics for the W_w molecules in the 6M solution. For this sample we have been able, thanks to the lengthening of the OD stretch lifetime at high concentration, of measuring the spectral anisotropy up to a delay time of 6 ps.

In **Fig. 4.24** we report the rotational time constant at different pressures.
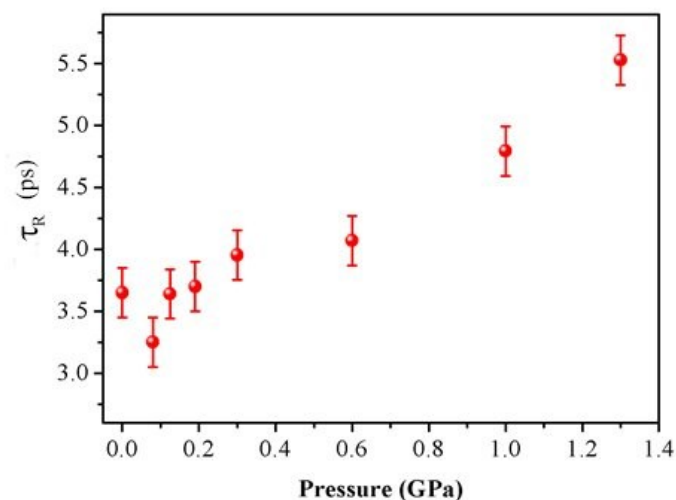
Fig. 4.24 Reorientation time τ_R versus pressure for the 6 M solution.

For this high concentrated solution, the reorientation time grows markedly with the increase of pressure. **Table 4.7** summarizes the reorientation times measured for all systems as a function of pressure.

Table 4.7   Reorientation time τ_R for neat water and 0.5, 2 and 6 M solutions at different applied pressures

Water		0.5M		2M		6M	
Pressure (GPa)	τ_R (ps)	Pressure (GPa)	τ_R (ps)	Pressure (GPa)	τ_R (ps)	Pressure (GPa)	τ_R (ps)
0.02	2.7	0.0001	2.3	0.0001	2.3	0.0001	3.6
0.06	2.3	0.09	2.0	0.10	2.0	0.08	3.2
0.09	2.1	0.20	1.7	0.16	2.0	0.12	3.6
0.15	1.7	0.33	1.7	0.20	2.0	0.19	3.7
0.18	1.5	0.57	1.7	0.31	2.0	0.30	3.9
0.25	1.4	0.72	1.7	0.52	2.1	0.6	4.1
0.42	1.3	0.94	2.0	0.78	2.1	1.0	4.8
0.60	1.2	1.25	1.9	1.2	2.1	1.3	5.5
0.75	1.2						
0.90	1.3						
1.2	1.3						

4.3 2D-IR experiment

2D-IR experiments in the region of the OD stretching mode were performed on 2 and 6 M NaClO$_4$ solutions at room pressure. **Fig. 4.25** shows a typical interferometric signal of the 2M SP solution, acquired scanning the sledge positions of the Mach-Zehnder interferometer.
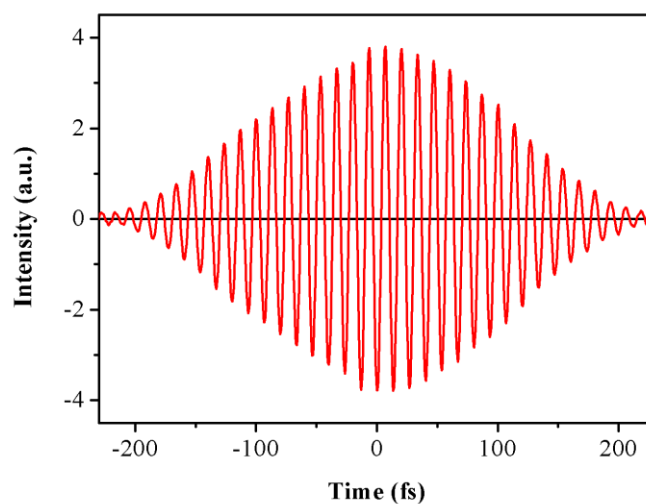

Fig. 4.25 Transient signal acquired, for the 2M NaClO$_4$ solution, scanning the delay time between the pump pulses.

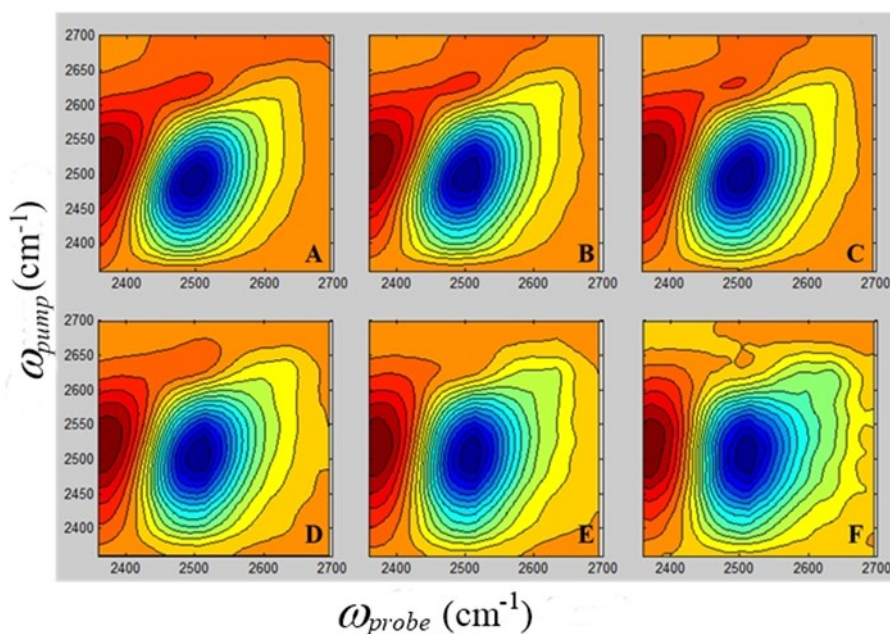The 2D maps obtained for the 2M solution are shown in **Fig. 4.26**.

Fig. 4.26 Two-dimensional spectra of a 2 M solution, measured at different pump- probe delay times: **A)** 0.05ps, **B)** 0.15 ps, **C)** 0.30ps, **D)** 0.55ps, **E)** 1.35ps and **F)** 2.35ps.

At very short pump-probe delay time (population time) the diagonal peaks (d.p.) are elongated in the direction of the diagonal, due to inhomogeneous effects. As the delay increases, the diagonal peaks change their shape from diagonally elongated to circular. This is a consequence of the spectral diffusion, by which the spectral signature of inhomogeneity is wiped out by fast structural fluctuations of the liquid.

4.4 Molecular Dynamics Simulations

Dr. Marco Pagliai has performed all the simulations reported in this thesis work. He realized MD simulations in the NVE ensemble with the SPC/E model, which was shown to be helpful in the description of ultrafast vibrational spectroscopy experiments [31]. For the simulations of $NaClO_4$ aqueous solutions we used the ORAC program [32, 33, 34]: we use SPC/E model [29] for water, while for $NaClO_4$ we adopt the potential parameters proposed by Heinje et al. [30]. These set of parameters are known to work well for dilute solutions: we verified that the potential reproduces almost exactly the experimental density of the 0.5M solution; for the 2 M we found an acceptable negative deviation of 5%. The error on the density of the 6 M solution exceeds 10%, and is considered unacceptable. For this reason, we limited our simulation to 0.5 and 2 M concentrations.

The systems was thermalized at 300 K for 120 ps and the trajectories collected for 240 ps in the NVE ensemble. The dimension of the cubic simulation boxes at the different pressure values has been obtained performing molecular dynamics simulations for 1.2 ns in the NPT ensemble.

In **Table 4.8** we report the number of molecules used to perform the simulations for the different systems and the dimension of the simulation boxes.

Tab. 4.8 Parameters used to perform the simulations on the different $NaClO_4$ solutions.

Concentration (M)	number of $NaClO_4$	number of H_2O	number of HOD	side length (Å)
0.5	8	816	48	29.8038
1.0	16	784	48	29.7530
1.5	24	784	48	29.8944
2.0	32	752	48	29.7822
3.0	48	720	48	29.8754
4.0	64	680	40	29.8262
6.0	96	584	40	29.7586

5. Optical Kerr Effect (OKE) results

5.1 Introduction

Time-resolved optical Kerr effect (OKE) investigations of liquid water show the signature of fast vibrational dynamics at short times, followed by a slower monotonic relaxation. The initial oscillatory component provides information about intermolecular hydrogen bond dynamics, and can be directly compared with the low-frequency Raman spectrum. In fact, the OKE experiments on supercooled water have been focused so far on the investigation of the slower decay, which is interpreted as a structural relaxation phenomenon.

An important aspect to be considered in interpreting OKE and depolarized light-scattering experiments on liquid water is the microscopic origin of the measured signal. The molecular polarizability of water is almost isotropic and the optically induced polarization is therefore dominated by intermolecular (collision induced) contributions. This holds not only for the high- frequency (>10 cm^{-1}) part of the light-scattering spectrum (corresponding to the short time OKE signal), but also for the very-low-frequency part that corresponds to the long-time relaxation tail of our time domain data. In other words, the OKE and depolarized-light scattering techniques are mostly sensitive to the intermolecular dynamics of water. In the short delay time limit, this corresponds to the intra-cage vibrational dynamics; the long-time decay, in contrast, is prevalently associated with rearrangement of local (cage) structures, which represents the first step of the overall structural relaxation. More precisely, the measured signal in a OKE experiment is defined by the material response function, that is, by the time-derivative of the dielectric-constant correlation function which, in water, is dominated by the intermolecular contribution.

The time resolved OKE signal for neat water, shown in **Fig. 5.1**, is dominated by the purely electronic contribution (the strong peak at zero delay time). In fact, the almost isotropic molecular polarizability makes the molecular contribution to the anisotropic susceptibility (**Eqs. 3.12** and **3.13**) of the sample very small, so that the intermolecular term (**Eq. 3.13**) contribute largely to the nuclear OKE response of water.
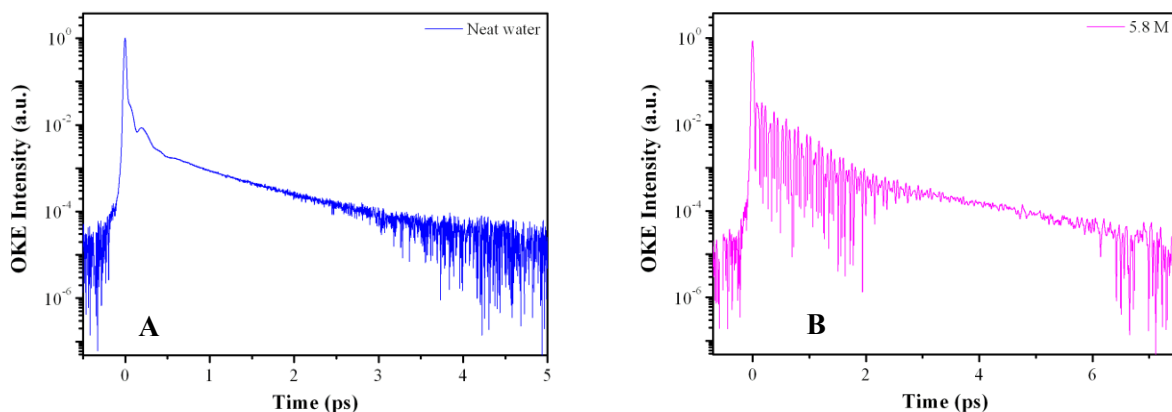
Fig. 5.1 A) The signal measu red in a HD-OKE experiment for neat water solution
B) the same, for the NaClO$_4$ solution 5.8M.

The large and fast oscillations showing up at short times (< 3 ps) in **Fig. 5.1B** are due to the intramolecular vibrations of the ClO$_4^-$ anion. The much slower and weaker oscillations that are visible in the first piscosecond of the neat water decay (**Fig. 5.1A**) are due to low frequency intermolecular vibrations; similar low frequency oscillations are observed also in the OKE experiments on the perchlorate solutions, although partially hidden by the intramolecular oscillations.

The very large relative intensity of the electronic peak makes the accurate knowledge of the instrumental function a crucial step towards a reliable signal deconvolution. Actually, it has been shown that, in case of weak nuclear response, even small deviations from the "correct" instrumental function produce relevant baseline modulations in the frequency domain Fourier transformed spectra, thus preventing reliable and consistent spectral profiles.

In view of its decisive importance for the correct analysis of the experimental data, it is worthwhile to describe in some detail the procedure adopted to extract the instrumental function $G(t)$ that appears in **Eqs. 3.26** and **3.31**.
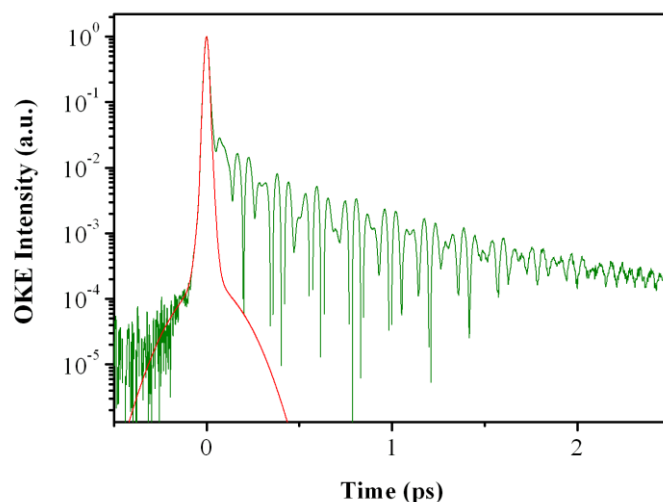
Fig. 5.2 Signal decay of 2M solution (green) and the instrumental function (red) used for the deconvolution.

We chose a plate of calcium fluoride, a cubic ionic crystal whose OKE response consists only of the instantaneous electronic peak and of one underdamped DHO corresponding to the Raman-active band at 322 cm^{-1} (T$_{2g}$ symmetry). In order to ensure that the instrumental function is taken exactly in the same experimental conditions as the OKE signal of the sample, care is taken to minimize the cell displacement when moving the illuminated spot from the CaF$_2$ plate to the bulk liquid (or the other way round). For this reason, the calcium fluoride plate is dipped directly inside the sample cell, so that just a very short horizontal translation of the cell is required, leaving the rest of the set-up unchanged. We make sure that the entrance face of the CaF$_2$ plate sticks to the inside of the front window of the cell; we acquire the instrumental function for each data set [25]. **Fig. 5.2** compares the measured instrumental function and the signal measured for a 2 M perchlorate solution. Notice that the response of the CaF$_2$ plate is free of any disturbing contribution (other than the purely electronic response) for at least four orders of magnitude. In this entire dynamic range, at negative times the rise of the signal from the reference and from the sample coincide exactly.

We assume that the time profile of the OKE signal can be reproduced as the sum of a stretched exponential relaxation and of a number of damped harmonic oscillators (DHOs) representing the oscillating components.

The stretched exponential $e^{-(t/\tau)^\beta}$, with the stretching parameter $\beta < 1$, is known to describe the structural relaxation of neat water. The general expression for the solution of the damped harmonic oscillator has the form $x(t) = e^{-\frac{\gamma}{2}}(A_1 e^{i\zeta t} + A_2 e^{-i\zeta t})$.

From **Eq. 3.10** we know that the time dependence of the OKE signal is the first time derivative of the susceptibility response function: the function used in our fitting is then

$$f(t) \propto \frac{\partial}{\partial t}\left[Ae^{\left(-\frac{t}{\tau_{struct}}\right)^\beta} + \sum_i e^{-i\frac{\gamma_i}{2}t}(A_1 e^{i\zeta_i t} + A_2 e^{-i\zeta_i t}) \right] \tag{5.2}$$

where $\zeta_i = \sqrt{\omega_i^2 - \gamma_i^2/4}$.

In the underdamped limit, i.e., for $\gamma_i \ll 2\omega_i$, the summation in the square brackets becomes the sum of simple damped cosine functions. In the overdamped limit, with $\gamma_i \gg 2\omega_i$, **Eq. 5.2** is

$$f(t) \propto \frac{\partial}{\partial t}\left[Ae^{\left(-\frac{t}{\tau_{struct}}\right)^\beta} + \sum_i e^{-\frac{\gamma}{2}t}(A_1 e^{-|\zeta_i|t} + A_2 e^{-|\zeta_i|t}) \right] \tag{5.3}$$

Although the oscillatory components of the OKE signal are better discussed in the frequency domain, it has to be stressed that all the simulated spectra that will be considered in the following sections are obtained from fitting performed in the time domain, using the general function given in **Eq. 5.2**.

Fig. 5.3 gives an example of the fit obtained for the HD-OKE signal of a NaClO$_4$ 2 M solution.
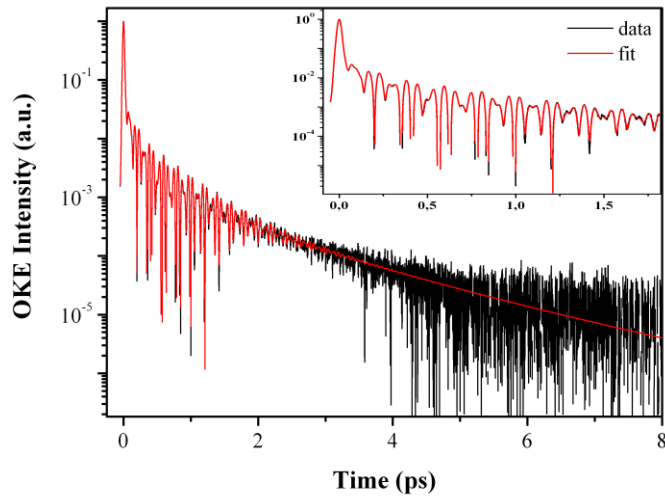
Fig. 5.3 Experimental (black) and simulated (red) time evolution of the HD-OKE signal for NaClO$_4$ 2M aqueous solution. The simulation is the sum one stretched exponential, six lorentzian (intramolecular) oscillators, convoluted with the instrumental function.

5.2 Concentration effect

Fig. 5.4 reports the time profile of the HD-OKE signal measured for 2 M and 5.8 M NaClO$_4$ solutions.
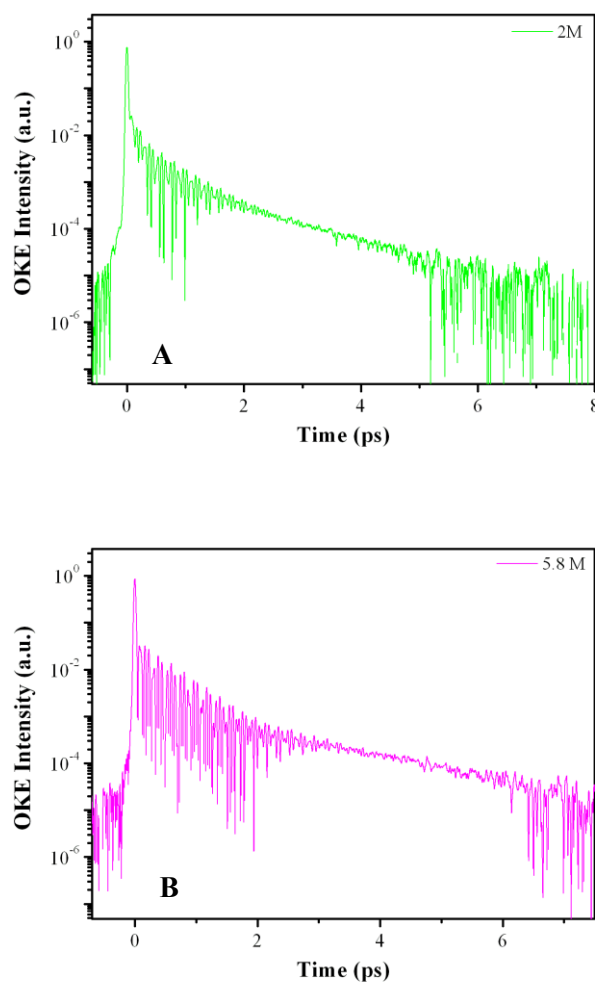
Fig. 5.4 A) Signal measured in a HD-OKE experiment for NaClO$_4$ aqueous solution 2M.
B) the same, for a 5.8M solution.

Comparing **Fig. 5.4** and **Fig. 5.1A,** it appears that the long delay time decay gets slower with increasing salt concentration and, in parallel, the intensity of the nuclear signal grows.

Structural relaxation

A stretched exponential decay for the structural relaxation is typical of condensed systems characterized by dynamics that take place on a broad distribution of timescales, which are correlated to the presence of a variety of relaxing structures.

In the fitting procedure we make use of **Eq. 5.2**, keeping the value of β fixed at 0.7 (the value usually adopted for water).

It is evident that the value of T_{struct} that we obtain depends on the value of the stretching parameter β. It is common practice to use instead the mean structural relaxation time $\langle \tau \rangle$, defined mathematically as the area under the normalized stretched exponential curve; it can be reduced to the form:

$$\langle \tau \rangle = \frac{T_{struct}}{\beta} \cdot \Gamma(1/\beta) \tag{5.4}$$

where $\Gamma(x)$ is the gamma function. The concentration dependence of the mean structural relaxation time is given in **Fig. 5.5**.
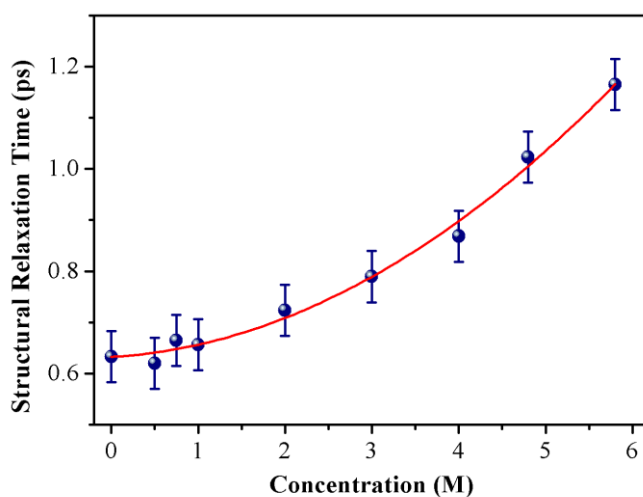
Fig. 5.5 Dependence of the structural mean relaxation time as a function of the $NaClO_4$ concentration. The red line is a second order polynomial fit.

The structural relaxation time increases with the salt concentration; the trend can be reproduced very closely with a second order polynomial function.

Table 5.1 Structural relaxation time of different NaClO$_4$ at different concentrations.

Concentration (M)	T$_{struct}$ (ps)
0	0.63
0.50	0.62
0.75	0.67
1	0.66
2	0.72
3	0.79
4	0.87
4.80	1.02
5.80	1.16

Oscillatory components and spectral response

The oscillatory components of the OKE signal are better discussed in the frequency domain. As reported in **Section 3.1.3**, the spectral representation of the time resolved OKE signal is obtained as the imaginary part of the Fourier transform of the time domain response function. It corresponds to the depolarized Raman spectral density, as defined in **eq. 3.32**. The spectral densities for NaClO$_4$ solutions of different concentration are collected in **Fig. 5.7**.

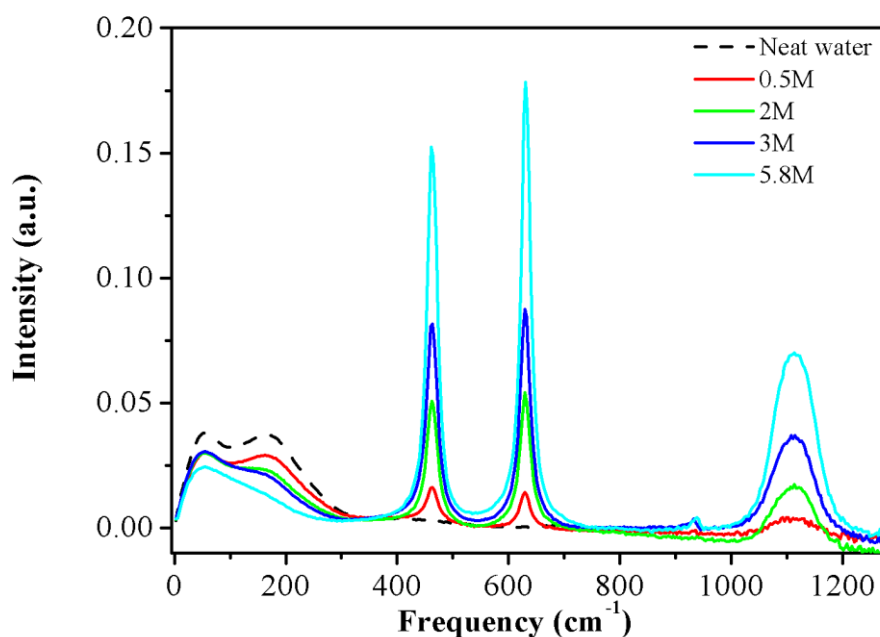**Fig. 5.7** Frequency response of NaClO₄ aqueous solutions at different concentration obtained from the OKE data using the instrumental function extracted by the fluorite measure. In the graph, we insert even the neat water spectrum (black dotted line) for a comparison.

We notice five main peaks; the two peaks below 300 cm^{-1} (which merge in a single asymmetric broad band at high concentration) are due to intermolecular vibrations; the higher frequency peaks are ascribed to ClO_4^- internal modes. The two broad bands at about 50 cm^{-1} and 200 cm^{-1} are generally indicated in the literature [25] as "bending" and "stretching" of the hydrogen-bond network. The two bands centered at about 460 cm^{-1} and 626 cm^{-1} are assigned to the anion symmetric and antisymmetric O-Cl-O bending, respectively, and the 1110 cm^{-1} band corresponds to the antisymmetric Cl-O stretching [35]. The very weak peak around 932 cm^{-1} corresponds to the symmetric stretching of the anion; its extremely low intensity is due to the total symmetric nature of the vibrational mode.

For the analysis of the spectra at different concentrations, we used the intramolecular band at 626 cm^{-1} as an intensity reference, rescaling all the spectra to make the intensity of this band proportional to the ClO_4^- concentration.

In **Fig. 5.8** we collect the spectra in the region of the intermolecular vibrations for solutions of different concentrations, after subtraction of the very low frequency (10 cm^{-1}) band, corresponding to the structural relaxation.
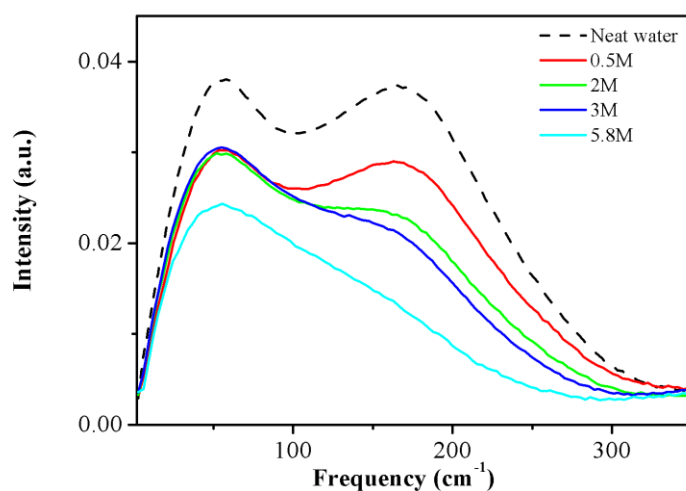
Fig. 5.8 Zoom of the NaClO$_4$ spectra in the intermolecular frequency region.

Salt concentration has a relevant influence on the relative intensities of the two peaks. Definitely, the intensity of the peak around 60 cm^{-1} compared to that at ~ 200 cm^{-1}, grows with concentration. However, there are large fluctuations in the trend of the absolute intensities with rising concentration. We attribute this partially erratic behaviour to the relevant background fluctuations produced by the imperfect instrumental functions used in the deconvolution. Therefore, we need another quantity, independent of the baseline, to characterize the spectral variations.

We found that a more stable parameter, much less dependent on the baseline fluctuations, is the ratio of the areas of the two peaks, obtained by fitting the spectrum with the sum of two DHOs.

Fig. 5.9 shows the spectrum in the low frequency region and the spectral result of the fit performed on the OKE data for the 0.5 M solution.
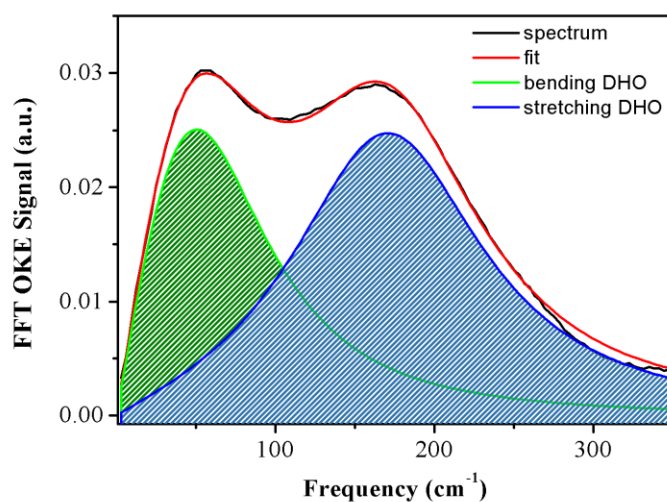
Fig. 5.9 Fourier transforms of signal (black line) and fit with two damped harmonic oscillators (DHO) as from eq. 5.2 (red line), for the NaClO4 0.5 M solution. The areas of the two spectral components are shown in green and blue colours.

The ratio of the areas of the peaks at ~60 cm^{-1} and ~200 cm^{-1} is given as a function of concentration in **Fig. 5.10**.
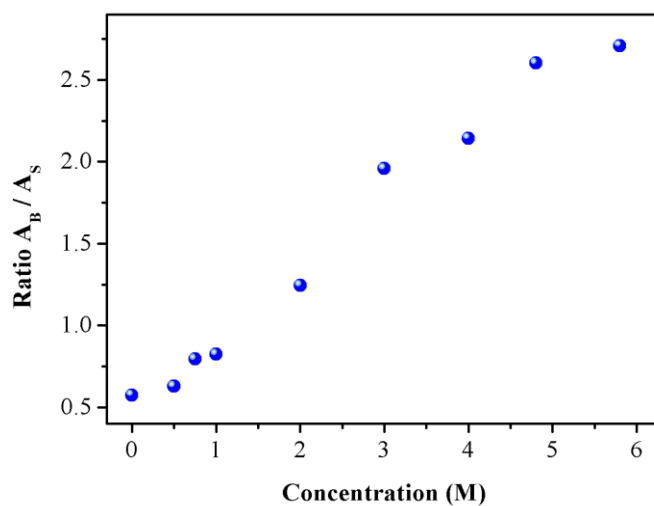
Fig. 5.10 Ratio of the areas of the two low frequency bands in **Fig. 5.9**, as a function of the molar concentration.

The ratio of area of the peak at ~60 cm^{-1} to that of the ~200 cm^{-1} band (see **Fig. 5.9**) grows almost linearly with the salt concentration.

The area ratio of these two bands grows monotonically with the rise of concentration.

Below, we report in table the frequency and the linewidth of the oscillators used to simulate the intermolecular peaks.

Table 5.2 The frequency (ω) and the linewidth (γ) of the DHOs for different salt concentration.

| Concentration (M)	ω_1 (cm^{-1})	γ_1 (cm^{-1})	ω_2 (cm^{-1})	γ_2 (cm^{-1})
0	73.9	122.8	186.8	145.9
0.5	75.3	127.7	185.4	148.0
0.75	78.2	139.0	184.0	140.9
1	78.8	141.1	183.8	143.3
2	84.4	163.0	180.6	135.7
3	88.2	173.8	173.7	118.9
4	89.6	179.5	171.8	125.2
4.8	89.6	177.6	165.7	123.2
5.8	85.7	168.0	155.4	121.0

5.3 Pressure effect

We performed experiments in the pressure range (0.1-1.3) GPa on NaClO$_4$ aqueous solutions at concentration 0.5, 2 and 6 M, using a Diamond Anvil Cell (DAC). The cell is similar to the one described in **Section 2.4.5**; with the only difference that diamonds replaces the sapphire windows. In fact, sapphire cannot be used of because of the high birefringence of this material (diamond has a cubic crystal structure and is optically isotropic).

There are several difficulties in realizing ultrafast OKE experiments in a DAC. One is due to the stress induced in the windows by the pressure: it leads to some degree of depolarization of the beams used in the experiment, a very detrimental drawback in a polarization-based technique. The detection procedure used in our experiments, based on the simultaneous acquisitions of heterodyned signals with opposite phases, reduces to a well acceptable level the disturbance from this effect. A second obstacle is the chirping of the short pulses due to the linear and nonlinear dispersion in the thick windows. This inconvenience is

substantially attenuated by pre-compensating with a negative chirp the pulses used in the experiment. It results that the most serious hindrance consists in the difficulty of obtaining a good instrumental function. Experimentally, the obvious choice is that of using the diamond as reference material to extract this information. However, in order to measure the OKE signal of the window, the cell has to be moved (back or forth) in the direction of propagation of the beams, so that the focused beams meet inside the window. Consequently, the chirping that affects the pulses changes: their compression has to be re-optimized. However, it is practically impossible, whatever the adjustment of the prism compressor geometry, to recover exactly the initial compression of the pulse: the resulting instrumental function is invariably inappropriate. Several unsatisfactory tests done employing different instrumental functions obtained with this procedure, convinced us to abandon the method.

We then decided to adopt a completely different approach. The best results, although not completely satisfactory, are obtained by building an "artificial" instrumental function, obtained by fitting the rise, at negative times, of the electronic peak of the $NaClO_4$ solution OKE signal with a combination of peak functions (Gaussian, Lorentzian). The instrumental function is then completed by folding the rising part around t =0.

Fig. 5.11 gives an example of the instrumental function obtained with this method from the fit of the purely electronic peak of a 2 M solution.
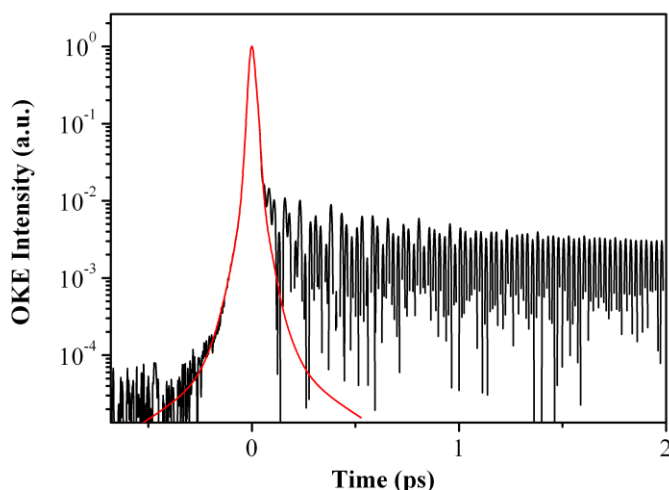

Fig. 5.11 Signal decay of the 6M solution (black) and the instrumental function (red) obtained from the fit of the electronic peak using Gaussians and Lorentzian functions.

If we compare **Fig. 5.11** with **Fig. 5.2**, it is evident that in both cases the electronic peak is very well reproduced for at least four decades. It is equally clear that in **Fig. 5.11**, below

10^{-4} intensity, the simulated instrumental function has a different shape by the other instrumental function. In spite of its exiguity, this discrepancy is detrimental to a completely reliable deconvolution of the frequency domain OKE data. It has to be stressed that this extreme sensitivity to the quality of the instrumental function is peculiar of water, and is a consequence of the extremely low intensity of the nuclear contribution to the OKE signal.

Structural relaxation

Also for the high pressure data, we use the same fitting function (**Eq. 5.2**) adopted for the room pressure data, maintaining for the stretching parameter β the value 0.7.

Fig. 5.12 reports the pressure dependence of the mean relaxation time for neat water and 0.5, 2 and 6 M $NaClO_4$ solutions.
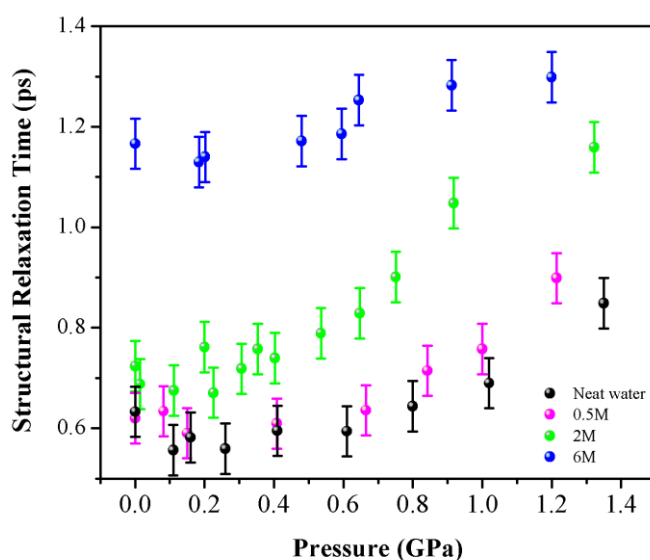
Fig. 5.12 Trend of the structural mean relaxation in function of pressure for different systems: neat water (black circles), 0.5M (magenta circles), 2M (green circles) and 6M (blue circles). The red lines correspond to the second order polynomial fit of the data.

For neat water and $NaClO_4$ 0.5 M solution two different regimes are visible in the figure. Up to 0.2 Gpa, the structural relaxation time shows a slight decrease with increasing pressure. In contrast, the relaxation time increases appreciably at higher pressures.

In more concentrated solutions, we observe an essentially monotonic trend throughout the examined pressure range, with a progressive slowing down of the relaxation.

Fig. 5.12 reports the value of the structural relaxation time as a function of pressure rather than density. In fact, no experimental data are available for the density of the perchlorate

solutions at high pressure. In principle, we could use the densities calculated in the MD simulations; however, we found that, while the calculated density at room pressure is in good agreement with the experimental value of neat water, the error grows remarkably with the concentration. In particular, the simulated density shows an error that goes from 1% for the 0.5M solution to 4% for the 2M solution.

Table 5.3 Structural relaxation time obtained for different systems in function of pressure.

Neat Water		0.5 M solution		2M solution		6M solution	
Pressure (GPa)	T_{struct} (ps)	Pressure (GPa)	T_{struct} (ps)	Pressure (GPa)	T_{struct} (ps)	Pressure (GPa)	T_{struct} (ps)
0.0001	0.63	0.0001	0.62	0.0001	0.72	0.0001	1.17
0.11	0.56	0.08	0.63	0.01	0.69	0.18	1.13
0.16	0.58	0.15	0.59	0.01	0.67	0.20	1.14
0.26	0.56	0.41	0.61	0.02	0.67	0.48	1.17
0.41	0.59	0.66	0.64	0.03	0.72	0.59	1.19
0.61	0.59	0.84	0.71	0.04	0.76	0.64	1.25
0.8	0.64	1.0	0.76	0.05	0.79	0.91	1.28
1.02	0.69	1.21	0.90	0.20	0.76	1.20	1.3
1.35	0.85			0.43	0.74		
				0.65	0.83		
				0.75	0.90		
				0.92	1.05		
				1.32	1.16		

Oscillatory components and spectral response

In **Fig.5.13** we report the spectra of $NaClO_4$ solutions 0.5, 2 and 6M for different pressures. We suppose that intramolecular peaks are not influenced by the compression phase and so, we impose that the peak area at frequency equal to 626 cm^{-1} is constant for the same solution. Moreover, the low frequency peak, corresponding to the structural relaxation, and a broad peak at about 450 cm^{-1} are subtracted from the spectra. Again, we focus our attention on the intermolecular peaks, at lower frequencies, relatives to HBs network.
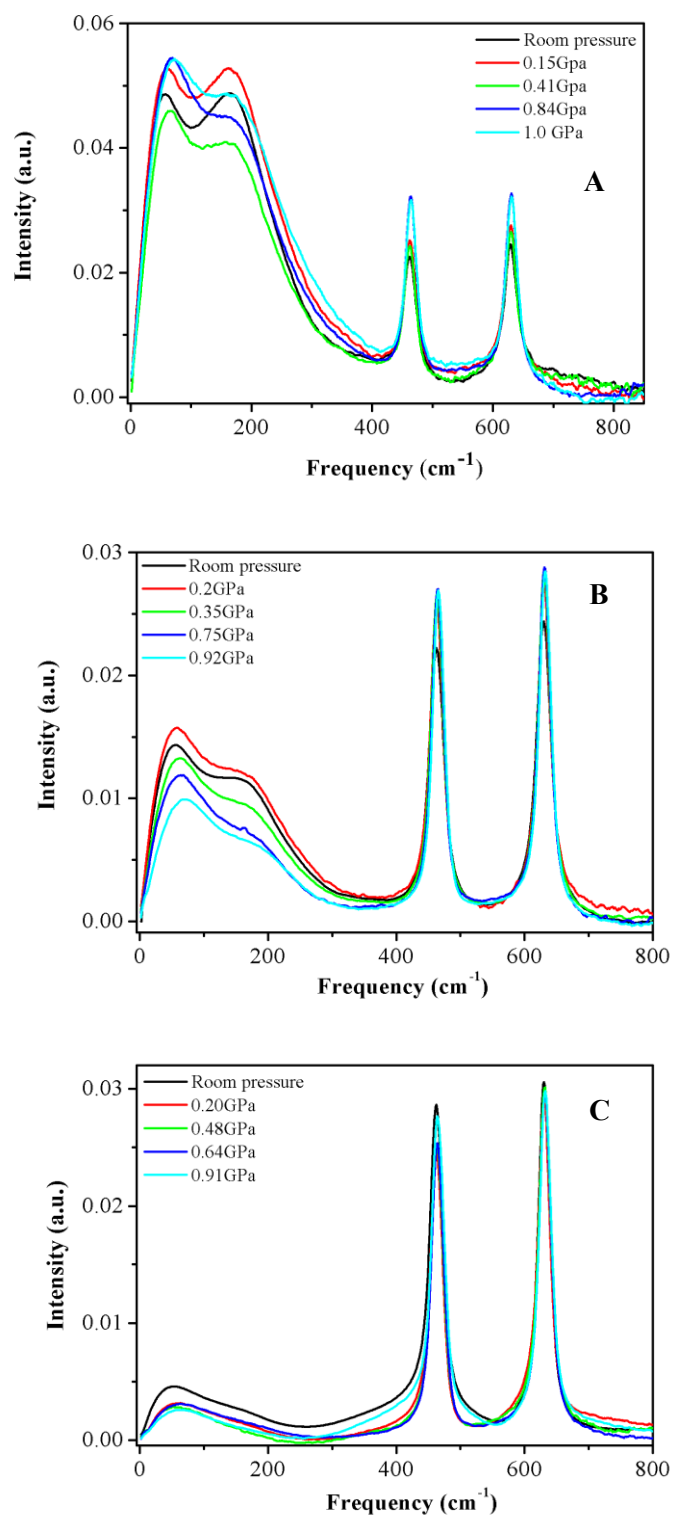
Fig. 5.13 Raman spectral density at different applied pressures. **A)** 0.5M NaClO$_4$ solution; **B)** 2M solution; **C)** 6M solution.

The spectra in **Fig. 5.13** show that the relative intensity of the low frequency peak (~60 cm^{-1}) grows with increasing pressure.

As indicated in **Section 5.2**, we use the ratio of the intensities of the two low frequency DHOs that reproduce the bending and stretching peaks to characterize the spectral variations. In **Fig. 5.10** we saw that that ratio increases pretty much with concentration. The behavior is similar also for the pressure dependence: the data collected in **Fig. 5.14** correspond to the area of the band at ~60 cm^{-1} divided by that at ~200 cm^{-1} (see **Fig. 5.9**).
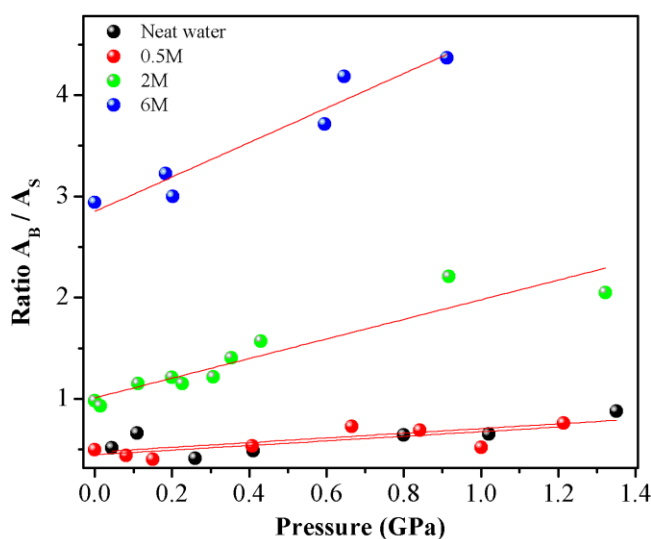
Fig. 5.14 Area of the band at ~60 cm^{-1}divided by that at ~200 cm^{-1}, as a function of the pressure for solutions of different concentration: neat water (black), 0.5M (red), 2M (green) and 6M (blue). Lines are linear fit of data.

At all concentrations, the intensity ratio of the two bands grows linearly with the pressure, with slopes that increase with the salt concentration.

In **Table 5.4** we summarize the parameters used to fit the HB stretching and bending bands for different concentrations and pressures.

Table 5.4 A) Frequency and linewidth of the DHOs used to simulate the lower frequency peaks for the 0.5M in function of pressure. **B)** the same, for the 2M solution. **C)** the same, for the 6M solution.

A)

Pressure (GPa)	ω_1 (cm^{-1})	γ_1 (cm^{-1})	ω_2 (cm^{-1})	γ_2 (cm^{-1})
0.0001	73.1	120.9	189.2	166.2
0.08	71.2	112.8	190.1	173.3
0.15	71.8	112.7	194.6	192.6
0.41	77.5	115.7	193.8	182.2
0.66	81.9	127.3	195.1	175.3
0.84	85.2	135.6	202.1	191.8
1.00	86.4	137.3	210.3	218.8
1.21	91.7	146.0	207.0	189.4

B)

Pressure (GPa)	ω_1 (cm^{-1})	γ_1 (cm^{-1})	ω_2 (cm^{-1})	γ_2 (cm^{-1})
0.0001	80.4	150.2	183.2	151.4
0.01	80.8	151.4	186.4	159.4
0.11	83.6	154.8	185.6	148.6
0.20	80.7	146.1	181.7	144.6
0.23	87.9	172.8	189.3	155.9
0.31	86.9	158.6	190.2	158.0
0.35	87.4	158.5	190.6	156.3
0.43	88.8	158.5	188.9	147.8
0.92	96.2	178.0	188.3	115.1
1.32	99.0	166.6	197.4	134.5

C)

Pressure 6M (GPa)	ω_1 (cm^{-1})	γ_1 (cm^{-1})	ω_2 (cm^{-1})	γ_2 (cm^{-1})
0.0001	80.5	149.2	152.8	104.0
0.18	83.9	148.4	150.1	109.2
0.20	74.2	107.0	133.4	78.4
0.59	74.9	111.6	132.2	79.1
0.64	90.4	146.7	161.9	100.4
0.91	80.6	120.0	139.7	85.7

6. Discussion

That the dynamics of water is heavily affected by the addition of ionic solutes has been proven by several experimental studies [36, 37, 38]. Still some ambiguities remain on the reasons why the effect is not univocal, retardation and acceleration having been observed for different solutions. In addition, the effect of concentration is not yet completely clear. In other words, it is still to be understood what is the range of influence of an ion on the surrounding water molecules: is it limited to the first solvation shell, or cooperative effects can change the water properties on a longer range? While concentration and temperature have been employed as variable external parameters in most of those studies, very little is known about the effect of pressure. The results reported in this thesis are intended to give a contribution in this direction.

Linear FT-IR spectra of $NaClO_4$ aqueous solutions are not very informative about that: as shown in **Fig. 4.6**, we observe a down-shift of the peak frequency of the W_w band that can be easily interpreted as due to the strengthening of the hydrogen bond with increasing density of the liquid. In contrast, the frequency of the W_p peak is practically unchanged in the entire pressure range. The data of **Fig. 4.7** demonstrate that this effect is common to all concentrations, from neat water to 4.9 M solution. The frequency of the W_w band (**Fig. 4.6**) increases from 2510 cm^{-1} in neat water to 2527 cm^{-1} in 4.9 M solution; the MD simulation reported in ref. [26] shows that the shift is mostly due to the electrostatic field (Stark effect) generated by the ions.

Transient Infrared spectroscopy is definitely much more informative. Two relevant quantities, the OD stretching vibrational lifetime and the orientational relaxation time, and their pressure and concentration dependence, are derived from the experiments. According to **Fig. 4.12**, the lifetime of the OD vibration is constant in solutions up to 1 M in concentration; beyond that value, the lifetime increases. This effect is attributed to the weakening of the hydrogen bond that reduces the anharmonic coupling to other vibrational degrees of freedom trough the H-bond. Less coupling corresponds to less relaxation channels and, consequently, to longer lifetime of the OD stretching mode. At low perchlorate concentrations, the bulk water forms an almost infinite 3D network. At higher anion concentrations, as more and more hydrogen bonds are broken, the integrity of the network deteriorates. This quasi-infinite

character of the network is definitely lost when the system overcomes the percolation threshold. According to Stanley and Teixeira [39], the percolation threshold for water occurs at a mole fraction of bonded H_2O molecules equal to 0.39. Bondarenko et al. [40] found that in $NaClO_4$ the percolation limit is reached at about 0.035 perchlorate/water mole fraction (see **Fig. 6.1**), corresponding to the concentration of ~1.7 M. Our results are consistent with their result and support the localization of the threshold separating quasi-bulk water from "real" ionic solution, in the concentration region 1.5 – 2 M.
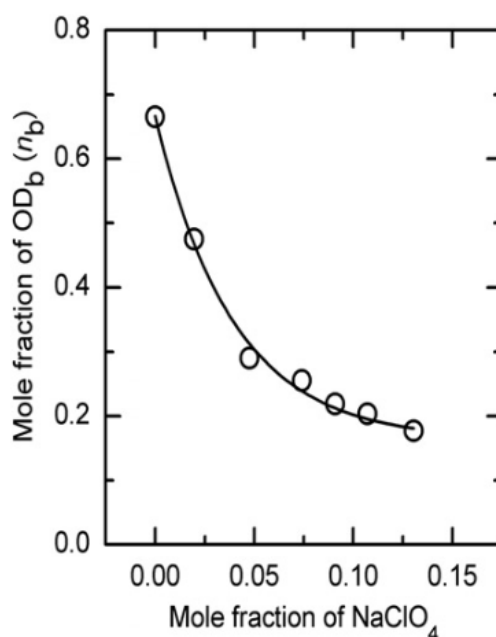

Fig 6.1 Mole fraction (nb) of bonded OD as a function of the perchlorate/water mole fraction. The percolation threshold is placed at nb = 0.39.

As to the rotational time constant obtained from transient anisotropy, the bimodal behavior shown in **Fig. 4.15** was already widely discussed by Stirnemann et al. [26] and well explained with the predictions of the extended jump model. The essence of the model have been already outlined in the **Chapter 1**. A more in-depth look at the model is needed for a correct interpretation of the data.

In $NaClO_4$ solutions, the jump time depends on two opposing term. The weakening of HBs due to the dissolved anions produces a speed up of water reorientation (the jump probability increases if the HB to be broken is weak: the more the anions present, the larger the number of water molecules that can jump). On the other hand, the presence of the ions in solution reduces the number of possible HB acceptors in the neighborhood of water (excluded volume effect), causing a slowdown of the dynamics. For dilute solutions, the weakening of

HBs prevails on the excluded volume effect; therefore, the overall results is the reduction of the orientational time [10] that can be seen in **Fig. 4.15** for concentrations below 1.5 M. At low concentrations ClO_4^- acts as an accelerant of the rotational dynamics. Clearly, this effect is expected to be proportional to the salt concentration.

The sharp change of slope sign between 1.5 and 2 M shown in **Fig. 4.15** tells us that not only the retardation due to the excluded volume prevails beyond that threshold, but that the concentration dependence of the retarding effect is more than proportional to the concentration. The convincing explanation given in ref. [26] relies on the connection that exists between the "frame" contribution τ_{reor}^{frame} to the reorientational time (see **Chapter 1**) and the jump time τ_{reor}^{jump}. As already noticed in the **Chapter 1**, τ_{reor}^{frame} describes a diffusive angular motion and, in the Debye-Stokes-Einstein hydrodynamic picture, is proportional to the viscosity η: $\tau_{reor}^{frame} \propto \eta$.

In turn, also the jump time τ_{reor}^{jump} is related to the viscosity: $\tau_{reor}^{jump} \propto L^2 \eta$. We have then:

$$\tau_{reor}^{frame} = \frac{\tau_{reor}^{jump}}{L^2}$$

(6.1)

where L is the translational displacement induced by an HB jump. While in neat water and in dilute solutions the HB acceptors come from the second shell, in concentrated solutions the presence of a large density of ions induces a partial network disruption that leads to an increasing presence of interstitial HB acceptors between the first and second shells. Thus, the mean displacement L associated to jumps decreases markedly with increasing concentration. At the same time, τ_{reor}^{jump} decreases to a lesser extent. The result is that, at high concentration, the rotational time increases, as shown in **Fig. 4.15,** thanks to the contribution of τ_{reor}^{frame} (**eq. 6.1**). It is worth of notice that our computer simulation reproduces almost perfectly the observed rotational times and their concentration dependence.

An additional proof of this interpretation can be provided by the comparison of orientational time and relative viscosity trends with the concentration.
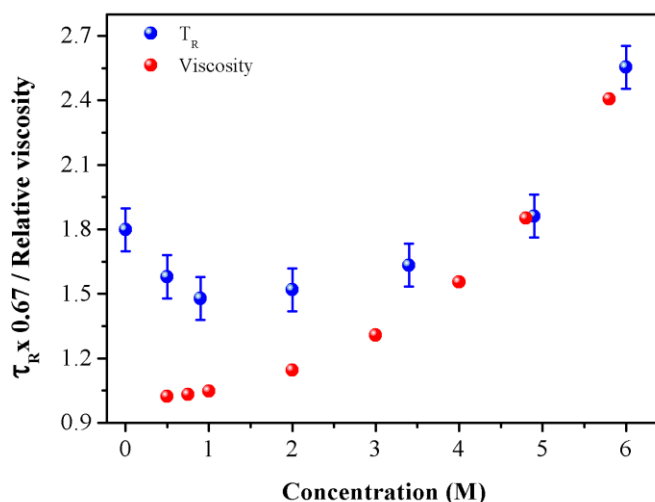
.

Fig. 6.2 Trends of orientational time (blue circle) and the relative viscosity (red circles), expressed as the ratio of solution viscosity and water viscosity, [41] in function of the $NaClO_4$ concentration. We underline that here the reorientation times of **Fig. 4.15** have been multiplied by a constant factor to overlap the last value of the time with the relative viscosity quantity.

We notice that the trend of the orientational time with the concentration recall the viscosity tendency only in the concentrated regime (over 2M). This evidence is in agree with explanation of the concentration effect given by the jump model; indeed, as explained before, the orientational dynamics on the diluted regime is regulated by the jump mechanism. Differently, the dynamics of concentrated system depends mainly by the translational frame term and so by the viscosity.

The radial distribution function $g(r)$ for the water-water $O \cdots O$ distance of **Fig. 6.3** shows that indeed the effect of concentration is that of progressively depressing and canceling the peak of the second solvation shell (~4.5 Å) and, at the same time, of rising a new peak at about 3.2 Å.
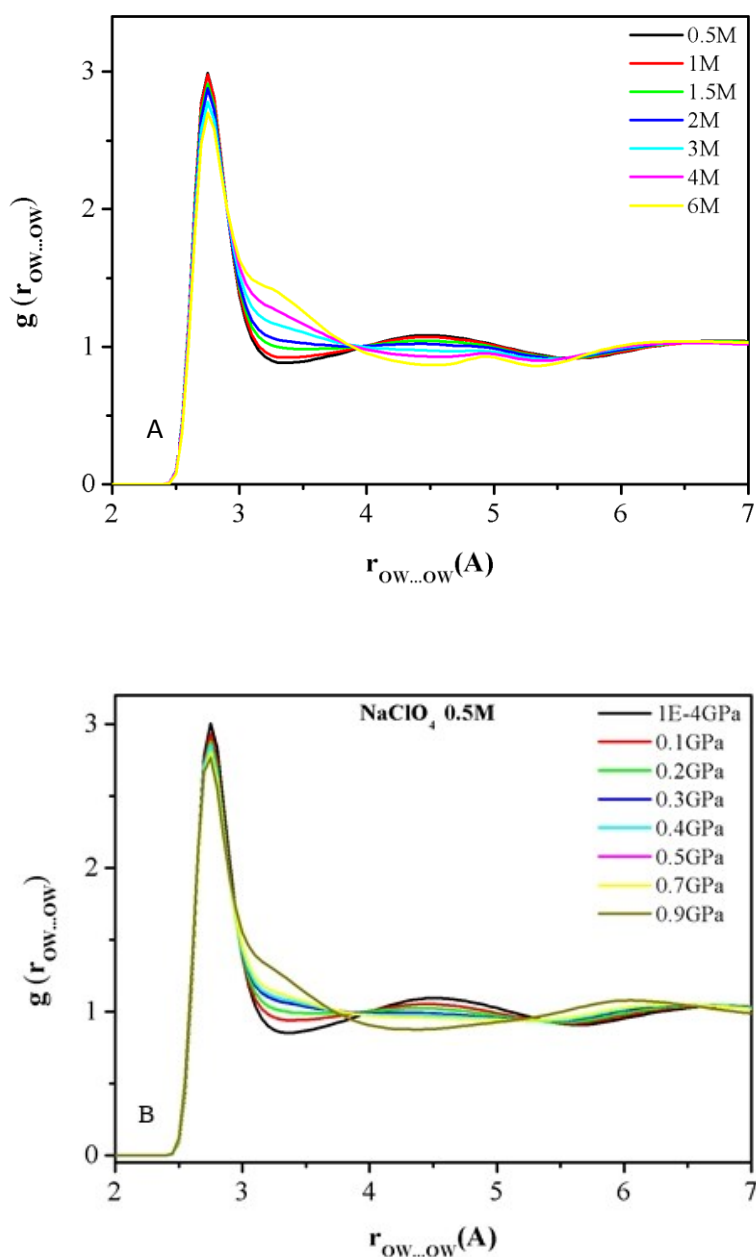
Fig. 6.3 Radial distribution function $g(r)$ for the O···O distance between water molecules. **A)** for different perchlorate concentrations at room pressure; **B)** for 0.5 M solution, at different pressures.

The pressure dependence of the OD vibrational lifetime in **Fig. 4.17** and of the reorientation time reported in **Fig. 4.22** for neat water, for 0.5 M and 2 M solutions, shows striking similarities. For both properties, there is a clear change of slope at a pressure value around 0.2 GPa. Fanetti et al [10] explained this bimodal behavior in pure water with the Laage's extended jump model. From room pressure up to 0.2 GPa, the progressive merging of the first two solvation shells leads to an increasing jump rate of the water molecules. As computer simulations demonstrate [10], this process is completed when the density of

interstitial molecules reaches its maximum value, at the pressure of about 0.2 GPa. Beyond that value, water behaves like a "normal" liquid. In pure water this high-pressure regime results in a constant rotational time (see **Fig. 4.22**).

The behavior of low concentration solutions in the same figure is qualitatively similar: in 0.5 and 2 M solutions, the initial decrease is followed by an almost constant (or very slightly increasing) trend at pressures higher than 0.2 GPa.

A similar change of slope at 0.2 GPa is observed for the vibrational lifetime. In this case the lifetimes of neat water, 0.5 and 2 M solutions are practically indistinguishable, with a moderate initial rise, attributed to the weakening of the HB due to the faster rotational dynamics induced by compression, followed by a decrease due to the shortening (i.e. strengthening) of the HBs due to the increased density.

Perchlorate 6 M solutions behave somehow differently. The pressure dependence of the orientational time (**Fig. 4.24**) has positive slope in the entire pressure range and τ_R increases more than linearly with pressure. The vibrational lifetime in **Fig. 4.19**, has a rather sharp increase below 0.2 GPa, followed by a slow decrease. Note that the lifetime of the stretching mode of the OD weakly bonded to ClO_4^- is more than twice larger than that of bulk water. The difference is due to the much weaker hydrogen bond that reduces the population relaxation rate.

We can then conclude that our results are in line with the predictions of the extended jump model. The concentration threshold value, which separates the dilute perchlorate solutions, where water dynamics is very similar to that of pure water, from the concentrated ones, strongly affected by the water-anion interactions, is located in the range 1.5 – 2 M. This value corresponds closely to the percolation threshold for the hydrogen bonded 3D network.

It is also confirmed that increasing pressure and increasing concentration produce similar effects on the water dynamics. For instance, **Fig 6.4** shows how the concentration dependence of the reorientation time τ_R has a behavior that depends on pressure. Only at room pressure and at 0.1 GPa we observe the initial speed-up of the rotational dynamics, followed by a slowing down for concentrations higher that 2 M. The slope change is not observed for higher pressures, and τ_R increases monotonically.
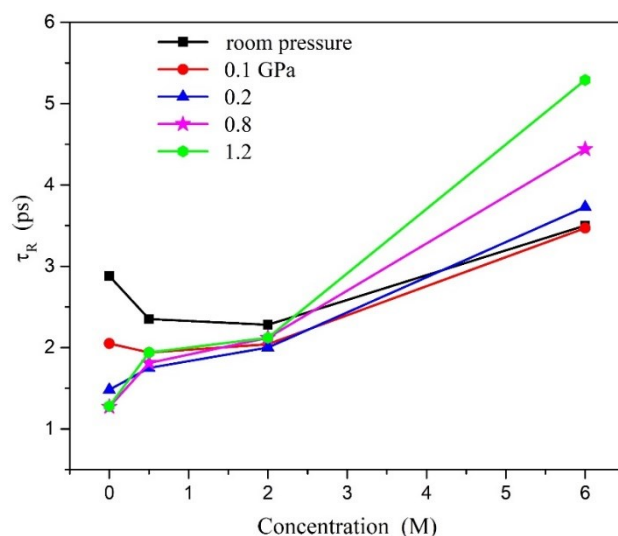
Fig 6.4 Concentration dependence of the water reorientation time τ_R at different pressures.

The same figure indicates that, except neat water and the very dilute 0.5 M solution, the reorientation time is, for all pressures, concentration independent up to the limit of $\sim 1.5 - 2$ moles per litre. On the contrary, beyond that pressure value it is remarkably dependent on pressure: at 2 M concentration τ_R is the same at 1.2 GPa and at 0.1 GPa, in 6 M solution the same time constants differ by a factor of 1.6.

The two-dimensional spectra presented in **Section 4.3** provide additional information on the dynamics of the solutions. The example of **Fig. 4.26** shows the effect of spectral diffusion, which results from the frequency fluctuations due to the local structural rearrangements of the liquid. 2D spectroscopy is informative also for a different kind of dynamics that takes place in solutions: the exchange of the solvent molecules in and out of the first solvation shell of the ClO_4^- ion. As already noticed, this dynamics can be followed experimentally thanks to the frequency difference of the OD stretching vibration when the OD group is bonded to the anion and when is bonded to a water molecule of the bulk liquid.
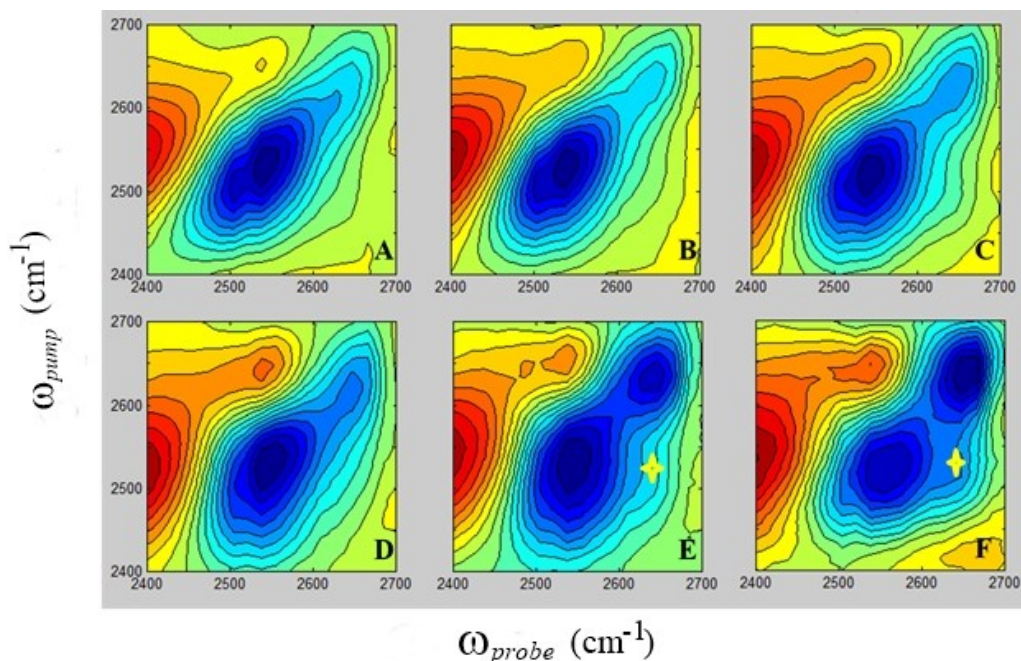
Fig. 6.5 Two-dimensional spectra of 6 M solution recorded at different delay time between pump and probe pulse: **A)** 0.1ps, **B)** 0.2 ps, **C)** 0.3ps, **D)** 0.5ps, **E)** 1ps and **F)** 2.5ps.

In **Fig. 6.5**, I collect six 2D maps obtained at different delay times for a 6 M solution. The maps are qualitatively similar to those of **Fig. 4.26**; due to the large concentration, **Fig. 6.5** shows clear evidence of the peaks corresponding to the two types of OH group, which appear on the diagonal. Moreover, we observe at the delay times of 1 and 2.5 ps, the appearance of a cross peak (c.p.), marked with a small yellow cross in maps E and F of the same figure. The intensity of the cross peak increases with the delay time, because of the chemical exchange of water molecules in and out of the anion solvation shell.

The chemical equilibrium for the exchange of the two OD subpopulations can be written as:

$$OD_P \underset{k_{W \to P}}{\overset{k_{P \to W}}{\rightleftharpoons}} OD_W$$
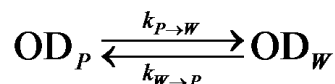
The thermodynamic equilibrium constant is given by the ratio of the kinetic constants of the direct ($k_{p\text{-}w}$) to the inverse ($k_{w\text{-}p}$) reaction.

The rise of the cross peak intensity with the population time provides the tool to measure the kinetic constants. We proceed by taking a slice of the 2D map at the excitation frequency at 2525 cm^{-1}; a Gaussian deconvolution allows extracting the intensity of the cross peak for

86

all the population times. The slices in **Fig. 6.6** show the rise of the cross peak on the high frequency tail of the band.
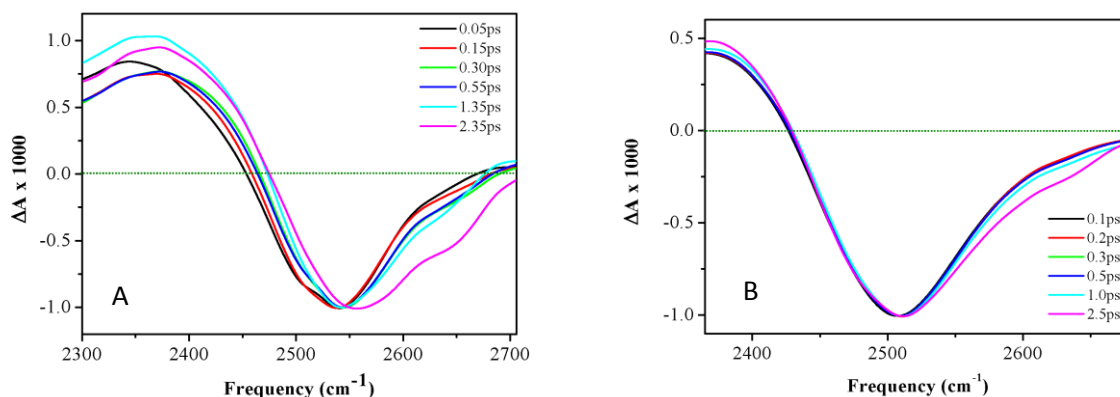

Fig. 6.6 1D slices from the 2D spectrum for different pump-probe delay times: 0.1ps, 0.2 ps, 0.3ps, 0.5ps, 1.0ps and 2. 5ps. **A)** 6 M solution: slice taken at 2525 cm^{-1}; **B)** 2 M solution: slice taken at 2510 cm^{-1}.

The spectra in the figure have been normalized to the minimum of the W_w bleaching band at 2525 cm^{-1} to quantify the growth of the cross peak.

The successive step of the analysis consists in the fit of the 1D spectra as the sum of two Gaussian functions. Then the cross to diagonal ratio of the areas of the two Gaussian bands is calculated and used to build the kinetic trace of the cross peak growth. This last phase is necessary to normalize the intensities measured in different runs and to get rid of the effect of laser fluctuations.

The growth of the cross peak is also visible in the 2D spectra of the 2 M solutions in **Fig. 4.26** and in the corresponding 1D slice of **Fig. 6.6 B**. However, the intensity is too low to provide a reliable kinetic trace.

The growth of the area of the cross peak is shown in **Fig. 6.7** , together with the curve calculated with the solution of the kinetic equation given in ref. [30].
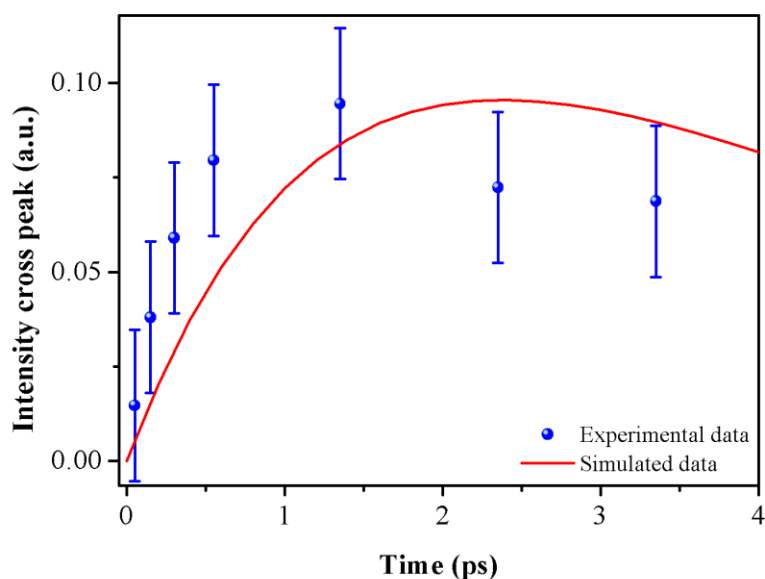
Fig. 6.7 Cross peak area as a function of the delay time between pump and probe pulse. The blue dots are our experimental data; the red line is obtained from the solution of the kinetic equation given in ref [30].

In **Fig.6.7** our experimental data are compared within the curve that describes the growth of the cross peaks according to the equation given in [30], obtained using the parameters provided by Gaffney and co-workers in ref. [42]. Our results are compatible with faster exchange kinetics than the value $k_{ex} = 1/6$ ps^{-1} reported in ref. [42]; however, the signal to noise ratio prevents us from proposing an accurate and reliable alternative value.

We already noticed that time resolved OKE measures the time autocorrelation function of the anisotropic first order susceptibility of the sample (**Eq. 3.10**); it depends on a collective property. This is particularly true in a liquid like water, whose molecular polarizability is almost spherically symmetric. Thus, the OKE response of water is mostly dependent on the intermolecular dynamics (**Eq. 3.13**). The oscillations observed in the OKE signal in the first 2.5 ps are due to the vibrations that are excited by the stimulated Raman effect. As described in equations **3.16 - 3.18**, there are contributions from *intra-molecular* vibrations (**eq. 3.17**) and from *inter-molecular* vibrations, consisting of translational and librational oscillations. The intra-molecular vibrations are described by underdamped ($\gamma < \omega$) harmonic oscillators, and the corresponding oscillating signal corresponds to the time derivative of simple damped cosine functions; the inter-molecular vibrations are overdamped ($\gamma > \omega$) oscillators, described by **eq. 5.3**. While the intra-molecular vibrations are of no interest in the present case, the inter-molecular ones, corresponding to the broad structured band observed below 300 cm^{-1}, are

intrinsically collective in nature and their pressure and concentration dependence can, in principle, provide valuable information on the structure-dynamics correlation. As we discussed in **Section 5.2**, we use two overdamped harmonic oscillator to reproduce that band. In **Fig. 5.14** the growth with increasing pressure of the relative intensity of the ~60 cm^{-1} peak is evident. However, this observation does not contribute very much to a better characterization of the water dynamics in perchlorate solution. In fact, apart from the conventional and partially arbitrary denomination of "HB stretching" (200 cm^{-1} band) and "HB bending" (60 cm^{-1} band), very little is known of the nature of those intermolecular modes. According to the results obtained for neat water in ref. [44], additional insight could be gained by performing high pressure experiments at different temperatures.

In this case, the analysis of the time profile of the OKE signal at longer delay it is much more informative. **Figs. 5.1 – 5.4** show that, for t > 2.5 ps, the time domain signal is dominated by the structural relaxation. We fit the slow relaxation with a stretched exponential function $e^{-(t/\tau)^{\beta}}$, assuming for the stretching parameter β the value 0.7 used for neat water.

Fig. 5.5 shows that the mean structural relaxation time, defined in **Eq. 5.4**, increases monotonically with the concentration. The difference with the behavior of the reorientation tim, obtained from the infrared data, shown in **Fig. 4.15** is striking. The two figures are directly compared here in **Fig. 6.8**.
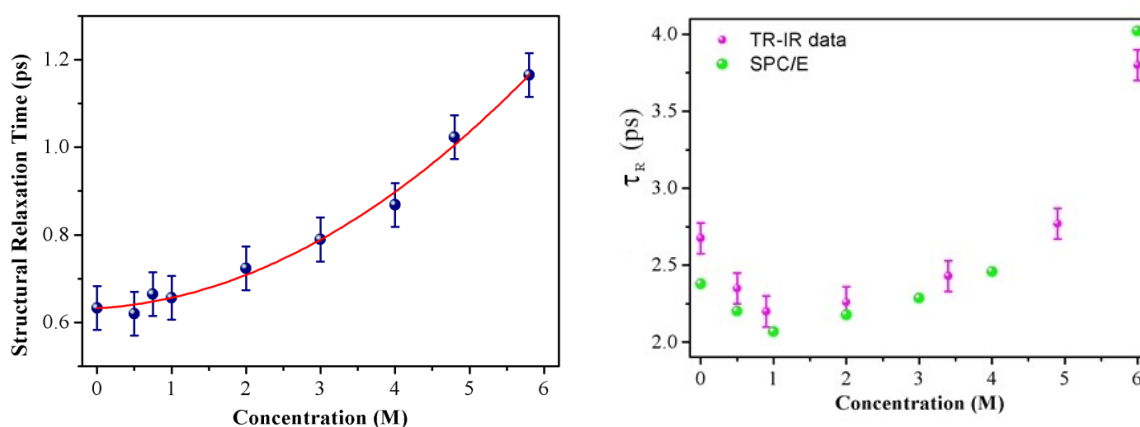

Fig. 6.8 Concentration dependence of the mean structural relaxation time (left) and of the OD reorientation time (right).

It confirms that the dynamics we are looking at in the two experiments is different in nature. The infrared reorientation times depend on the specific mechanism of the molecular orientational motion (well described by the extended jump model) and are sensitive to the short distance interactions involving the first and second solvation shells. In contrast, the structural relaxation OKE data results from complex structural fluctuations that involve intermolecular correlations on very different spatial ranges.
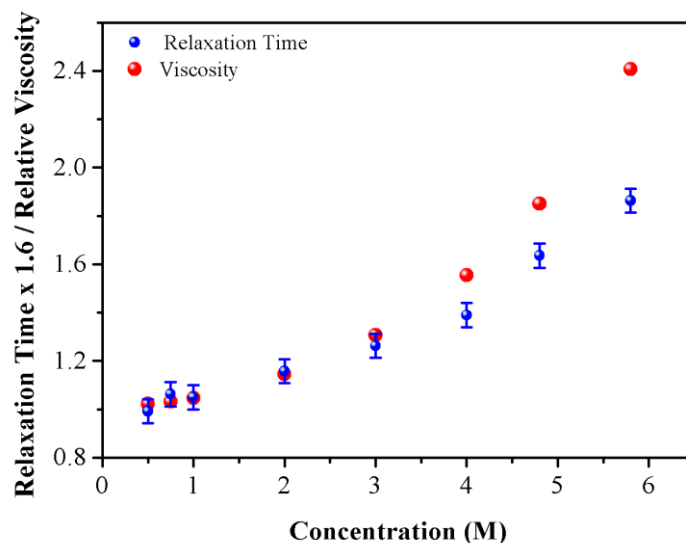

Fig. 6.9 Mean structural relaxation time (blue circles) and the relative viscosity (red circles), expressed as the ratio of solution viscosity and water viscosity, [41] at different $NaClO_4$ concentrations. The relaxations times of **Fig. 5.5** are multiplied by a constant factor to overlap the first value with that of the relative viscosity. Structural relaxation is then more likely to be comparable to the viscosity.

Fig. 6.9 compares the concentration dependence of the mean structural relaxation time with that of the viscosity. Both properties follow a monotonic increase: at low concentration, the trend of the structural relaxation follows perfectly that of the shear viscosity. At concentrations higher than 2 M, viscosity and structural relaxation decouple, the latter growing appreciably less.

If we compare the pressure dependence of the OKE structural relaxation time, shown in **Fig. 5.12**, with that of the infrared reorientation time of **Figs. 4.22** and **4.24**, we observe several analogies. For an easier comparison, here we put the three figures together (**Fig. 6.10**).
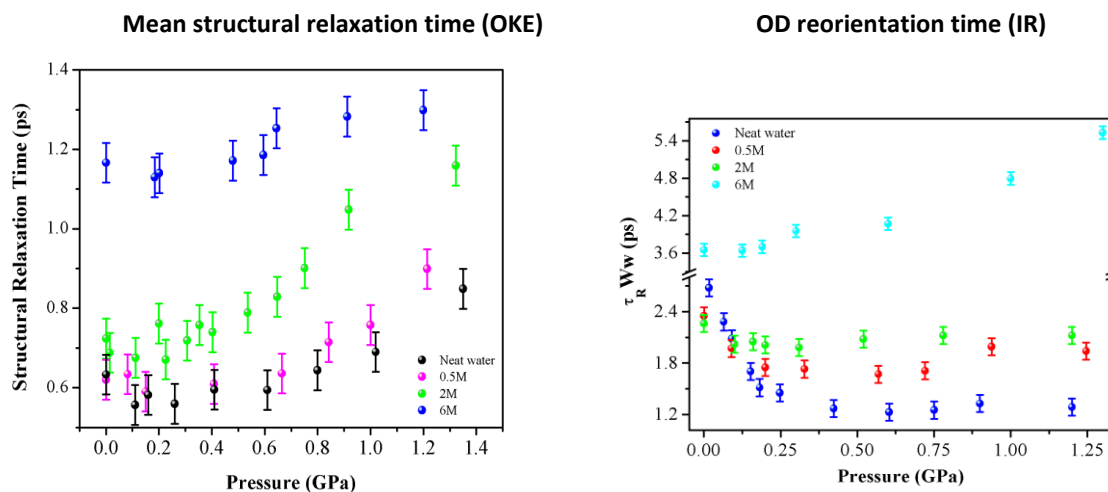

Fig. 6.10 Comparison of the pressure dependence of the mean structural relaxation time (left) and of the OD reorientation time (right).

In both graphs we observe a change of sign of the slope around 0.2 GPa. The change is evident in pure water and in 0.5 M solution; it becomes less and less evident as concentration rises. Actually, in both cases it is hardly visible in the 2 M solution and at higher concentrations.

The figure confirms, once more, two typical features of water and of $NaClO_4$ solutions:

a) 0.2 GPa represents the pressure divide between low density and high density dynamical regimes of pure water, as demonstrated in ref. [10]. This threshold value holds also for dilute solutions and fades off as concentration increases.

b) the concentration value in which the bulk water character of $NaClO_4$ solutions is definitely lost falls in the region 1.5 – 2 M.

Altogether, our data confirm a suggestion already made [43], that pressure and concentration act in the same direction. Both parameters tend to cancel the peculiar behavior of the water dynamical properties: beyond the threshold values of the concentration and of pressure, the liquid behaves like a "normal liquid".

References

[1] Ludwig, R. Water: from clusters to the bulk. *Angewandte Chemie International Edition* **2001**, 40(10), 1808-1827.

[2] Takeya, S., Fujihisa, H., Gotoh, Y., Istomin, V., Chuvilin, E., Sakagami, H., & Hachikubo, A. Methane clathrate hydrates formed within hydrophilic and hydrophobic media: kinetics of dissociation and distortion of host structure. *The Journal of Physical Chemistry C* **2013**, 117(14), 7081-7085.

[3] Walrafen, G. E. Raman spectral studies of the effects of electrolytes on water. *The Journal of Chemical Physics* **1962**, 36(4), 1035-1042.

[4] Terpstra, P., Combes, D., & Zwick, A. Effect of salts on dynamics of water: A Raman spectroscopy study. *The Journal of chemical physics* **1990**, 92(1), 65-70.

[5] Cox, W. M. & Wolfenden, J. H. *Proc. R. Soc. London*, Ser. A **1934**, 145, 486.

[6] Laage, D., & Hynes, J. T. A molecular jump mechanism of water reorientation. *Science* **2006**, 311(5762), 832-835.

[7] Laage, D., Stirnemann, G., Sterpone, F., Rey, R., & Hynes, J. T. Reorientation and allied dynamics in water and aqueous solutions. *Annual review of physical chemistry* **2011**, 62, 395-416.

[8] Park, S., & Fayer, M. D. Hydrogen bond dynamics in aqueous NaBr solutions. *Proceedings of the National Academy of Sciences* **2007**, 104(43), 16731-16738.

[9] Fayer, M. D. (Ed.). *Ultrafast infrared vibrational spectroscopy* **2013**. CRC Press.

[10] Fanetti, S., Lapini, A., Pagliai, M., Citroni, M., Di Donato, M., Scandolo, S., ... & Bini, R. Structure and dynamics of low-density and high-density liquid water at high pressure. *The journal of physical chemistry letters* **2013**, 5(1), 235-240.

[11] Fanetti, S., Pagliai, M., Citroni, M., Lapini, A., Scandolo, S., Righini, R., & Bini, R. Connecting the water phase diagram to the metastable domain: High-pressure studies in the supercooled regime. *The journal of physical chemistry letters* **2014**, *5*(21), 3804-3809.

[12] Bartolini, P., Taschin, A., Eramo, R., & Torre, R. Optical Kerr Effect Experiments on Complex Liquids. In *Time-Resolved Spectroscopy in Complex Liquids* **2008**. Springer US.

[13] Mukamel, S. *Principles of nonlinear optical spectroscopy* **1999**. Oxford University Press.

[14] Costard, R. *Ultrafast Dynamics of Phospholipid-Water Interfaces: Studied by Nonlinear Time-Resolved Vibrational Spectroscopy* **2015**. Springer.

[15] Ernst, R. R., Bodenhausen, G., & Wokaun, A. *Principles of nuclear magnetic resonance in one and two dimensions* **1987**. Clarendon Press.

[16] Laane, J. (Ed.). *Frontiers of molecular spectroscopy* **2011**. Elsevier.

[17] Hamm, P., & Zanni, M. *Concepts and methods of 2D infrared spectroscopy* **2011**. Cambridge University Press.

[18] Hamm, P., Lim, M., & Hochstrasser, R. M. Structure of the amide I band of peptides measured by femtosecond nonlinear-infrared spectroscopy. *The Journal of Physical Chemistry B* **1998**, 102(31), 6123-6138.

[19] Hausherr, M. *Development of an Interferometer-based Transient Two-dimensional Infrared Spectrometer* **2011**. PhD Thesis.

[20] Touceda, P. T. *Transient infrared spectroscopy: a new approach to investigate valence tautomerism* **2009**. PhD Thesis.

[21] Kaindl, R. A., Wurm, M., Reimann, K., Hamm, P., Weiner, A. M., & Woerner, M. Generation, shaping, and characterization of intense femtosecond pulses tunable from 3 to 20 μm. *JOSA B* **2000**, 17(12), 2086-2094.

[22] Vauthey, E., *Introduction to nonlinear optical spectroscopic techniques for investigating ultrafast processes* **2006**. Univ. of Geneva.

[23] Zhong, Q., Fourkas, J., *Optical Kerr Effect Spectroscopy of Simple Liquids* **2009**. PhD Thesis.

[24] Bartolini, P., Taschin, A., Eramo, R., Righini, R., & Torre, R. Optical Kerr effect measurements on supercooled water: the experimental perspective. In *Journal of Physics: Conference Series* **2009**, 177, 1, 012009.

[25] Taschin, A., Bartolini, P., Eramo, R., Righini, R., & Torre, R. Optical Kerr effect of liquid and supercooled water: The experimental and data analysis perspective. *The Journal of chemical physics* **2014**, 141(8), 084507.

[26] Stirnemann, G., Wernersson, E., Jungwirth, P., & Laage, D. Mechanisms of acceleration and retardation of water dynamics by ions. *Journal of the American Chemical Society* **2013**, 135(32), 11824-11831.

[27] Steinel, T., Asbury, J. B., Zheng, J., & Fayer, M. D. Watching hydrogen bonds break: A transient absorption study of water. *The Journal of Physical Chemistry A* **2004**, 108(50), 10957-10964.

[28] Rezus, Y. L. A., & Bakker, H. J. On the orientational relaxation of HDO in liquid water. *The Journal of chemical physics* **2005**, 123(11), 114502.

[29] Heinje, G., Luck, W. A. P., & Heinzinger K. Molecular Dynamics Simulation of an

Aqueous NaClO$_4$ Solution. *J. Phys. Chem.* **1987**, 91, 331-338.

[30] Kwak, K., Zheng, J., Cang, H., & Fayer, M. D. Ultrafast two-dimensional infrared vibrational echo chemical exchange experiments and theory. *The Journal of Physical Chemistry B* **2006**, 110(40), 19998-20013.

[31] Procacci, P., Hybrid MPI/OpenMP Implementation of the ORAC Molecular Dynamics Program for Generalized Ensemble and Fast Switching Alchemical Simulations. *J. Chem. Inf. Model.* **2016**, 56, 1117-1121.

[32] Procacci, P., Paci, E., Darden, T., & Marchi, M. ORAC: A Molecular Dynamics Program to Simulate Complex Molecular Systems with Realistic Electrostatic Interactions. *J. Comput. Chem.* **1997**, 18, 1848-1862.

[33] Marsili, S., F. Signorini, G., Chelli, R., Marchi, M., & Procacci P. Orac: A molecular dynamics simulation program to explore free energy surfaces in biomolecular systems at the atomistic level. *J. Comput. Chem.* **2010**, 31, 1106-1116.

[34] Berendsen, H. J. C., Grigera, J. R., & Straatsma, T. P. The missing term in effective pair potentials. *J. Phys. Chem.* **1987**, 91, 6269-6271.

[35] Engel, G.; Hertz, H. G. Ber. Bunsenges. Phys. Chem. **1968**, 72, 808.

[36] Mähler, J., & Persson, I. A study of the hydration of the alkali metal ions in aqueous solution. *Inorganic Chemistry* **2011**, 51(1), 425-438.

[37] Wachter, W., Kunz, W., Buchner, R., & Hefter, G. Is there an anionic Hofmeister effect on water dynamics? Dielectric spectroscopy of aqueous solutions of NaBr, NaI, NaNO$_3$, NaClO$_4$, and NaSCN. *The Journal of Physical Chemistry A* **2005**, 109(39), 8675-8683.

[38] Gaffney, K. J., Ji, M., Odelius, M., Park, S., & Sun, Z. H-bond switching and ligand exchange dynamics in aqueous ionic solution. *Chemical Physics Letters* **2011**, 504(1), 1-6.

[39] Stanley, H. E., & Teixeira, J. Interpretation of the unusual behavior of H$_2$O and D$_2$O at low temperatures: tests of a percolation model. *The Journal of Chemical Physics* **1980**, 73(7), 3404-3422.

[40] Bondarenko, G. V., & Gorbaty, Y. E. Hydrogen bonding in aqueous solution of NaClO$_4$. *Molecular Physics* **2011**, 109(5), 783-788.

[41] Janz, G. J., Oliver, B. G., Lakshminarayanan, G. R., & Mayer, G. E. Electrical conductance, diffusion, viscosity, and density of sodium nitrate, sodium perchlorate, and sodium thiocyanate in concentrated aqueous solutions. *The Journal of Physical Chemistry* **1970**, 74(6), 1285-1289.

[42] Park, S., Odelius, M., & Gaffney, K. J. Ultrafast dynamics of hydrogen bond exchange in aqueous ionic solutions. *The Journal of Physical Chemistry B* **2009**, 113(22), 7825-7835.

[43] Holzmann, J., Ludwig, R., Geiger, A., & Paschek, D. Pressure and salt effects in simulated water: two sides of the same coin?. *Angewandte Chemie International Edition* **2007**, 46(46), 8907-8911.

[44] Taschin, A., Bartolini, P., Eramo, R., Righini, R., & Torre, R. Evidence of two distinct local structures of water from ambient to supercooled conditions. *Nature communications* **2013**, 4, 2401.